HOKKAIDO UNIVERSITY

Title	Study on high-temperature latent heat storage using Al-Si alloy
Author(s)	坂井, 浩紀
Degree Grantor	北海道大学
Degree Name	博士(工学)
Dissertation Number	甲第14867号
Issue Date	2022-03-24
DOI	https://doi.org/10.14943/doctoral.k14867
Doc URL	https://hdl.handle.net/2115/94575
Type	doctoral thesis
File Information	Hiroki_Sakai.pdf

Hokkaido University Collection of Scholarly and Academic Papers : HUSCAP

Study on high-temperature latent heat storage using Al-Si alloy

Al-Si 合金を用いた高温潜熱蓄熱に関する研究

Hiroki Sakai

Hokkaido University

CONTENTS

Chapter 1

General Introduction

1.1 Demand for latent heat-storage materials

The development of thermal energy storage (TES) technologies is considered important either as a main option or a component of energy-storage systems for energy grids. The most attractive advantage of concentrated solar power plants (CSPs) with TES is their dispatchability. The number of commercial CSP plants that can continuously operate 24 h a day due to the application of TES is increasing [1-3]. Furthermore, newly-developed storage systems have been proposed recently that convert electricity into heat, (using thermophotovoltaic cells [4, 5], electric heaters [6], or heat pumps), and then store the heat using TES, before finally converting it back into electricity. These systems are expected to overcome the limitations of the intermittent generation of renewable energies, which is a key issue for installing renewable energy in the power network in a cost-effective way. Because TES is a key process within these concepts, various TES systems have recently been reported, such as those using the sensible heat of pebbles [6] or molten salt [7], and the sensible and latent heat of liquid Si [8]. Considering TES as a stable energy buffer for renewable-energy power plants, high-temperature TES has great advantages. Considering thermodynamic limitations, high-temperature heat sources (or those with a large temperature gap between the heat source and heat sink) increase the efficiency of power generation. Considering the exergy of the system, high-temperature heat sources reduce exergy loss to a greater degree than low-temperature ones, as the exergy efficiencies of electricity and solar

energy are both close to 1. Therefore, the development of high-temperature TES is urgently needed to enable the installation of renewable energy to a considerable extent.

In addition, TES technologies have attracted attention in industrial fields. For example, large amounts of energy are required for steelmaking and chemical manufacturing, and some of this energy is lost as thermal energy. From the perspective of energy conservation, effective use of this unused heat is important. It is difficult to use exhaust heat directly due to spatial and time gaps between the heat source and demand of thermal energy. Therefore, TES can be used as a stable energy buffer to overcome this limitation, and can be used for many processes [9-11].

Although sensible heat storage using molten salt [7, 12, 13], concrete [14], brick [15], and pebbles [6] are all typical methods for high-temperature TES, an alternative storage method that has received significant attention is latent heat storage (LHS) using a phase change material (PCM). As discussed in previous review papers [16-18], LHS has three main advantages. First, it achieves a high heat capacity. LHS can store a large amount of heat with a small temperature swing, because the cumulative stored heat changes in a single step around the melting temperature of the PCM. The second advantage is the constant charging/discharging temperature. In the LHS technique, the temperature does not change when heat is stored via the phase transition. The PCM can be regarded as an isothermal heat source; therefore, rapid heat exchange is possible. The third advantage is that LHS does not involve chemical changes. This advantage can simplify the system and further lower the costs. These advantages make LHS desirable for use in high-temperature TES applications.

A PCM with a high melting temperature should be selected for high-temperature LHS, because the PCM can store heat at its melting temperature. Molten salts are typical high-temperature PCMs [19]. Delise et al. investigated the

thermophysical properties of nitrate mixtures containing Na/K/Li/Ca [20]. Mathur et al. encapsulated sodium nitrate with ZnO, and formed internal voids inside the nitrate capsules using a sacrificial polymer, which was later used for evaluation of its cyclic durability [21]. Yu et al. proposed a composite containing $NaNO_3$ as a PCM, and $Ca(OH)_2$ as a matrix, fabricated by cold sintering [22]. Miliozzi et al. mixed concrete with $NaNO_3$–KNO_3 eutectic-type PCM inserted in diatomite [23]. Chloride salts were selected as PCMs that operate at higher temperature than nitrate salts. Myers et al. reviewed pure and eutectic chloride salts [24]. Singh et al. infiltrated $MgCl_2$ into graphite foams and measured the fusion heats and thermal diffusivities of the products [25]. Tian et al. fabricated a composite consisting of binary eutectic NaCl–$CaCl_2$ and expanded graphite [26]. Leng et al. synthesized form-stable PCM using KCl–NaCl eutectic salts and diatomite [27]. Carbonate salts have also been studied as high-temperature PCMs [28, 29].

1.2 Metallic PCMs

Metals and alloys are alternative classes of PCM materials. Metallic PCMs such as Al, Cu, and their alloys, have high melting temperatures, high thermal conductivities, and high heat-storage densities. Some studies have evaluated the potential of metals and alloys as PCM materials. Risueño et al. selected five types of Zn–Mg–Al alloys, considering their melting temperature, fusion enthalpy, and cost [30]. Short- (100 cycles) and long-term (500 cycles) thermal cyclic durability tests were performed with these alloys using differential scanning calorimetry (DSC) and an electric furnace, respectively. After 500 thermal cyclic tests, Mg–51mass%Zn and Mg–47mass%Zn–4mass%Al had excellent thermal stability. The thermophysical properties of Mg–51mass%Zn were characterized previously [31]. The cyclic stability of the Mg–

Zn alloy was analyzed using simultaneous thermal analysis with thermogravimetry, differential thermal analysis, and mass spectrometry. After 20 cyclic tests, no appreciable mass change was observed. The authors also examined the thermal diffusivity and thermal conductivity of the alloy over a range of temperatures from room temperature to ~400 °C (above the melting temperature of the alloy). The Mg–Zn alloy had thermal diffusivity and conductivity two orders of magnitude higher than those of other salt PCMs with similar melting temperatures. Gokon et al. tested the thermal stability of four kinds of hypereutectic Al–Si alloys in graphite containers [32]. Cyclic tests (20 cycles) were performed for these alloys under vacuum conditions. After these cyclic tests, Al–25mass%Si showed little oxidation, and there was no reaction between the alloy and graphite. Rea et al. designed a thermal storage tank with an Al–12mass%Si alloy, connected to a valved thermosyphon to control heat flow, and thermoelectric generators to convert heat to electricity [33]. The thermal storage tank received and distributed heat, and the temperature gradient in the tank was below 6 °C. Andraka et al. synthesized a eutectic Cu–Mg–Si alloy, the composition of which was based on FactSage calculations, an American Society for Metals (ASM) diagram, and the report by Birchenall et al. [34] as a PCM for a Dish–Stirling system [35]. Three Cu–Mg–Si alloys were evaluated using DSC, and they determined the eutectic composition and heat of fusion of this system. They concluded that the ASM composition, Cu–21.16mass%Mg–25.34mass% Si, was eutectic and has the highest fusion heat.

Metallic PCMs are attractive for use as a TES material. However, the high corrosivity of molten metal is a problem when using a metallic PCM. The structure that encapsulates the PCM metal must completely cover the metal to prevent leaks when the metal is molten, i.e., it should have a core–shell structure. To overcome these limitations, metallic PCM composites have been studied. Xu et al. reported a form-stable Al–Al_2O_3

composite, in which Al is the PCM and Al_2O_3 is the skeleton [36]. They developed an Al–Al_2O_3 mixed-sintering method, and studied the optimum molding pressure and time. Lao et al. prepared an alloy/honeycomb ceramic composite with Al–Si alloy and SiC-whisker–Al_2O_3 [37], by adding alloy powder to some of the honeycomb holes. Macro-encapsulation is another way to form PCM composites. Several methods for the macro-encapsulation of metallic PCMs have been studied. Several shell materials have been used, including metals [38-40], ceramics [41], and glass [42].

1.3 Microencapsulated PCM

In the aforementioned methods for fabricating metallic PCM composites, it is difficult to fill the PCM into the matrix or skeleton densely, without any leakage of the molten metal. The shape of the PCM composites is also limited. Alloy-type microencapsulated PCMs (MEPCMs) have been developed as candidate materials to address these problems. MEPCMs consist of a metallic core and a ceramic shell. Microencapsulation allows for easier handling, and enables the use of this PCM as a powder. MEPCMs are ideal candidates for enabling further application of the LHS technique.

Since Nomura et al. reported a simple method for manufacturing MEPCMs using Al–Si alloys [43, 44], Al–Si/Al_2O_3 core/shell MEPCM with high cyclic durability [45, 46] and an Al–Zn type MEPCM [47] were reported. Recently, various compositions of the core material of the MEPCM have been reported. In the Sn system, shells of SiO_2 [48], $CaCO_3$ [49], and TiO_2 [50] were reported. Fe–SiC core–shell microcapsules fabricated by chemical vapor deposition [51] were also reported. An MEPCM with a Zn–Al core and Ni and NiP multilayer shell [52] was also reported. In terms of shell development, an Al_2O_3 and AlN shell [53], Al_2O_3 and mullite layers [54], and Al_2O_3

shell covered with Cu [55, 56] were reported.

As a further application of the use of MEPCMs, the bottom-up design of a TES structure is suggested. As mentioned earlier, MEPCM can be used as a powder material. By combining MEPCM with sintering aids or ceramics, powder compaction technology can be applied to create heat-storage structures with various shapes. According to this concept, it is easy to fabricate an LHS structure with shapes suitable for heat-exchanger applications.

Combining an MEPCM with a catalyst is also proposed as another application of MEPCM. The combination of PCM and a chemical reaction itself was proposed [39, 57, 58] to stabilize the heat source when using waste heat for endothermic reactions. Because MEPCM is a powder material, the catalyst can be placed near the heat-storage material. Therefore, it is possible to integrate the catalyst and heat-storage layers, enabling heat to be exchanged quickly between these two materials and preventing overheating of the catalyst. It is also considered feasible to develop a new reaction system that integrates exothermic and endothermic reactions, and a heat-storage layer.

The undercooling of MEPCM, i.e., the mismatch between the melting and solidification temperatures, needs to be solved for the development of these applications. Undercooling has been reported in alloy-based MEPCM. Undercooling reduces the heat-release initiation temperature, which limits the heat exchange process. This can be a fatal drawback in applications where constant temperature control is required, such as those in combination with catalytic reactions.

In this thesis, various studies were conducted to develop applications of MEPCMs as excellent thermal-storage materials. In Chapter 2, the concept of a bottom-up design of an LHS material using the MEPCM concept is discussed. In Chapter 3, the usefulness of the combination of a heat-storage material and catalyst is

evaluated by investigating the effect of the heat-storage material on an endothermic reaction. Chapter 4 discusses the unique supercooling of alloy-type MEPCMs, with a focus on the composition and particle size of Al–Si-type MEPCMs. In Chapter 5, the addition of nucleation agents to the MEPCM as an attempt to suppress undercooling is discussed. Finally, Chapter 6 provides an overall conclusion of this study.

References

[1] Zanganeh G, Pedretti A, Zavattoni S, Barbato M, Steinfeld A. Packed-bed thermal storage for concentrated solar power–Pilot-scale demonstration and industrial-scale design. Sol Energy. 2012;86:3084-98.

[2] Tian Y, Zhao C-Y. A review of solar collectors and thermal energy storage in solar thermal applications. Appl Energy. 2013;104:538-53.

[3] Slocum AH, Codd DS, Buongiorno J, Forsberg C, McKrell T, Nave J-C, et al. Concentrated solar power on demand. Sol Energy. 2011;85:1519-29.

[4] Datas A, Ramos A, Martí A, del Cañizo C, Luque A. Ultra high temperature latent heat energy storage and thermophotovoltaic energy conversion. Energy. 2016;107:542-9.

[5] Datas A, Zeneli M, del Cañizo C, Malgarinos I, Nikolopoulos A, Nikolopoulos N, et al. Molten silicon storage of concentrated solar power with integrated thermophotovoltaic energy conversion. AIP Conference Proceedings: AIP Publishing; 2018. p. 090005.

[6] Stevanovic D, Rembold T. High temperature energy storage based on hot air turbine and pebble-heater technology. 2016 4th International Symposium on Environmental Friendly Energies and Applications (EFEA): IEEE; 2016. p. 1-6.

[7] Laughlin RB. Pumped thermal grid storage with heat exchange. Journal of Renewable and Sustainable Energy. 2017;9:044103.

[8] Meroueh L, Chen G. Thermal energy storage radiatively coupled to a supercritical Rankine cycle for electric grid support. Renew Energ. 2020;145:604-21.

[9] Nomura T, Oya T, Okinaka N, Akiyama T. Feasibility of an advanced waste heat transportation system using high-temperature phase change material (PCM). ISIJ Int. 2010;50:1326-32.

[10] Dal Magro F, Meneghetti A, Nardin G, Savino S. Enhancing energy recovery in the steel industry: Matching continuous charge with off-gas variability smoothing. Energy Convers Manage. 2015;104:78-89.

[11] Miró L, Gasia J, Cabeza LF. Thermal energy storage (TES) for industrial waste heat (IWH) recovery: A review. Appl Energy. 2016;179:284-301.

[12] Kuravi S, Trahan J, Goswami DY, Rahman MM, Stefanakos EK. Thermal energy storage technologies and systems for concentrating solar power plants. Prog Energy Combust Sci. 2013;39:285-319.

[13] Fereres S, Prieto C, Giménez-Gavarrell P, Rodríguez A, Sánchez-Jiménez PE, Pérez-Maqueda LA. Molten carbonate salts for advanced solar thermal energy power plants: Cover gas effect on fluid thermal stability. Sol Energy Mater Sol Cells. 2018;188:119-26.

[14] Alonso MC, Vera-Agullo J, Guerreiro L, Flor-Laguna V, Sanchez M, Collares-Pereira M. Calcium aluminate based cement for concrete to be used as thermal energy storage in solar thermal electricity plants. Cem Concr Res. 2016;82:74-86.

[15] Forsberg CW, Stack DC, Curtis D, Haratyk G, Sepulveda NA. Converting excess low-price

electricity into high-temperature stored heat for industry and high-value electricity production. The Electricity Journal. 2017;30:42-52.
[16] Farid MM, Khudhair AM, Razack SAK, Al-Hallaj S. A review on phase change energy storage: materials and applications. Energy Convers Manage. 2004;45:1597-615.
[17] Zalba B, Marın JM, Cabeza LF, Mehling H. Review on thermal energy storage with phase change: materials, heat transfer analysis and applications. Appl Therm Eng. 2003;23:251-83.
[18] Sharma A, Tyagi VV, Chen CR, Buddhi D. Review on thermal energy storage with phase change materials and applications. Renew Sust Energ Rev. 2009;13:318-45.
[19] Kenisarin MM. High-temperature phase change materials for thermal energy storage. Renew Sust Energ Rev. 2010;14:955-70.
[20] Delise T, Tizzoni A, Ferrara M, Corsaro N, D'Ottavi C, Sau S, et al. Thermophysical, environmental, and compatibility properties of nitrate and nitrite containing molten salts for medium temperature CSP applications: A critical review. J Eur Ceram Soc. 2019;39:92-9.
[21] Mathur A, Kasetty R, Oxley J, Mendez J, Nithyanandam K. Using encapsulated phase change salts for concentrated solar power plant. Energy Procedia. 2014;49:908-15.
[22] Yu Q, Jiang Z, Cong L, Lu T, Suleiman B, Leng G, et al. A novel low-temperature fabrication approach of composite phase change materials for high temperature thermal energy storage. Appl Energy. 2019;237:367-77.
[23] Miliozzi A, Chieruzzi M, Torre L. Experimental investigation of a cementitious heat storage medium incorporating a solar salt/diatomite composite phase change material. Appl Energy. 2019;250:1023-35.
[24] Myers Jr PD, Goswami DY. Thermal energy storage using chloride salts and their eutectics. Appl Therm Eng. 2016;109:889-900.
[25] Singh D, Kim T, Zhao W, Yu W, France DM. Development of graphite foam infiltrated with $MgCl_2$ for a latent heat based thermal energy storage (LHTES) system. Renew Energ. 2016;94:660-7.
[26] Tian H, Wang W, Ding J, Wei X, Huang C. Preparation of binary eutectic chloride/expanded graphite as high-temperature thermal energy storage materials. Sol Energy Mater Sol Cells. 2016;149:187-94.
[27] Leng G, Qiao G, Jiang Z, Xu G, Qin Y, Chang C, et al. Micro encapsulated & form-stable phase change materials for high temperature thermal energy storage. Appl Energy. 2018;217:212-20.
[28] Li C, Li Q, Cong L, jiang F, Zhao Y, Liu C, et al. MgO based composite phase change materials for thermal energy storage: The effects of MgO particle density and size on microstructural characteristics as well as thermophysical and mechanical properties. Appl Energy. 2019;250:81-91.
[29] Li C, Li Q, Li Y, She X, Cao H, Zhang P, et al. Heat transfer of composite phase change material modules containing a eutectic carbonate salt for medium and high temperature thermal energy storage applications. Appl Energy. 2019;238:1074-83.
[30] Risueño E, Gil A, Rodríguez-Aseguinolaza J, Tello M, Faik A, D'Aguanno B. Thermal cycling testing of Zn–Mg–Al eutectic metal alloys as potential high-temperature phase change materials for latent heat storage. J Therm Anal Calorim. 2017;129:885-94.

[31] Blanco-Rodríguez P, Rodríguez-Aseguinolaza J, Risueño E, Faik A, Tello M, Doppiu S. Thermophysical characterization of Mg-51% Zn eutectic metal alloy: A phase change material for thermal energy storage in direct steam generation applications (vol 75, pg 630, 2014). Energy. 2014;75:630-.
[32] Gokon N, Nakamura S, Yamaguchi T, Kodama T. Cyclic properties of thermal storage/discharge for Al-Si alloy in vacuum for solar thermochemical fuel production. Energy Procedia. 2015;69:1759-69.
[33] Rea JE, Oshman CJ, Singh A, Alleman J, Parilla PA, Hardin CL, et al. Experimental demonstration of a dispatchable latent heat storage system with aluminum-silicon as a phase change material. Appl Energy. 2018;230:1218-29.
[34] Birchenall CE, Gueceri S, Farkas D, Labdon MB, Nagaswami N, Pregger B. Heat storage in alloy transformations. Final report. National Aeronautics and Space Administration, Cleveland, OH (USA). Lewis Research Center; Delaware Univ., Newark(US). Dept. of Chemical Engineering; 1981.
[35] Andraka CE, Kruizenga AM, Hernandez-Sanchez BA, Coker EN. Metallic phase change material thermal storage for dish Stirling. Energy Procedia. 2015;69:726-36.
[36] Xu Y, He Y-L, Zhu G-H, Lv S, Shan B. Al/Al_2O_3 form-stable phase change material for high temperature thermal energy storage. Energy Procedia. 2017;105:4328-33.
[37] Lao X, Xu X, Wu J, Xu X. High-temperature alloy/honeycomb ceramic composite materials for solar thermal storage applications: Preparation and stability evaluation. Ceram Int. 2017;43:4583-93.
[38] Zhang G, Li J, Chen Y, Xiang H, Ma B, Xu Z, et al. Encapsulation of copper-based phase change materials for high temperature thermal energy storage. Sol Energy Mater Sol Cells. 2014;128:131-7.
[39] Maruoka N, Sato K, Yagi J, Akiyama T. Development of PCM for Recovering High Temperature Waste Heat and Utilization for Producing Hydrogen by Reforming Reaction of Methane. ISIJ Int. 2002;42:215-9.
[40] Ma B, Li J, Xu Z, Peng Z. Fe-shell/Cu-core encapsulated metallic phase change materials prepared by aerodynamic levitation method. Appl Energy. 2014;132:568-74.
[41] Fukahori R, Nomura T, Zhu C, Sheng N, Okinaka N, Akiyama T. Macro-encapsulation of metallic phase change material using cylindrical-type ceramic containers for high-temperature thermal energy storage. Appl Energy. 2016;170:324-8.
[42] Gimenez-Gavarrell P, Fereres S. Glass encapsulated phase change materials for high temperature thermal energy storage. Renew Energ. 2017;107:497-507.
[43] Nomura T, Zhu C, Sheng N, Saito G, Akiyama T. Microencapsulation of metal-based phase change material for high-temperature thermal energy storage. Sci Rep. 2015;5:9117.
[44] Nomura T, Sheng N, Zhu C, Saito G, Hanzaki D, Hiraki T, et al. Microencapsulated phase change materials with high heat capacity and high cyclic durability for high-temperature thermal energy storage and transportation. Appl Energy. 2017;188:9-18.
[45] Sheng N, Zhu C, Saito G, Hiraki T, Haka M, Hasegawa Y, et al. Development of a microencapsulated Al–Si phase change material with high-temperature thermal stability and durability over 3000 cycles. J of Mater Chem A. 2018;6:18143-53.

[46] Sheng N, Zhu C, Sakai H, Hasegawa Y, Akiyama T, Nomura T. Modified preparation of Al_2O_3@ Al-Si microencapsulated phase change material for high-temperature thermal storage with high durability over 3000 cycles. Sol Energy Mater Sol Cells. 2019;200:109925.
[47] Kawaguchi T, Sakai H, Sheng N, Kurniawan A, Nomura T. Microencapsulation of Zn-Al alloy as a new phase change material for middle-high-temperature thermal energy storage applications. Appl Energy. 2020;276:115487.
[48] Bao J, Zou D, Zhu S, Ma Q, Wang Y, Hu Y. A medium-temperature, metal-based, microencapsulated phase change material with a void for thermal expansion. Chem Eng J. 2021;415:128965.
[49] Ma Q, Zou D, Wang Y, Lei K. Preparation and properties of novel ceramic composites based on microencapsulated phase change materials (MEPCMs) with high thermal stability. Ceram Int. 2021.
[50] Zhu S, Zou D, Bao J, Ma Q, Wang Y, Hu Y. Synthesis and characterization of a novel high durability alloy microcapsule for thermal energy storage. Sol Energy Mater Sol Cells. 2021;230:111262.
[51] Zhang F, Zhong Y, Yang X, Lin J, Zhu Z. Encapsulation of metal-based phase change materials using ceramic shells prepared by spouted bed CVD method. Sol Energy Mater Sol Cells. 2017;170:137-42.
[52] Svetlizky D, Kazimierczak H, Ovadia B, Sharoni A, Eliaz N. Electrochemical Processing and Thermal Properties of Functional Core/Multi-Shell ZnAl/Ni/NiP Microparticles. Materials. 2021;14:834.
[53] Wei H, Yang S, Wang C, Qiu C, Lin K, Han J, et al. Novel and durable composite phase change thermal energy storage materials with controllable melting temperature. J Mater Sci Technol. 2021;86:11-9.
[54] Han C, Gu H, Zhang M, Huang A, Zhang Y, Wang Y. Al–Si@ Al_2O_3@ mullite microcapsules for thermal energy storage: Preparation and thermal properties. Sol Energy Mater Sol Cells. 2020;217:110697.
[55] Sheng N, Zhu C, Sakai H, Akiyama T, Nomura T. Synthesis of Al-25 wt% Si@ Al_2O_3@ Cu microcapsules as phase change materials for high temperature thermal energy storage. Sol Energy Mater Sol Cells. 2019;191:141-7.
[56] Li Q, Ma X, Zhang X, Zhang J, Ma J, Hu X, et al. Preparation of a new capsule phase change material for high temperature thermal energy storage. J Alloys Compd. 2021;868:159179.
[57] Maruoka N, Akiyama T. Exergy recovery from steelmaking off-gas by latent heat storage for methanol production. Energy. 2006;31:1632-42.
[58] Maruoka N, Akiyama T. Development of PCM reactor for methane steam reforming. ISIJ Int. 2010;50:1305-10.

Chapter 2

Fabrication of heat storage pellets composed of microencapsulated phase change material for high-temperature applications

2.1 Introduction

Microencapsulated phase change material (MEPCM) is an ideal candidate for realizing the bottom-up design of a thermal energy storage (TES) structure with high heat capacity and a high degree of freedom in shape. The achievement of the bottom-up design concept via the metallic MEPCM is the novelty of chapter 2. Based on the bottom-up design of the TES structure using the MEPCM, various methods can be adopted for the fabrication of the TES structure without the concern of PCM leakage because the PCM is already encapsulated. The TES structure can be fabricated in various shapes: simple pellets, honeycombs for the heat exchanger, and grains that suit the fluid bed; in addition, small TES structures of the order of sub-microns or several millimeters that cannot be fabricated via macro-encapsulation can be fabricated using this concept. The bottom-up design employing the alloy MEPCM has the potential to be utilized in novel TES techniques for high temperature applications.

Sintering agent was adopted to fabricate latent heat storage structure in simple way. The melting point of the core of Al-Si alloy MEPCM used in this paper is 577°C. Latent heat storage (LHS) is performed over the melting temperature of the PCM, thus operating temperature become higher than the temperature. Sintering temperature is also

needed to be higher the temperature for the LHS structure to maintain its shape. On the other hand, too higher temperature than the melting temperature can cause breaking of capsule by thermal expansion of inside core. Because of these reasons, sintering temperature desires to be higher than the melting temperature and lower than the breaking temperature of MEPCM shell. Firstly, I selected glass frit (GF) with a low sintering temperature as a sintering aid. The result of the LHS pellets composed MEPCM and GF is reported in chapter 2.2. Then, I tried to fabricate LHS pellets with sinterable alumina (SA) with a higher sintering temperature. This result is reported in chapter 2.3.

2.2.1 Experimental procedure: Fabrication of heat storage pellets with MEPCM and glass frit

2.2.1.1 Materials

Microparticles of Al-25mass%Si with a mean diameter of 36.3 μm were prepared via the spinning disk atomization method (Hikari Material Industry Co. Ld., purity: 99.0 %, T_m: 577 °C, L: 432 J g^{-1}). They were used as raw materials.

$Al(OH)_3$ powder (Kojundo Chemical Laboratory Co., Ltd, Purity: 99.99%) was used as an additive to form a stable shell of MEPCM.

GF that consisted of SiO_2, B_2O_3, ZnO, BaO, Al_2O_3, and La_2O_3 was used as a sintering agent to prepare the latent heat storage pellet.

2.2.1.2 Preparation of MEPCM

As a main material for the PCM composite, the final product, a MEPCM precursor, and MEPCM were prepared following the method reported in the previous study [1]. First, a boehmite treatment of the Al-25 mass% Si particles was conducted in boiling distilled water. 3.33 g L^{-1} $Al(OH)_3$ was added at a constant pH of 8 for 3 h, to form a precursor shell on the surface. The pH value was adjusted by adding $NH_3 \cdot H_2O$ to the

solution. The solution was then cooled to 75 °C, and was maintained at this temperature for 16 h. After filtration and drying, the MEPCM precursor was then obtained. The MEPCM precursor was placed in a rotary kiln and treated via heat-oxidation in an oxygen gas flow (purity 99.5 %, rate 2 L min^{-1}), to form a stable Al_2O_3 shell. Approximately 10 g of the precursor was heated from room temperature to 1150 °C, at a rate of 10 °C min^{-1}, and then maintained at 1150 °C for 6 h. Thus, the MEPCM was obtained.

2.2.1.3 Fabrication of pellet and grain type thermal energy storage composites

Three types PCM composites with different main materials, Al-25mass%Si microsphere, a MEPCM precursor, and MEPCM, were prepared by the same procedure. First, the main materials were weighed to a ratio of 1:1, with GF as a sintering agent. They were then mixed using a planetary ball mill at a speed of 100 rpm for 15 min. The mixed powder was then shaped into cylindrical pellets with diameter of 10 mm and height of 3.3-3.7 mm, by being pressed at 20 MPa at room temperature. Finally, these pellets were heated to 800 °C, and kept at this temperature for 1 h in air.

2.2.1.4 Cyclic test

Cyclic tests were performed on the composites to evaluate their durability by repeating the melting and freezing processes over 300 cycles. These cycles were performed in a tube furnace, with two mobile heaters that could be automatically moved along the tube using an air compressor. One heater was set at 650 °C for melting, and the other heater was set to 400 °C for freezing. In these experiments, the as-prepared composite was set at the center of the tube, and the two heaters were moved to the center in order. The melting and the freezing periods were both set to 1800 s (30 min). In addition, another composite, in which a thermocouple was inserted into the middle of the sample, was also placed next to the test sample, to record the temperature history of the composite during the cyclic tests.

2.2.1.5 Characterization

Scanning electron microscopy (SEM, JEOL, JSM-7001FA) and energy dispersive spectroscopy (EDS) were used to characterize the surface structure of the synthesized composites. The phase composition was determined using powder X-ray diffraction (XRD) with a one-dimensional (1D) silicon-strip detector (Rigaku Miniflex600, D/teX Ultra2, Cu Kα). Finally, the thermal properties of the composites were investigated. Their latent heat of fusion was measured using a differential scanning calorimeter (DSC) (Mettler Toledo 823e); the samples were subjected to heating and cooling at the rate of 2 °C min^{-1} in an Ar atmosphere during this process. The thermal diffusivity and specific heat of the composites were measured using a laser flash thermal analyzer (ULVAC, TC-7000). The densities of the samples were measured with an ultrapycnometer (Quantachrome Instruments, Ultrapycnometer 1000).The thermal conductivity was calculated from the thermal diffusivity, the specific heat and the density:

$$\lambda=\alpha\times C_p\times\rho \quad (1)$$

Where λ is the thermal conductivity, α is the thermal diffusivity, C_p is the specific heat and ρ is the density.

2.2.2 Results

2.2.2.1 Structural characterization of the composites

Figure 2-1 shows overviews of the composites prepared from a) Al-Si microsphere/GF, b) MEPCM precursor/GF, and c) MEPCM/GF. The appearance of Al-Si microsphere/GF composites was remarkably different from all of the others. As shown in Fig. 2-1 a), metallic spherical agglomerations with diameters of 0.22-0.61 mm

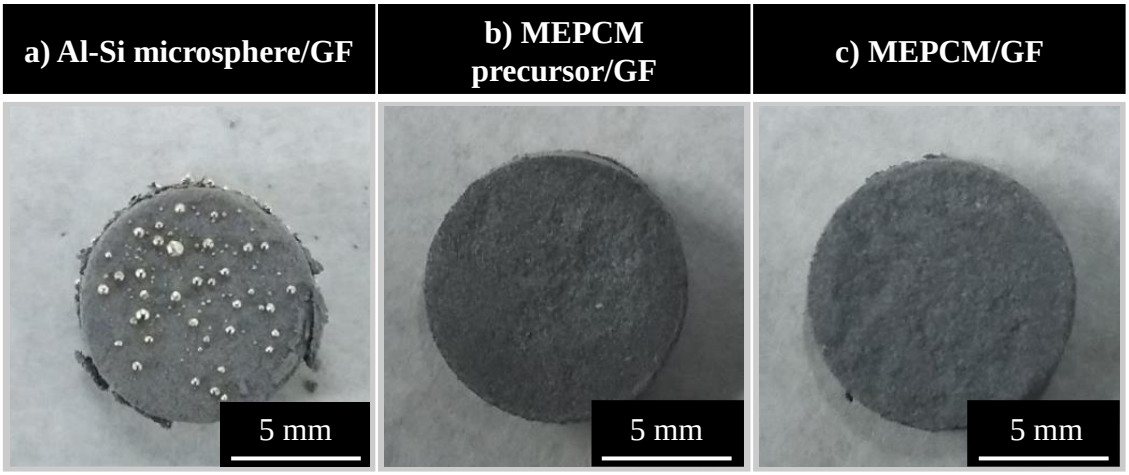

Figure 2-1 Overviews of the composites prepared from a) Al-Si microsphere/GF, b) MEPCM precursor/GF, c) MEPCM/GF.

are clearly visible on the surface of the Al-Si microsphere/GF composites. In Figs. 2-1 b) and c), however, the MEPCM precursor/GF and MEPCM/GF composites do not have metallic agglomerations, their pellet shapes have remained intact.

Figure 2-2 shows 1) SEM images and 2) results of elemental mapping of the cross-sections of a) Al-Si microsphere/GF, b) MEPCM precursor/GF, and c) MEPCM/GF. The EDS mapping reveals that, for all of the composites, the circle structures, which consisted of Al and Si with diameters of ~10–40 μm, were surrounded by oxygen. Clearly, the circle structure came from the core material of Al-25mass%Si. Little Al and Si was detected in the oxygen detected areas, however. Focusing on the results of the Al-Si microsphere/GF composite, in Fig. 2-2 a-2), some of the circle structures were directly connected with other circle structures, without contact through the oxygen phase. In Fig. 3 b-2) and Fig. 2-2 c-2), the Al and oxygen areas overlapped, forming a layer with a thickness of about 1 μm around the circle structures. These consisted of Al and Si. In addition, the spherical structures composed of Al and Si were separated by oxygen layers. No leakage of liquid Al-Si was observed in the EDS

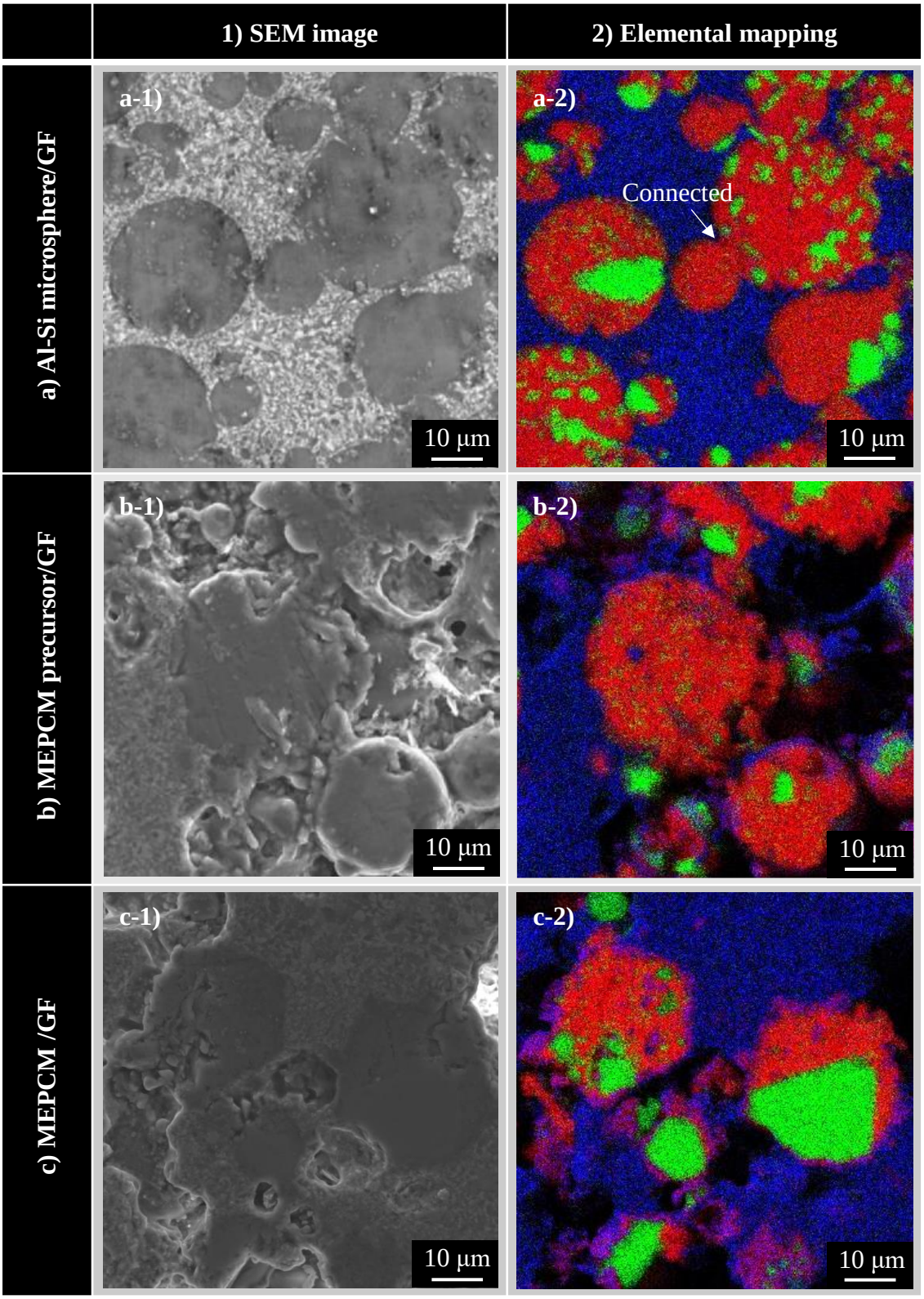

Figure 2-2 1) SEM images and 2) results of elemental mapping of the cross-section of a) Al-Si microsphere/GF, b) MEPCM precursor/GF, and c) MEPCM/GF. In the elemental mappings, red area represent Al, light green area represent Si, and blue area represent Oxygen.

mapping. In particular, oxygen was not detected on the Al-Si core. Therefore, it can be concluded that the oxidation and corrosion of Al-Si in the MEPCM was prevented.

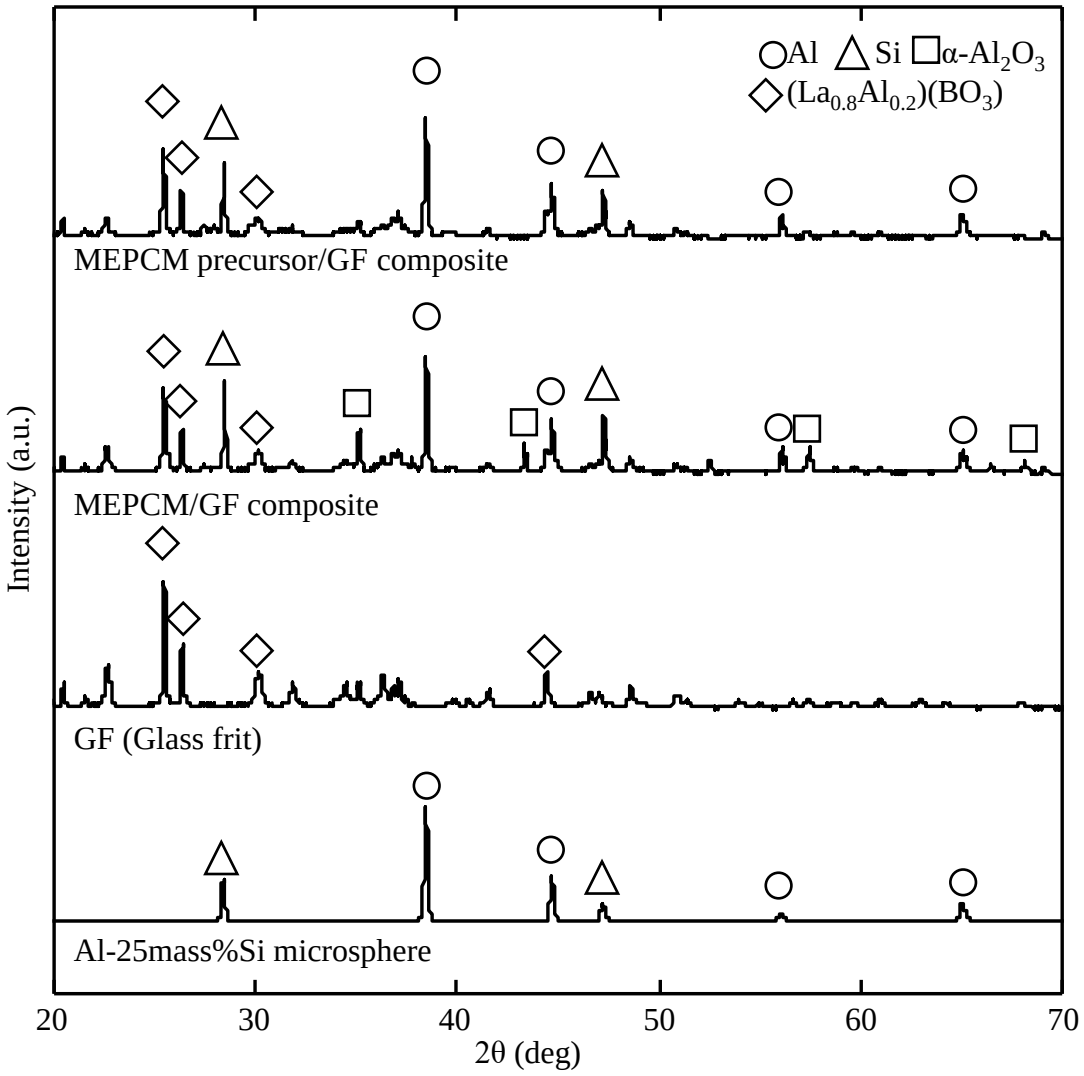

Figure 2-3 XRD spectra of the MEPCM precursor/GF composite and the MEPCM/GF composite, shown together with data from the raw material of Al-25mass%Si microsphere and the sintered GF (at 800ºC for 1 h).

Figure 2-3 shows XRD spectra of the MEPCM precursor/GF composite and the MEPCM/GF composite, shown together with that of the raw material of the Al-25mass%Si microsphere and the sintered GF (at 800 °C for 1 h). Almost all of the detected

peaks correspond to Al, Si, GF, and α-Al_2O_3. In addition, ($La_{0.8}$ $Al_{0.2}$)(BO_3) and SiO_2 were also detected. Al_2O_3 was detected in the MEPCM/GF composites, therefore, it can be inferred that Al and oxygen overlapped in the layer around the core of Al-Si, as can be seen from Fig. 2-2 c), to form α-Al_2O_3.

2.2.2.2 Thermal properties

Table 2-1 lists the thermophysical properties of the MEPCM precursor/GF composite and those of the MEPCM/GF composite. It can be seen from Table 2-1 that the thermal conductivity of the MEPCM precursor/GF composite was 2.16 W m^{-1} K^{-1}, and that of the MEPCM/GF composite was 3.20 W m^{-1} K^{-1}. The thermal conductivity of PCM, Al-25 mass% Si, was 167 W m^{-1} K^{-1} [2]. Thus, the thermal conductivity decreased owing to the microencapsulation and fabrication of the composite. However, these values are higher than those of non-metallic PCMs. The thermal conductivities of inorganic salt eutectics are in the range of 0.4-2.1 W m^{-1} K^{-1}, for instance [3].

Table 2-1 Physical properties of MEPCM precursor/GF composite and MEPCM/GF composite

Composite	Thermal diffusivity (m^2 s^{-1})	Specific heat (kJ kg^{-1} K^{-1})	Density (g m^{-3})	Thermal conductivity (W m^{-1} K^{-1})
MEPCM precursor/GF	8.37×10^{-7}	0.813	3.17×10^{6}	2.16
MEPCM/GF	8.37×10^{-7}	1.27	3.06×10^{6}	3.20

Figure 2-4 shows the DSC curves of the MEPCM precursor/GF composite and the MEPCM/GF composite. Each curve has an endothermic peak around the melting temperature of Al-Si (MEPCM precursor/GF composite: 576.5 °C, MEPCM/GF composite: 575.5 °C). Therefore, these peaks represent the solid-liquid phase change of Al-Si. The heat capacity of the MEPCM precursor/GF composite was 122 J g^{-1} and that

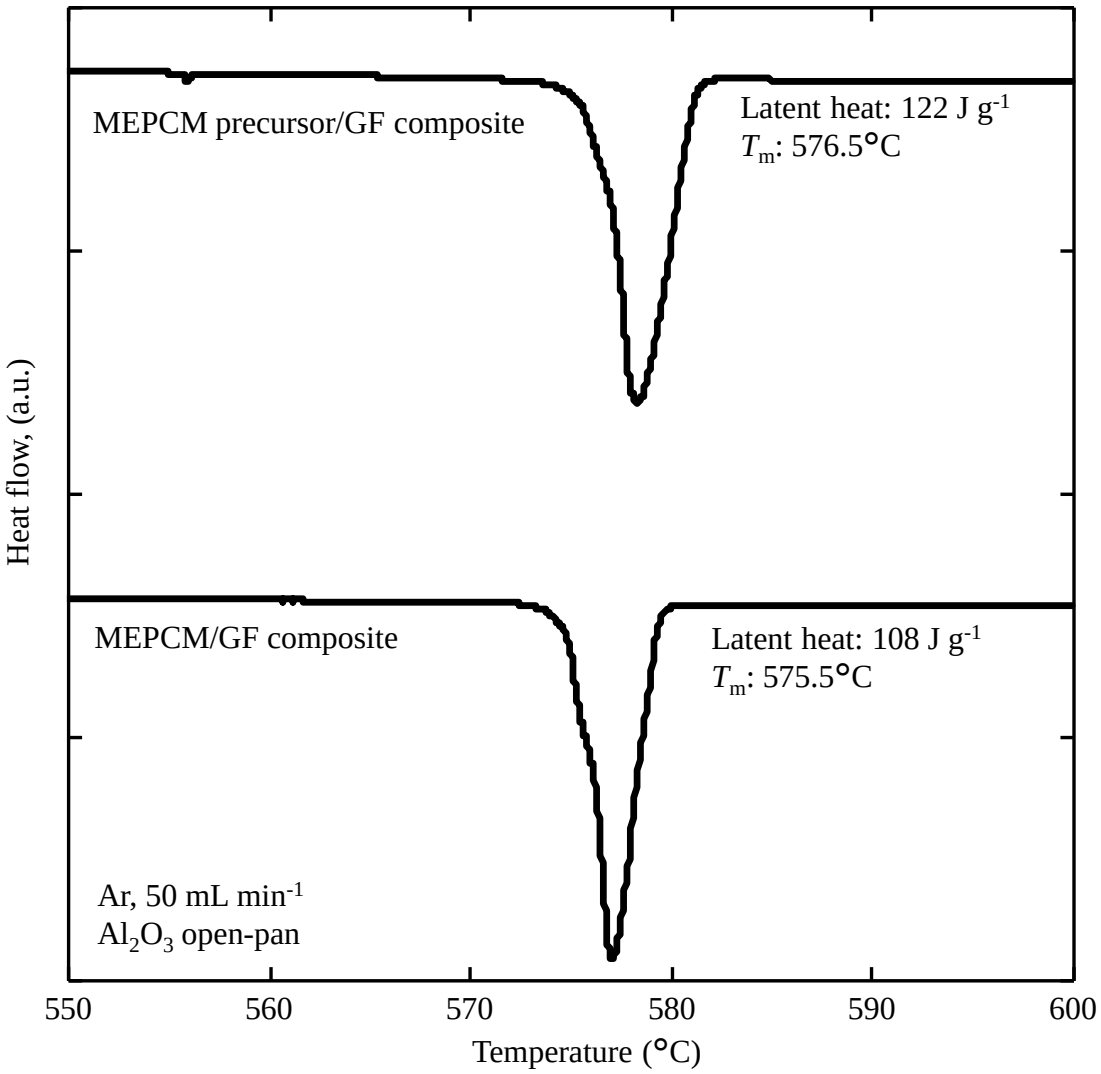

Figure 2-4 DSC curves of the composites after heat treatment at 800°C for 1 hour.

of the MEPCM/GF composite was 108 J g^{-1}.

2.2.2.3 Cyclic durability

Figure 2-5 shows the temperature histories of the MEPCM/GF composites at the first and 300th melting and freezing cycles. The temperature histories of the composites at the first and 300th cycles have similar curves. During the heating period, the temperature was mitigated at around the melting temperature of PCM, 577 ºC.

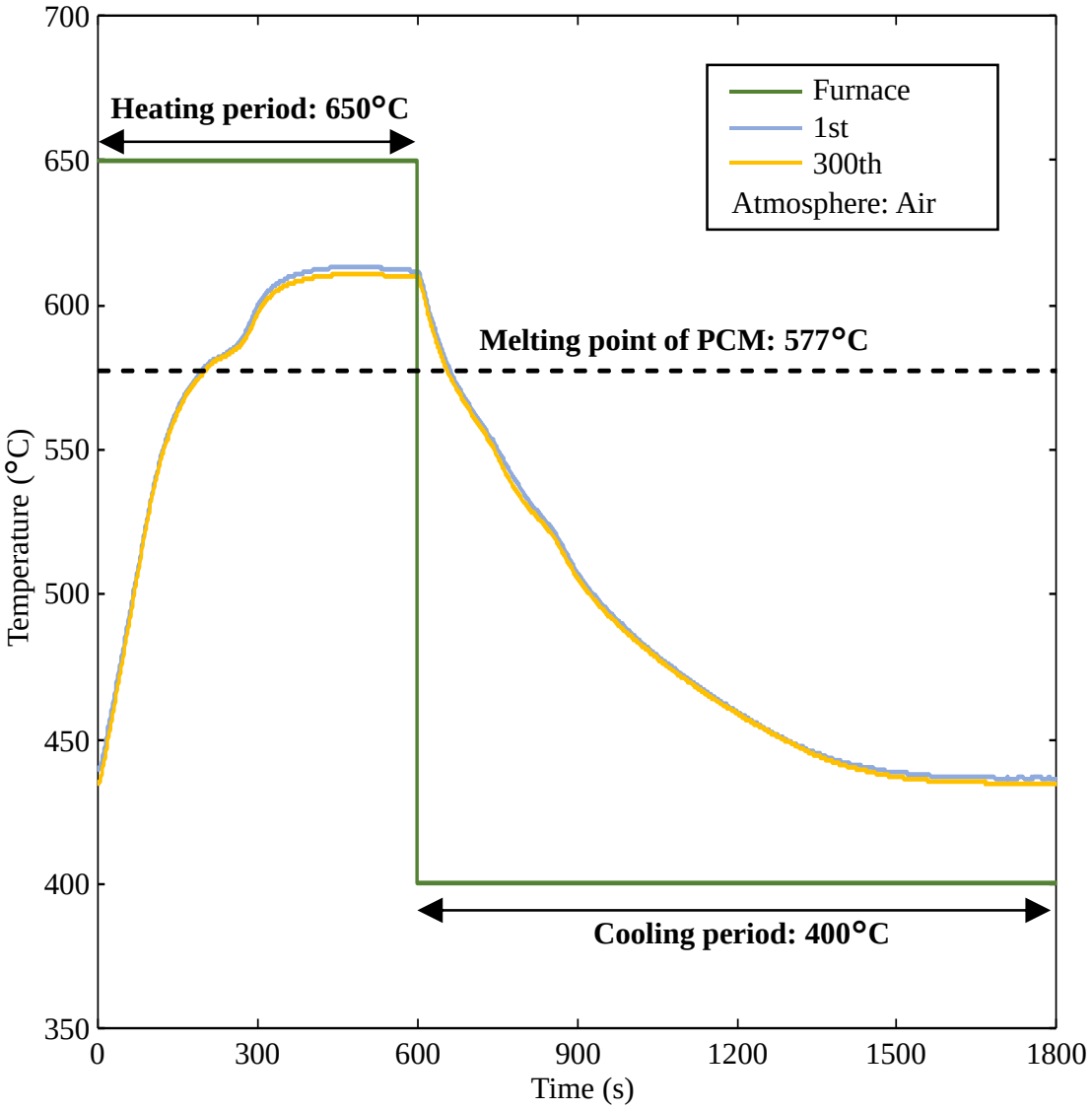

Figure 2-5 Temperature histories of the MEPCM/GF composites after the first and 300th cycles of testing.

During the cooling period, the temperature change was mitigated at ~530–550 ºC. The former mitigation was caused by the melting of the inner PCM, and the latter mitigation was caused by solidification. The temperature change was mitigated at different temperatures during the heating and cooling periods. This represents the supercooling of the PCM. The degree of supercooling is ~20–40 ºC. The temperature history

demonstrates that the melting temperature of the PCM in the MEPCM/GF composite remained steady in the cyclic test; however, the temperature history also shows that MEPCM/GF composite underwent supercooling during the test.

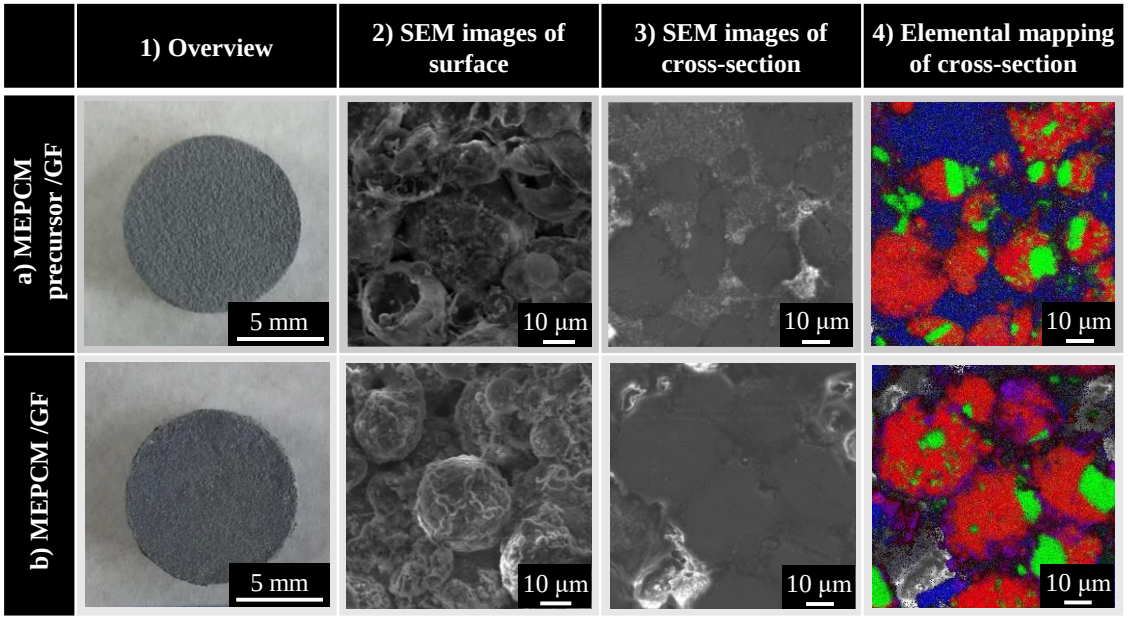

Figure 2-6 1) Overviews, 2) SEM images of surface, 3) SEM images of cross-section, and 4) Elemental mapping of cross-section of a) MEPCM precursor/GF and b) MEPCM/GF composite, after 300 cycles of repeated melting and freezing.

Figure 2-6 shows 1) overviews, 2) SEM images of surface, 3) SEM images of cross-section, and 4) the elemental mapping of cross-sections of a) MEPCM precursor/GF and b) MEPCM/GF composite, after 300 cycles of repeated melting and freezing. Focusing on the MEPCM precursor/GF composite, although many capsules seemed to be broken in Fig. 2-6 a-2), no remarkable change, such as the leakage or the agglomeration of the PCM (see Fig. 2 a), was observed, as shown in Fig. 2-6 a-1). In addition, the inside of the composite, in Fig. 2-6 a-3, 4), also showed no remarkable change, compared with those of the as prepared composite (see Fig. 3 b-1, 2)). Focusing on the MEPCM/GF composite, neither any remarkable change, such as the leakage of the PCM or the

agglomeration of the PCM in Fig. 2-6 b-1), nor the broken capsule in Fig. 2-6 b-2), were observed. In comparison to Fig. 2-2 c-1, 2) and Fig. 2-6 b-3,4), the composite had no remarkable change inside before and after the cyclic test.

After the cycle durability tests, no remarkable changes were observed in either the MEPCM precursor/GF or the MEPCM/GF composites, as shown in Fig. 2-6. Figure 2-5 also shows that the temperature histories did not change between the first and 300th test cycles. The heat capacity of the MEPCM precursor/GF composite was 87% of the as-prepared composite. On the other hand, that of the MEPCM/GF composite was 93% of the as-prepared composite. Both composites had the same melting temperature before and after the cyclic test. The latent heat of the MEPCM precursor/GF composite decreased by some broken capsules of the MEPCM precursor/GF composite shown in Fig. 2-6 a-2) whereas that of the MEPCM/GF composite hardly changed. Thus, it can be concluded that the MEPCM/GF composite has better cyclic durability than the MEPCM precursor/GF composite.

2.2.3 Discussions

The sintering temperature (800 °C) during the preparation of the composites is higher than the melting temperature of the PCM (577 °C). Some leakage of the liquid PCM was therefore expected. As shown in Fig. 2 a), metallic spherical agglomerations were observed in the Al-Si microsphere/GF composite. However, the MEPCM precursor/GF and MEPCM/GF composites had no leakage. These results indicate that the existence of a shell, even that of a precursor such as AlOOH, is important for preventing the leakage of the PCM. This is vital to fabricating a PCM composite from a powder-based PCM. The shell prevented the liquid PCM cores from directly contacting each other and agglomerating.

In Fig.2-3, no new phase, that is, no phase other than those of the MEPCM precursor and the MEPCM/GF, was detected in either the MEPCM precursor or the MEPCM/GF composites. This result indicates that neither the shell of the MEPCM precursor, nor the MEPCM, reacted with the GF. This means that the MEPCM precursor and the MEPCM shell have excellent chemical stabilities

In table 2-1, the thermal conductivity values of the composites proposed herein represent the thermal conductivities of heat storage structures, not those of materials, which is the case with regard to inorganic salt eutectics. The latter require encapsulation, and an additional encapsulation step can cause their thermal conductivity to decrease. In contrast, the PCM in these composites was already encapsulated. Therefore, they can be directly inserted to a heat storage unit without additional encapsulation. Thus, it can be said that these composites have good thermal conductivity. To further improve the thermal conductivity of the MEPCM composites, the mass fraction of the MEPCM in composites can be increased. The MEPCM can be combined with metals because the MEPCM has a ceramic shell. The MEPCM/metal composite can be expected to become a TES structure that provides a higher thermal conductivity.

Next, we discuss the heat-storage capacity of the composites. The latent heat of the MEPCM, made via the same process, was found to be 183 J g^{-1} in a previous study [1]. Compared to this value, the latent heat of the MEPCM/GF composite had 59.0% of the sensible heat capacity of the MEPCM(see Fig.2-4). Taking the mass fraction of the MEPCM in the composites into consideration, it can be concluded that the heat storage performance of MEPCM did not degrade after sintering. Figure 2-5 shows a comparison of the heat capacity per mass among the tested products and conventional sensible heat storage (SHS) materials. The heat capacities of the products are measured values, and those of the SHS materials are calculated values. The heat capacities of the SHS materials

were calculated by multiplying the specific heat and the temperature difference (50 K). The differences in the capacities of the two composites result from the differences in the heat capacities of the MEPCM precursor and those of the MEPCM. The two composites have approximately double the heat capacity of the SHS materials. Fig. 2-6 shows a comparison of the heat capacity per volume among the products and SHS materials. The heat capacities of the products were calculated using the densities shown in Table 1 and the heat storage capacities per mass. The heat capacities of the SHS materials per volume are multiples of the heat capacities in shown in Fig. 2-5 and the densities of the SHS materials. The two composites have approximately 1.5 times the heat capacity per volume of Al_2O_3 as the SHS material. In comparison with the heat capacity of SiO_2, the heat capacity per volume of the MEPCM precursor/GF composite is thrice higher.

Table 2-2 shows a comparison of the thermophysical properties of the PCM composites proposed in this and other papers. The PCM composites fabricated in this paper have excellent thermal energy storage capacities per volume, compared to other types of PCM composites. Moreover, the thermal conductivities of the MEPCM precursor/GF and MEPCM/GF composites compare favorably with other PCM composites. It can be said that the products proposed in this paper are excellent latent heat storage composites for use at temperatures close to 600 °C.

Table 2-2 Comparison of thermophysical properties of PCM composites.

Composite	PCM:Matrix (Mass ratio)	Melting temperature (°C)	Fusion heat ($J\ g^{-1}$)	Fusion heat ($MJ\ m^{-3}$)	Thermal conductivity ($W\ m^{-1}\ K^{-1}$)
MEPCM precursor/ GF	1:1	576.5	122	387	2.16
MEPCM/GF	1:1	575.5	108	330	3.20
Al/Al_2O_3[4]	6:4	655.1	194.2	264.1	2.15
$NaLiCo_3/MgO$[5]	1:1	489.4	177.6	-	2.6
$NaNO_3/Ca(OH)_2$[6]	6:4	306.5	102.8	218.7	-

- means that the thermophysical property was not referred in the citation paper.

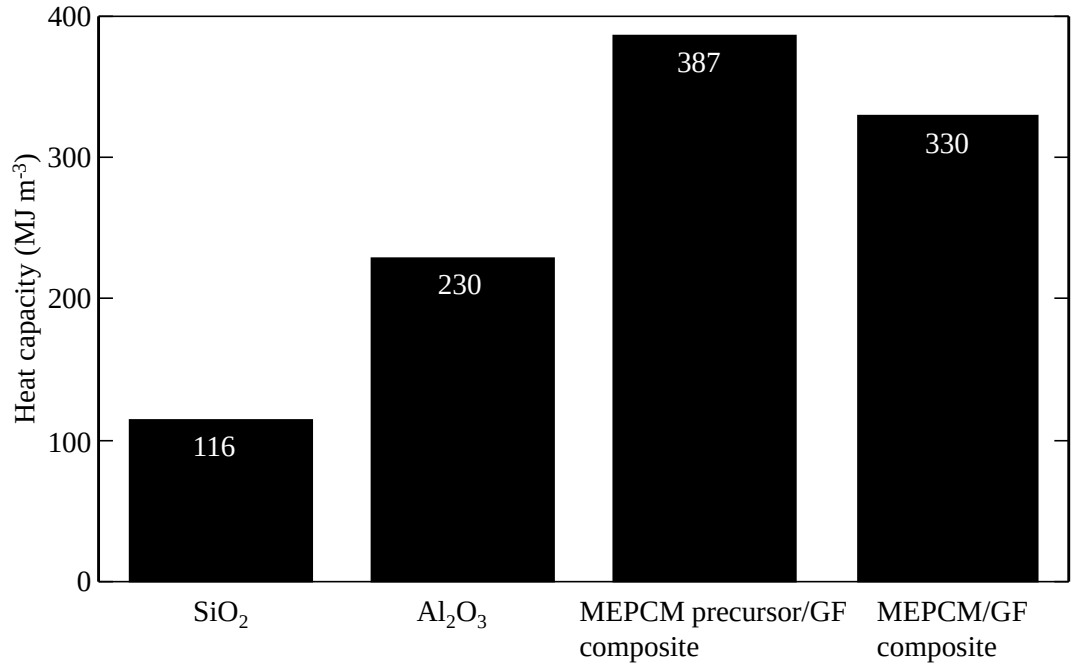

Figure 2-5 A comparison of the heat capacity per mass among the tested products and conventional sensible heat storage (SHS) materials. The heat capacities of the SHS materials were calculated by multiplying the specific heat and the temperature difference (50 K)

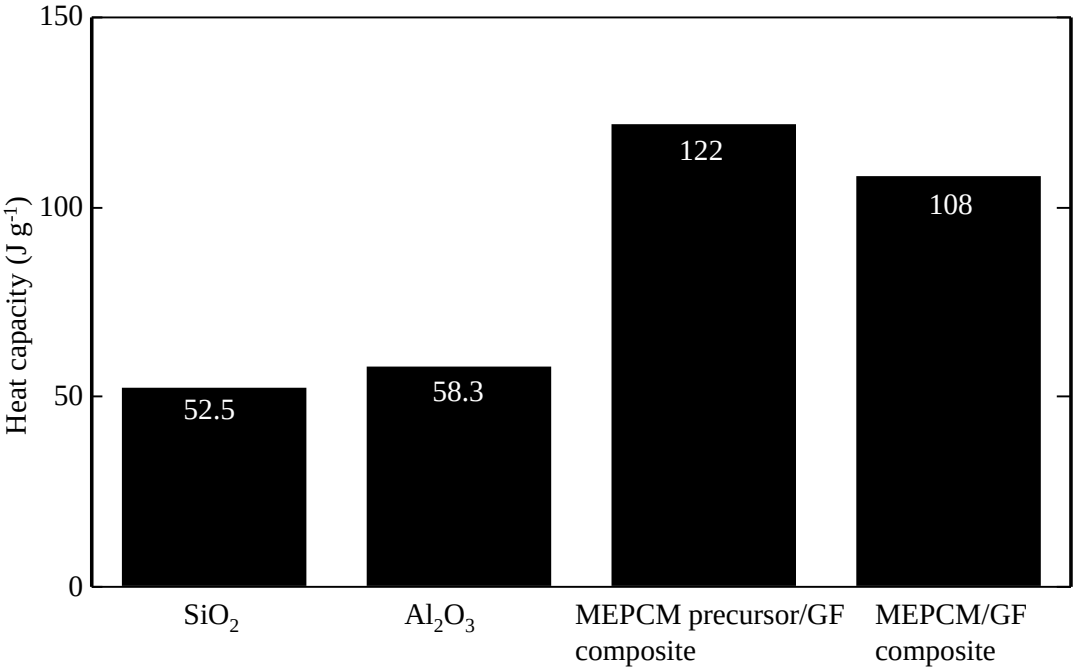

Fig.2-6 A comparison of the heat capacity per volume among the tested products and conventional sensible heat storage (SHS) materials. The heat capacities of the SHS materials were calculated by multiplying the specific heat and the temperature difference (50 K)

2.3.1 Experimental procedure: Fabrication of heat storage pellets with MEPCM and sinterable alumina

2.3.1.1 Materials

Microparticles of Al-25 mass%Si with a mean diameter of 36.3 μm were prepared using the spinning disk atomization method (purity: 99.0 %, T_m: 577 °C, L: 432 J g^{-1}, Hikari Material Industry Co. Ld.). They were used as raw materials.

$Al(OH)_3$ powder (Kojundo Chemical Laboratory Co., Ltd, Purity: 99.99%) was used as an additive to form the stable shell of MEPCM.

Sinterable alumina (SA) (2.44 μm, purity 99.87%, purchased from Nippon Light Metal Co. Ltd.) was used as a matrix material for the heat storage pellets.

2.3.1.2 Preparation of MEPCM precursor

A MEPCM precursor was prepared following a previously-reported method[1]. Firstly, boehmite treatment of the Al-25 mass% Si particles was conducted in boiling distilled water. 3.33 g L^{-1} $Al(OH)_3$ was added at a constant pH of 8 for 3 h, to form a precursor shell on the surface. The pH value was adjusted by adding $NH_3 \cdot H_2O$ to the solution. The solution was then cooled to 75 °C and this temperature was maintained for 16 h. After filtration and drying, the MEPCM precursor was then obtained.

2.3.1.3 Fabrication of heat storage pellets

The MEPCM precursor and SA were mixed, pressed, sintered, and finally heat storage pellets were prepared. Firstly, MEPCM precursor and the SA were weighed at 1:1 and mixed with a planetary ball mill at a speed of 100 rpm for 15 min. Then the mixed powder was shaped into cylindrical pellets with diameter of 10 mm and height of 3.2–3.4 mm by pressing at room temperature at 20 or 50 MPa. Finally, the green pellets were heated to 1300 °C and this temperature was maintained for 3 h under air or atmospheric

O_2. For simplicity, hereafter, the fabricated heat storage pellets are labeled as "x MPa-atmosphere" where x means the pelletized pressure and atmosphere is sintering atmosphere; air or O_2. Table 2-3 shows the list of the products. For example, 20 MPa-air means heat storage pellets pelletized at 20 MPa and sintered under air atmosphere.

2.3.1.4 Characterization

Scanning electron microscopy (SEM, JEOL, JSM-7001FA) and energy dispersive spectroscopy (EDS) were used to characterize the surface structure of the synthesized composites. The phase composition was determined using powder X-ray diffraction (XRD) with a one-dimensional (1D) silicon-strip detector (Rigaku Miniflex600, D/teX Ultra2, Cu Kα). Their latent heat of fusion was measured using a differential scanning calorimeter (TG-DSC) (Mettler Toledo TGA-DSC-3); the samples were heated and cooled at rate of 5 °C min^{-1} in an Ar atmosphere during this process.

2.3.2 Results

2.3.2.1 Structural characterization of the heat storage pellets

Figure 2-7 shows images of the heat storage pellets (which consisted of MEPCM and SA) when pelletized and sintered under different pressures and atmospheres, respectively: (a) 20 MPa-air, (b) 20 MPa-O_2, (c) 50 MPa-air and (d) 50 MPa-O_2. Despite having a higher sintering temperature than the melting temperature of the MEPCM, no agglomerations of metal were observed on the surface of the pellets. The sintering temperature was higher than 1000 °C. Leakage or combustion of liquid PCM was expected at this high sintering temperature. However, as shown in Figure 2-7, agglomeration of metal was not observed and these pellets maintained their shape after sintering.

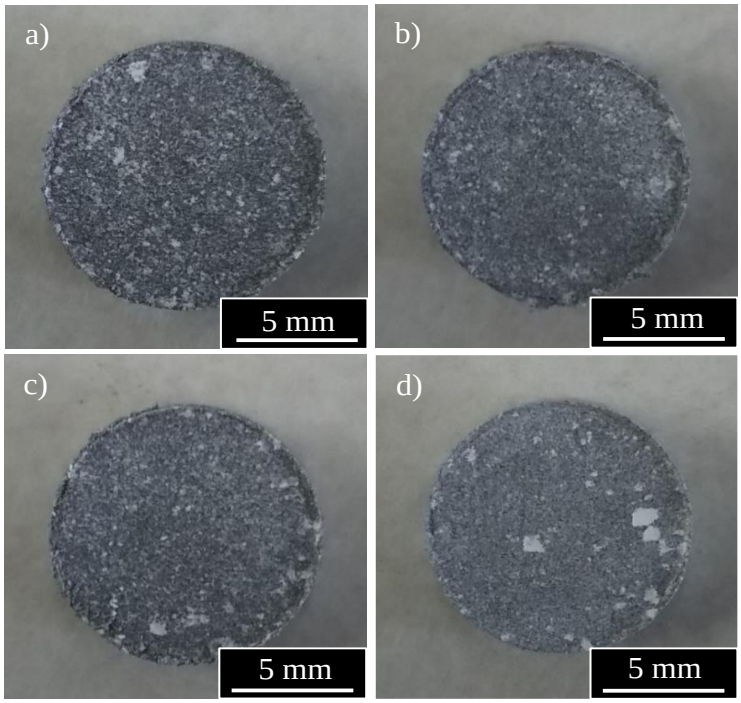

Figure 2-7 Images of heat storage pellets which consisted of MEPCM and SA when pelletized and sintered under different pressure and atmosphere, respectively. a) 20 MPa-air, b) 20 MPa-O_2, c) 50 MPa-air and d) 50 MPa-O_2.

Figure 2-8 shows SEM images of the pellets fabricated under different conditions. Figure 2-8 shows that each pellet had a spherical structure with nearly the same diameter of raw PCM inside. This result indicates that some MEPCM kept their spherical shape in the heat storage pellets. Figure 2-9 shows SEM images and elemental mappings of the cross section of the pellets pelletized at 20 MPa. a-1, 2) sintered under air atmosphere and b-1, 2) O_2 atmosphere. In Figure 2-9-b) and 2-9-d), red areas represent Al and blue areas represent O. Purple areas in which Al and O coexist, represent the presence of Al_2O_3. There are some regions where O doesn't exist in Figure 2-9 a-2) and Figure 2-9 b-2). In other words, some Al and Si doesn't coexist with O. Therefore, elemental mapping suggests that not all the Al and Si in the pellets were oxidized. These results show that some PCM was not oxidized during sintering operation at high temperature.

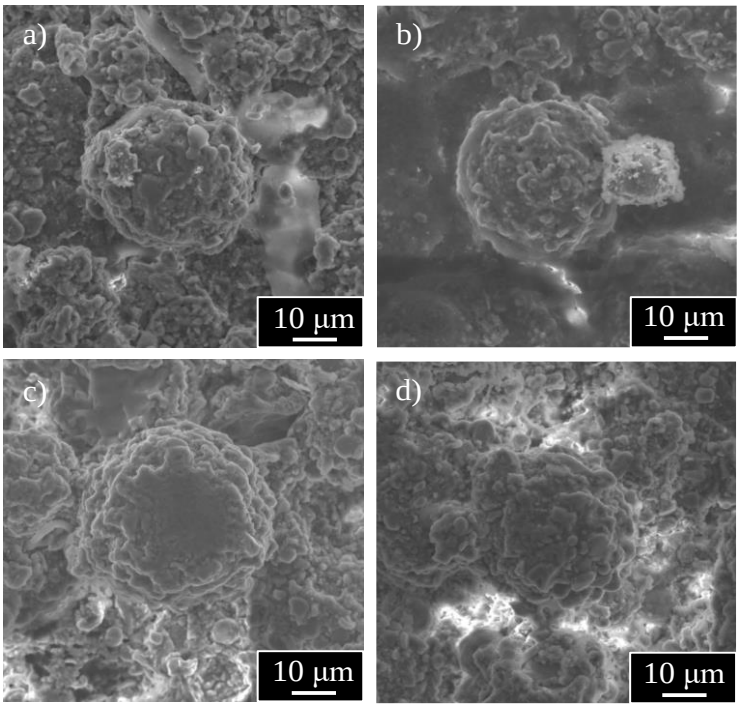

Figure 2-8 SEM images of the pellets fabricated different condition. a) 20 MPa-air, b) 20MPa-O_2, c) 50 MPa-air and d) 50 MPa-O_2.

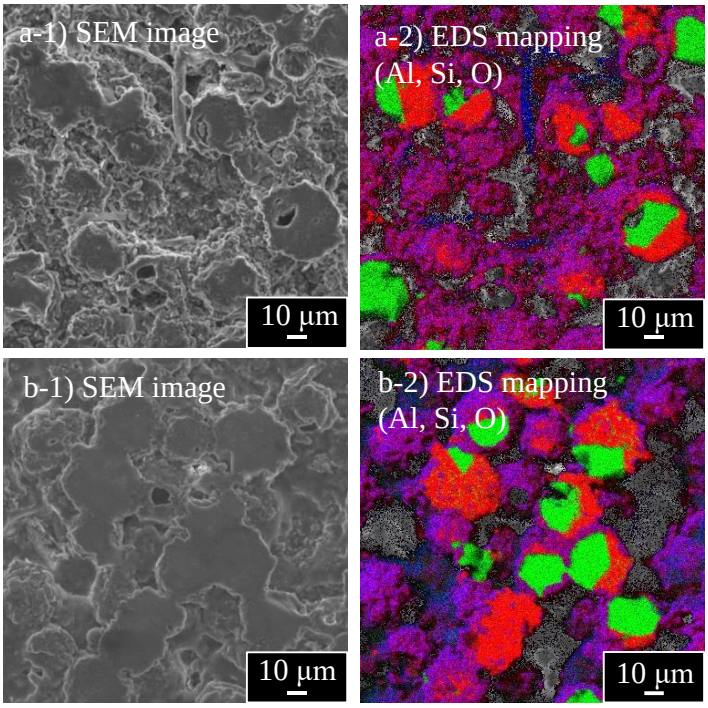

Figure 2-9 SEM images and elemental mappings of the cross section of the pellets pelletized at 20 MPa. a-1, 2) sintered under air atmosphere and b-1, 2) O_2 atmosphere. Red area represent Al, light green area represent Si, and blue area represent O.

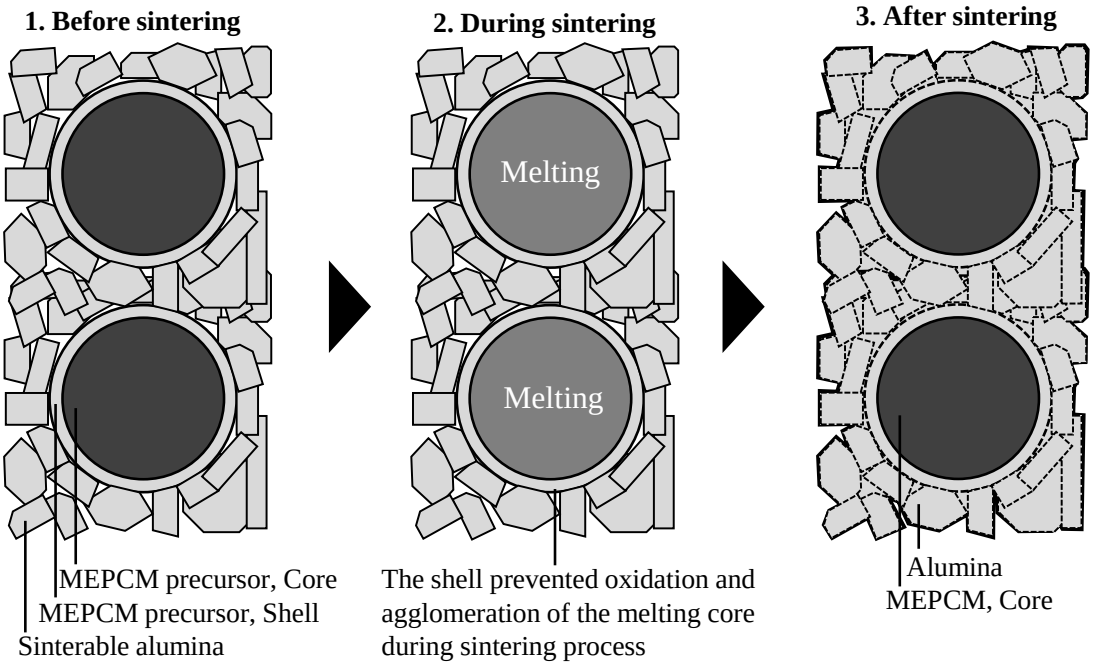

Figure 2-10 Schematic images inside latent heat storage pellets before, during and after the sintering.

Figure 2-10 shows schematic images inside products before, during and after the sintering process. The shell of the MEPCM prevented the melting core from oxidation. The shell also prevented direct contact of each melting core. Thus, Al-Si alloy remains inside the products and agglomeration of metal was not observed.

Figure 2-11 shows XRD patterns for heat storage pellets: a-1) 20 MPa-air, b-1) 20 MPa-O_2, c-1) 50 MPa-air and d-1) 50 MPa-O_2. Figure 5 also shows XRD patterns of sinterabe alumina. Al, Si, and α-Al_2O_3 were detected in all the pellets. Figure 2-11 a, b, c, d, e-2) are magnified XRD patterns of the products from 20° to 24°. The XRD spectra of each composite shows that Al_2O_3 was detected in the heat storage pellets, therefore Al and O overlapped as α-Al_2O_3. The heat storage pellets, excluding the pellets pelletized at 20 MPa and sintered under O_2 atmosphere, also show the presence of SiO_2. This suggests that the Si in the PCM was oxidized in the pellets which were sintered under air atmosphere or pelletized at high pressure.

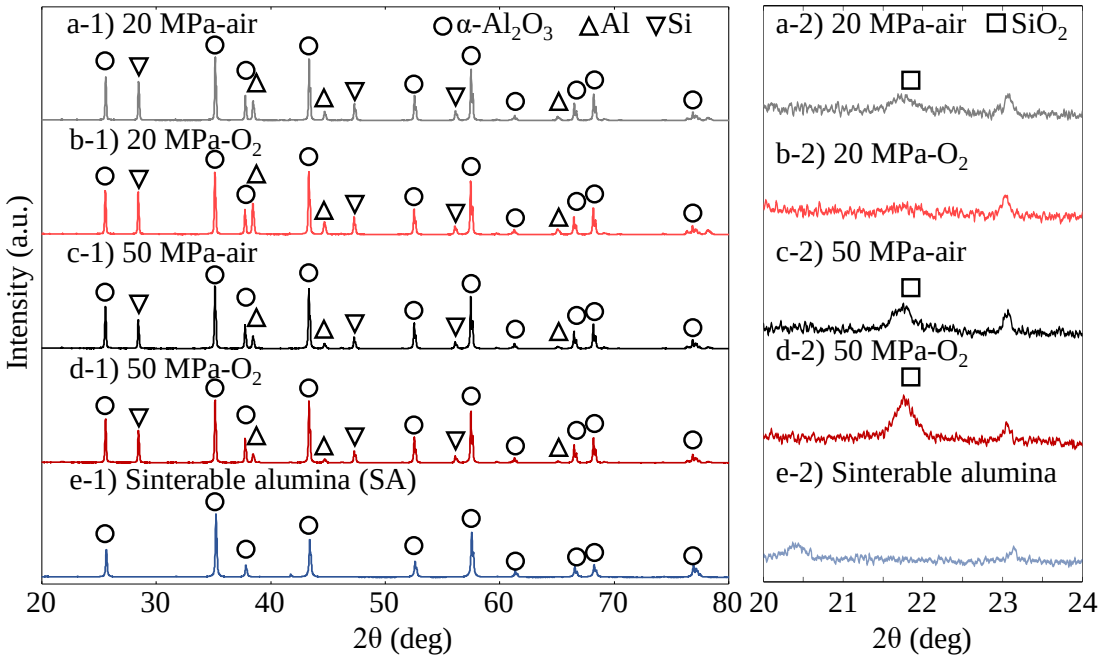

Figure 2-11 XRD patterns for heat storage pellets. a-1) 20 MPa-air, b-1) 20 MPa-O_2, c-1) 50 MPa-air and d-1) 50 MPa-O_2 with e-1) XRD patterns of sinterable alumina.

a, b, c, d, e-2) magnified XRD patterns of the products from 20°to 24°.

2.3.2.2 Thermal properties

Figure 2-12 shows DSC curves for the heat storage pellets: a) 20 MPa-air, b) 20MPa-O_2, c) 50 MPa-air and d) 50MPa-O_2. Each curve had an endothermic peak at around 577 °C, the melting temperature of Al-Si,. Therefore, these peaks are solid-liquid phase transitions for Al-Si. Figure 2-13 shows fusion heat of the heat storage pellets shown in Figure 2-12. The heat storage pellets, a) 20 MPa-air, b) 20 MPa-O_2, c) 50 MPa-air and d) 50 MPa-O_2, has 46.1 J g^{-1}, 73.5 J g^{-1}, 24.4 J g^{-1} and 23.8 J g^{-1} heat storage capacity respectively.

The heat storage pellets, 20MPa-O_2, that were pelletized at 20 MPa and sintered under O_2 atmosphere had the highest heat storage capacities. Heat storage capacity was

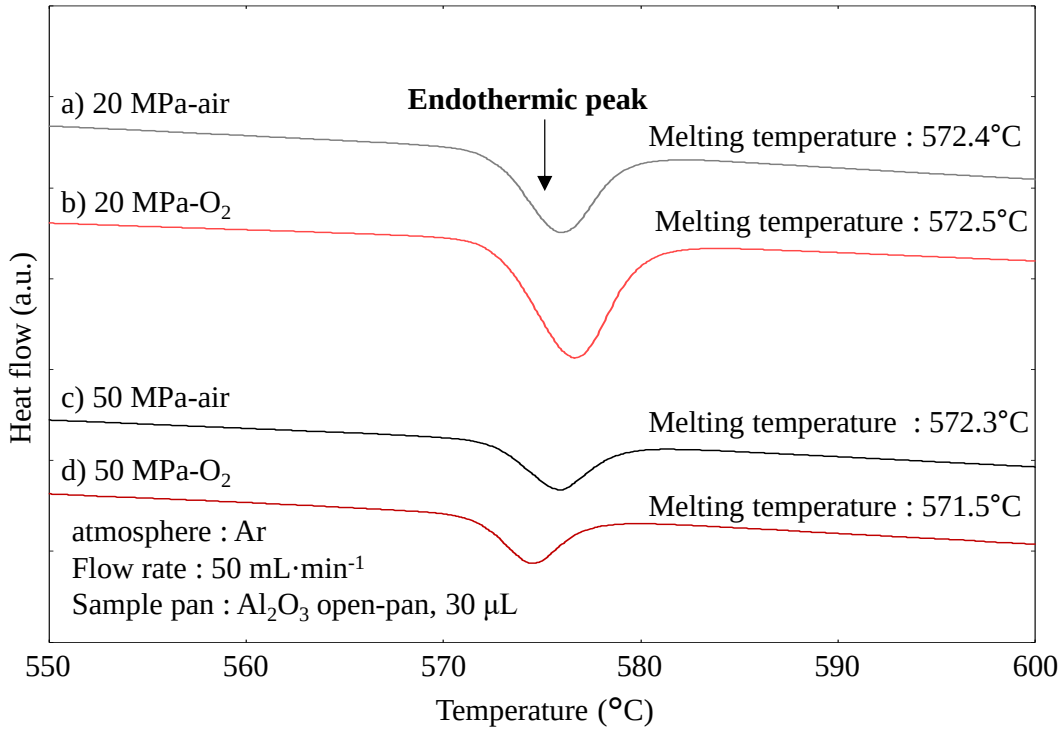

Figure 2-12 DSC curves for the heat storage pellets.

a) 20 MPa-air, b) 20 MPa-O_2, c) 50 MPa-air and e) 50 MPa-O_2.

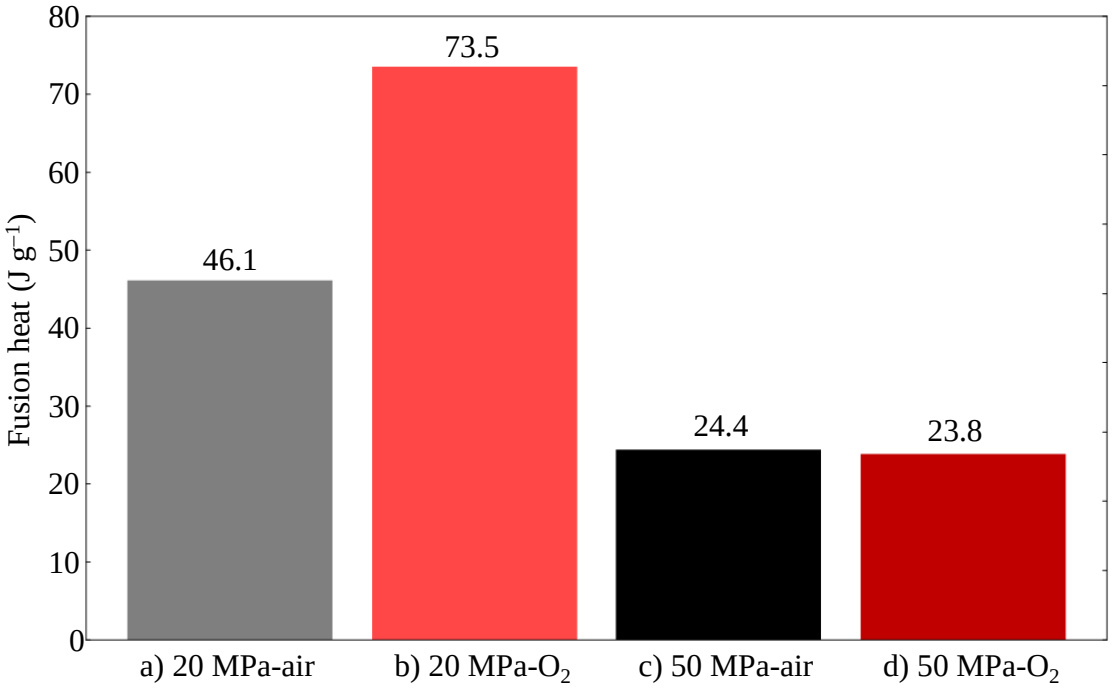

Figure 2-13 Fusion heat of the heat storage pellets shown in Figure 2-12.

a) 20 MPa-air, b) 20 MPa-O_2, c) 50 MPa-air and e) 50 MPa-O_2.

decreased by oxidation of PCM inside the heat storage pellets. In this study, latent heat decrease was prevented when the heat storage pellet was pelletized at 20 MPa and sintered under O_2 atmosphere.

2.3.3 Discussions

Reasons for this why this condition prevented oxidation of PCM are considered. To observe the mass increase, which depends on the atmosphere during sintering, TG analysis was performed of as prepared mixed powders of MEPCM precursor and SA under air or O_2 flow. Figure 2-14 shows the result of the TG analysis. The temperature program and atmosphere were kept same as the sintering condition. There was little difference between the two atmospheres until about 1000 °C. We observed mass decrease at around 200 °C and mass increase started at around 590 °C. Above 1000 °C the rate of mass increase under air flow was higher than the rate under O_2 flow. Finally, there was a 2% difference in the maximum value of the weight change between air and O_2.

SA is stable material, thus the mass change in the TG curve is derived from MEPCM. Our previous study[1] reported mass decrease due to dehydration of $Al(OH)_3$ and mass increase due to oxidation of Al during the heat treatment of the MEPCM precursor. In the final stage of MEPCM shell formation, cracks on the MEPCM surface (caused by heat expansion of the core) are closed by Al oxidation. This is a self-repair process. Figure 2-15 shows a schematic diagram of self-repair process. This self-repair prevents further oxidation of the inner core during heat treatment and the process progresses more rapidly in atmospheres of higher partial pressure of O_2. Figure 2-14 shows that, over 1000 °C, there is a difference in the mass increase of the samples, depending on the atmosphere. Differences in the rate of self-repair in each atmosphere

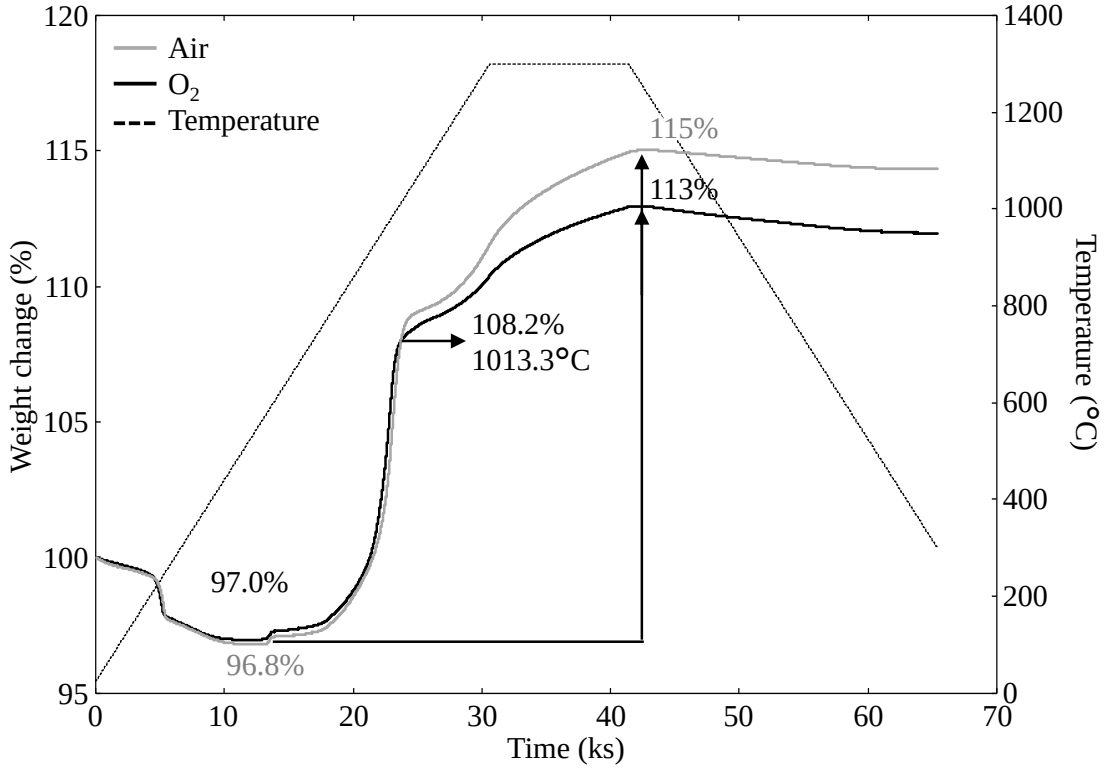

Figure 2-14 TG curves of mixed powders of MEPCM precursor and SA under air or O_2 flow.

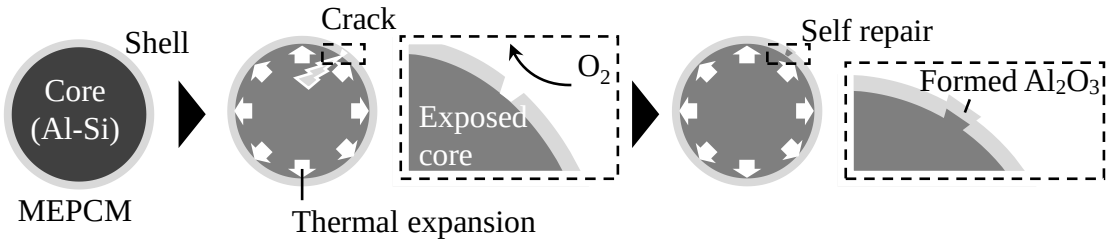

Figure 2-15 A schematic image of self-repair process.

are thought to cause differences in the mass increase. We can see that O_2 atmosphere is advantageous for the preparation of MEPCM and heat storage pellets containing MEPCM. This is because the O_2 atmosphere has a higher partial pressure of O_2 than the air.

The latent heat of the heat storage pellet pelletized at 50 MPa was lower than that of the ones pelletized at 20 MPa. This result indicates that 50 MPa is too high to break MEPCM during the fabrication of heat storage pellets. Cracking of the MEPCM shell

caused more oxidation of the inner core. This is because the ceramic shell helps to prevent oxidation of the inner core. For this reason, high pelletizing pressure is not ideal for the fabrication of MEPCM heat storage pellets.

2.4 Conclusion

Latent-heat storage pellets were successfully fabricated using a microencapsulated metallic PCM. These composites were fabricated with the simple method of mixing the MEPCM and a sintering agent, followed by compression and sintering.

1. The agglomeration of the molten metal was observed in the as-prepared Al-Si microsphere/GF composite because the sintering temperature was higher than the melting temperature of the PCM. However, the MEPCM precursor and the MEPCM prevented agglomeration during sintering.

2. An endothermic peak was observed around the melting temperature of PCM from DSC analysis of the composites. This shows that these composites can be used for latent heat storage.

3. The MEPCM pellets had higher thermal conductivity than non-metallic PCMs. In addition, the latent heat of the pellets showed that the latent heat of the MEPCM did not decrease after the fabrication of the pellets.

4. The thermal history of the MEPCM/GF pellets did not change after 300 cycles of durability testing.

Fabrication of LHS pellets with MEPCM and sinterable alumina were also archived.

5. MEPCM precursor prevented agglomeration and combustion during the sintering step. On the other hand, oxidation of PCM was inevitable and caused loss of latent heat.

2. When sintering temperature is higher than 1000 °C, O_2 atmosphere allows for effective sintering. In addition, pelletizing pressure should be low enough to avoid cracking the MEPCM shell.

3. The heat storage pellet pelletized at 20 MPa and sintered under O_2 atmosphere had highest latent heat, 73.5 J g^{-1}. Following these findings, the next challenge is to increase the heat storage capacity.

This study demonstrates that MEPCM can be used to fabricate latent heat storage composites for high-temperature applications.

References

[1] Sheng N, Zhu C, Saito G, Hiraki T, Haka M, Hasegawa Y, et al. Development of a microencapsulated Al–Si phase change material with high-temperature thermal stability and durability over 3000 cycles. J of Mater Chem A. 2018;6:18143-53.

[2] Fukahori R, Nomura T, Zhu C, Sheng N, Okinaka N, Akiyama T. Macro-encapsulation of metallic phase change material using cylindrical-type ceramic containers for high-temperature thermal energy storage. Appl Energy. 2016;170:324-8.

[3] Nazir H, Batool M, Bolivar Osorio FJ, Isaza-Ruiz M, Xu X, Vignarooban K, et al. Recent developments in phase change materials for energy storage applications: A review. Int J Heat Mass Transfer. 2019;129:491-523.

[4] Xu Y, He Y-L, Zhu G-H, Lv S, Shan B. Al/Al_2O_3 Form-Stable Phase Change Material for High Temperature Thermal Energy Storage. Energy Procedia. 2017;105:4328-33.

[5] Li C, Li Q, Cong L, jiang F, Zhao Y, Liu C, et al. MgO based composite phase change materials for thermal energy storage: The effects of MgO particle density and size on microstructural characteristics as well as thermophysical and mechanical properties. Appl Energy. 2019;250:81-91.

[6] Yu Q, Jiang Z, Cong L, Lu T, Suleiman B, Leng G, et al. A novel low-temperature fabrication approach of composite phase change materials for high temperature thermal energy storage. Appl Energy. 2019;237:367-77.

Chapter 3

Reaction heat control for steam reforming of ethanol with Ni-impregnated latent-heat storage grains

3.1 Introduction

Combining an MEPCM with a catalyst is proposed as an LHS strategy in this chapter. The combination of PCM and a chemical reaction itself was proposed [1-3] in terms of stabilizing the heat source when using waste heat for endothermic reactions. Specifically, it is possible to integrate the catalyst layer with the thermal-storage layer by directly supporting the catalyst on an LHS structure made from an MEPCM. In this case, heat can be exchanged quickly between the catalyst and the heat-storage material. Preventing overheating of the catalyst or combining an unstable heat source and endothermic reaction via heat storage can also be achieved by this strategy. In addition, new reaction systems integrating exothermic and endothermic reactions, and a heat-storage layer could be developed.

In this chapter, the effect of LHS on the stabilization of the catalyst-packed-bed temperature for an endothermic reaction is confirmed. Catalyst–LHS grains were fabricated for LHS applications by loading an MEPCM with catalyst. The catalytic performance of the prepared catalyst–LHS grains for the steam reforming of ethanol (as given in equation (1)) was investigated.

$$C_2H_5OH + 3H_2O \rightarrow 6H_2 + 2CO_2 \quad \Delta H_{298} = 174 \text{ kJ/mol} \qquad (1)$$

Ni was selected as the catalyst for steam reforming of ethanol. The prepared Ni catalyst–LHS grains have the potential to achieve both LHS and catalysis functions simultaneously in a single material. In this study, the catalytic performance of the prepared Ni–LHS grains was evaluated when the power supply to the heating part of the catalytic reactor was stopped to confirm whether they could operate as a heat source for the steam reforming of ethanol.

3.2 Experimental procedure

3.2.1 Materials

Microparticles of Al–25mass%Si with a mean diameter of 36.3 μm were prepared via spinning-disk atomization by the supplier (Hikari Material Industry Co. Ltd.). This material had a purity of 99.0%, melting temperature (T_m) of 577 °C, and latent heat capacity (L) of 432 J g^{-1} and was used as a raw material. $Al(OH)_3$ powder (Kojundo Chemical Laboratory Co., Ltd, Purity: 99.99%) was used as an additive to form a stable shell of MEPCM. Glass frit that consisted of SiO_2, B_2O_3, ZnO, BaO, Al_2O_3, and La_2O_3 was used as a sintering agent to prepare the LHS grains. Nickel nitrate hexahydrate (Kojundo Chemical Laboratory Co., Ltd, Purity: 99.9%) was used as the Ni source of the catalyst supported by the LHS grain. Ethanol (Kanto Chemical Co., Inc., Purity: 99.5%) was used for the steam-reforming experiments.

3.2.2 Preparation of catalyst–LHS composite

The MEPCM was prepared following a method reported in a previous study [4] and Chapter 2. Figure 3-1 shows the process for preparing the catalyst–LHS composite. First, a boehmite treatment of the Al–25 mass% Si particles was conducted in boiling distilled water. The raw Al–Si was added to a solution containing 3.33 g L^{-1} $Al(OH)_3$ at a constant pH of 8 (adjusted using $NH_3 \cdot H_2O$), and allowed to react for 3 h to form a

precursor shell on the surface. The solution was then cooled to 75 °C, and was maintained at this temperature for 16 h. After filtration and drying, the MEPCM precursor was then obtained.

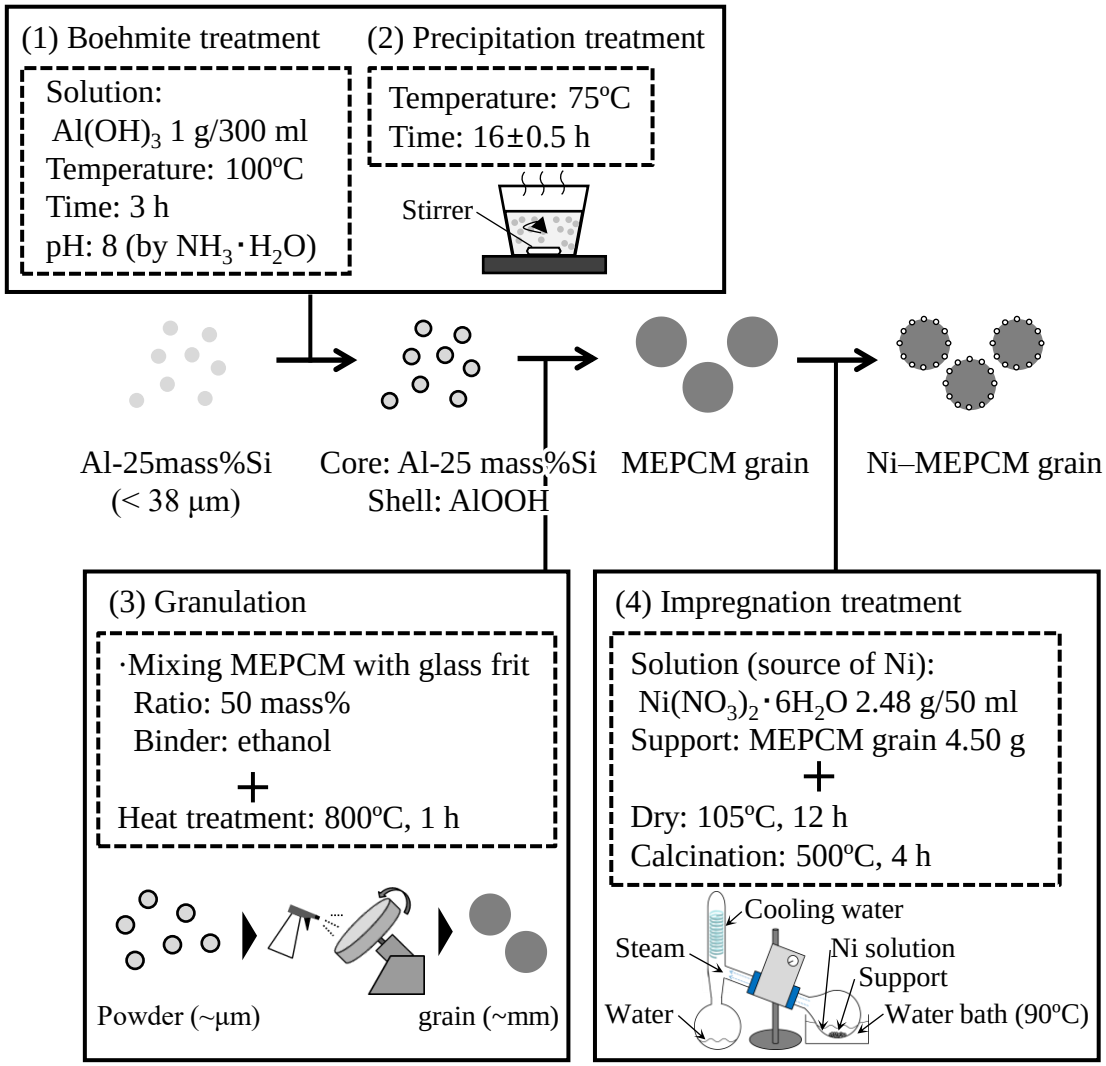

Figure 3-1 Preparation of Ni–LHS grains from Al-25mass%Si via (1) boehmite treatment, (2) precipitation treatment, (3) granulation, and (4) impregnation treatment.

Next, the LHS grains were formed by tumbling granulation. Glass frit and the MEPCM precursor were mixed in a 1:1 weight ratio in a planetary ball mill at 100 rpm for 15 min. The mixed powder was fed into a pan-type rolling granulator and formed

into grains with 1–3 mm diameter using ethanol as a binder. The green samples were heated at 800ºC for 1 h in an air atmosphere to obtain the LHS grains. Ni–LHS composite grains were prepared by impregnation in a rotary evaporator. The nominal mass ratio of Ni was 10 mass%. First, 2.48 g of nickel nitrate hexahydrate was added to 50 ml of distilled water in a flask. Next, 4.50 g of LHS grains were added to the prepared Ni solution, and the solution was heated to 90°C to impregnate the Ni as the water evaporated as the flask rotated. Then, the sample was dried at 105°C for 12 h and calcined at 500°C for 4 h under an air atmosphere. Finally, Ni–LHS composite grains were obtained. For comparison, Ni was also loaded on alumina particles (diameter: 2 mm) by the same impregnation method.

3.2.3 Catalytic performance for steam reforming of ethanol

The catalytic performance of the composite LHS grains was evaluated using a glass tube (diameter: 20 mm) as a reaction chamber, as shown in Figure 3-2. First, 3.5 g of Ni–LHS grains was packed in the glass tube to achieve a catalyst packed bed with a height of 20 mm. Before catalytic tests, the catalyst was reduced in hydrogen at 500°C for 1 h. Then, furnace 1 and 2 above the packed bed layer were heated to 550°C and furnace 3 heating the packed bed was heated to 650°C as shown in Fig 3-2. After the temperature of furnace 3 reached 650°C, a mixture of ethanol and distilled water (molar ratio of 1:5, respectively) was added dropwise using a feed pump (Tokyo Rika Kikai, MP-4000) under Ar flow (200 ml min^{-1}) at a feed rate of 0.1 ml min^{-1}. The droplets of the solution were absorbed by glass wool and vaporized at 550°C before reaching the catalyst. The vapor was continuously flowed through the catalyst packed bed. When the outlet gas reached a constant composition, furnace 3 was turned off and the catalytic test was performed for 30 min. The composition of the outlet gas was analyzed with quadrupole mass spectrometry (Q-mass; Pfeifer Vacuum, Termostar GSD301). The

catalytic activity of the Ni–Al_2O_3 grains was also tested under the same experimental conditions for comparison.

The catalytic performance was evaluated by the hydrogen yield expressed by equation (2).

$$\text{Hydrogen yield: } \frac{F_{\text{out}}}{6F_{\text{in}}} \times 100 \qquad (2)$$

where F_{in} is the inlet flow rate of C_2H_5OH. and F_{out} is the outlet flow rate of hydrogen.

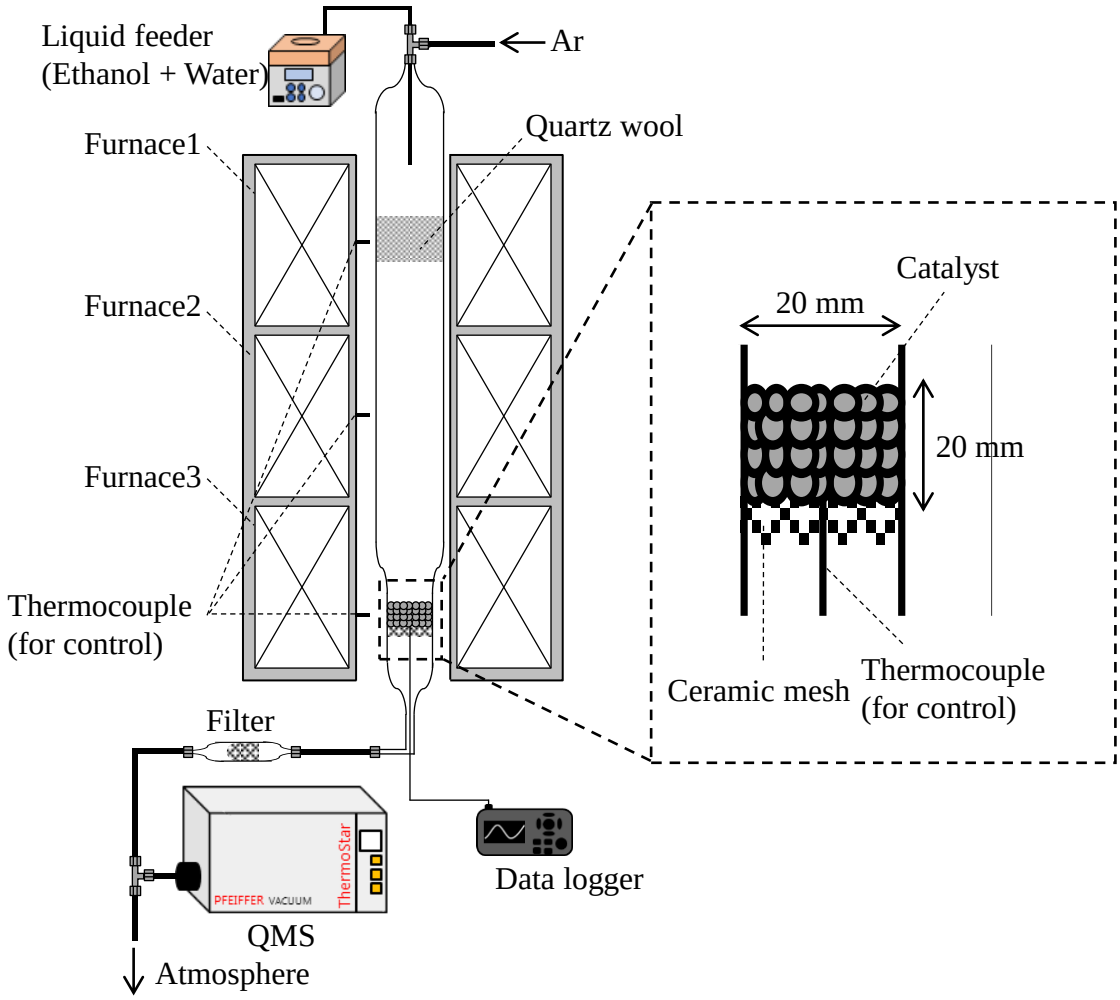

Figure 3-2 Experimental apparatus used to evaluate the catalytic performance of the LHS grains for steam reforming of ethanol.

3.2.4 Characterization

Scanning electron microscopy (SEM; JEOL, JSM-7001FA) and energy dispersive X-ray spectroscopy (EDS) were used to characterize the surface structure of the synthesized catalyst. The phase composition was determined using powder X-ray diffraction (XRD) with a one-dimensional (1D) silicon-strip detector (Rigaku Miniflex600, D/teX Ultra2, Cu Kα). Their latent heat of fusion was measured using thermogravimetry-DSC (TG-DSC; Mettler Toledo TGA-DSC-3); the samples were heated and cooled at rate of 5 °C min^{-1} in an Ar atmosphere during this process.

3.3 Results

3.3.1 Characterization of the as-prepared Ni–LHS grains

Figure 3-3 shows the appearance of the as-prepared LHS grains and Ni–LHS grains. The size of the composite LHS grains ranged from 1 to 3 mm. After impregnation of the catalyst, the color of the surface of the grains changed from gray to black, but the shape and size of the grains did not change significantly. This indicates that the composite LHS grains were sufficiently durable to withstand the impregnation process.

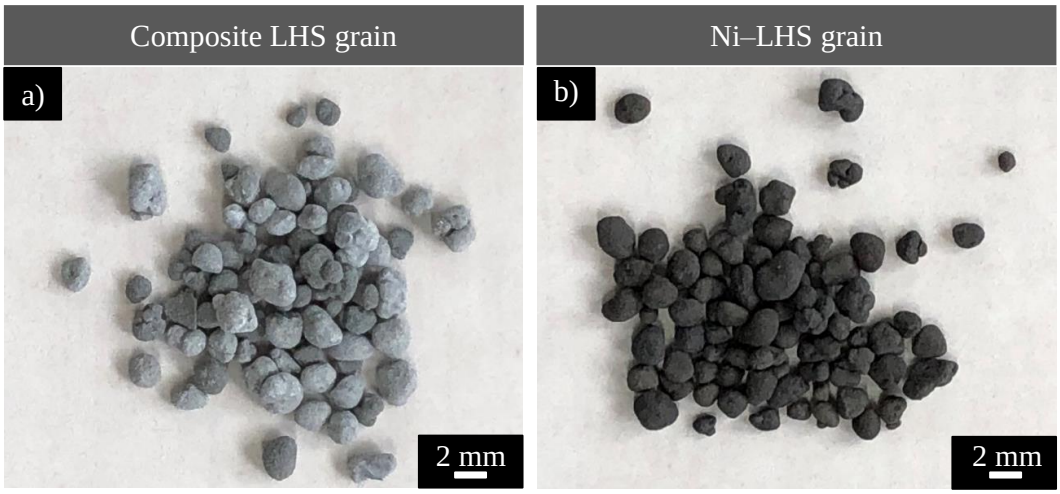

Figure 3-3 Appearance of LHS grains a) before and b) after impregnation treatment.

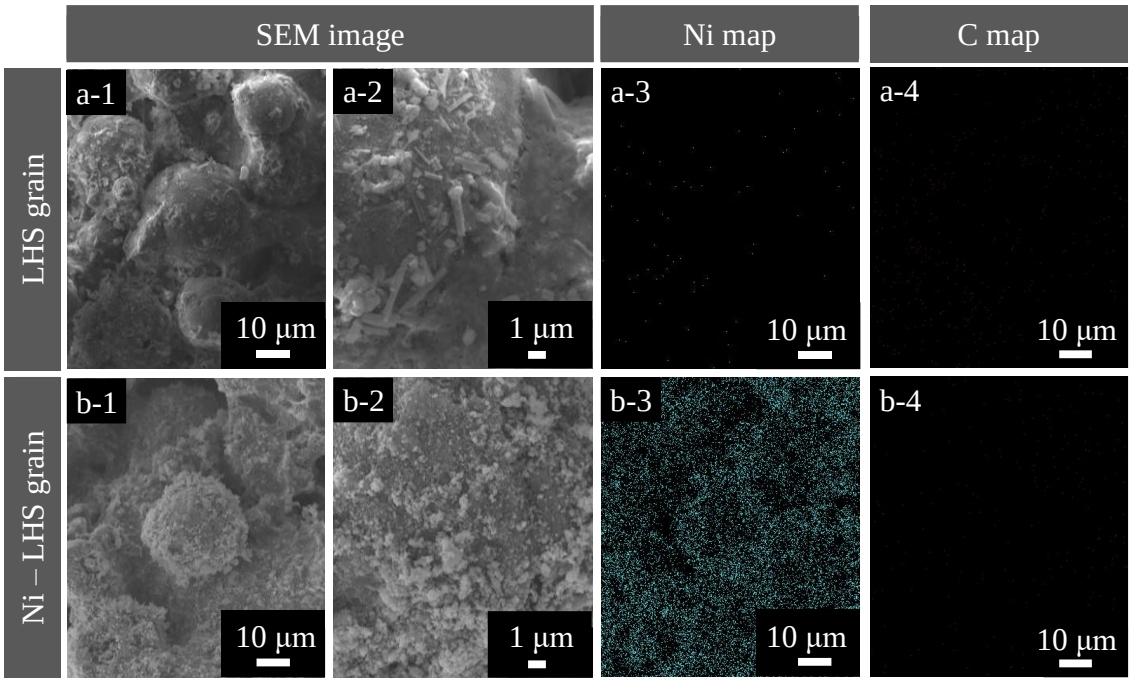

Figure 3-4 SEM images and Ni and C elemental maps of LHS grains a) before and b) after impregnation treatment.

Figure 3-4 shows SEM images and EDS maps of the surface of the Ni–LHS grains before and after impregnation. Spherical MEPCM particles were observed in both samples before and after impregnation. In addition, particles of about 100–200 nm were observed on the surface of the MEPCM after catalyst impregnation. The EDS maps identified that these particles were Ni. In conclusion, the impregnation treatment successfully resulted in Ni catalyst supported on the composite LHS grains.

Figure 3-5 shows the XRD patterns of MEPCM, composite LHS grains, Ni–LHS grains after impregnation, and glass frit used as a sintering aid. In both the LHS and Ni–LHS grains, the Al and Si peaks of the MEPCM were detected. This indicates that the core Al–Si alloy in the formed grains was protected and did not change chemically during the granulation and impregnation processes. A peak corresponding to NiO was detected in the sample after catalyst impregnation. This result indicates that the

Ni nitrate hexahydrate used as the Ni source was oxidized to NiO by calcination at 500°C in air. No new composition other than NiO was detected in the Ni–LHS grains before or after Ni impregnation, and all peaks, except for those corresponding to Al, Si, and NiO were attributed to the glass frit glass sintering aid.

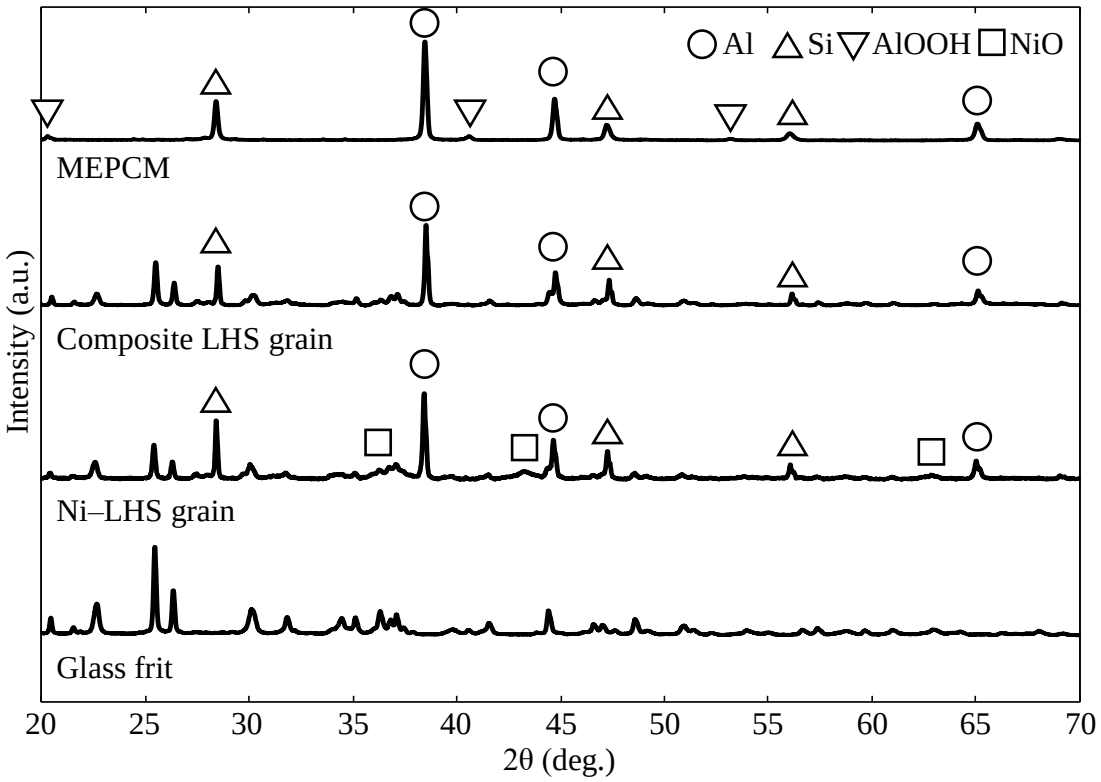

Figure 3-5 XRD patterns of MEPCM, and LHS grains before and after impregnation, and the glass frit for reference.

Figure 3-6 shows the DSC curves of the LHS and Ni–LHS grains measured during cooling from 600 to 500°C. An exothermic peak due to MEPCM solidification was observed in both samples. The latent heat capacity (L) was calculated as the sum of the ΔH of the DSC peaks, giving 78.0 and 69.9 J g^{-1} for the LHS and Ni–LHS grains, respectively. The ~10% decrease in L after Ni loading was consistent with the percentage decrease in the weight ratio of MEPCM after loading 10 mass% Ni. The

solidification temperatures were 557°C and 558°C for the LHS grains and Ni–LHS grains, respectively.

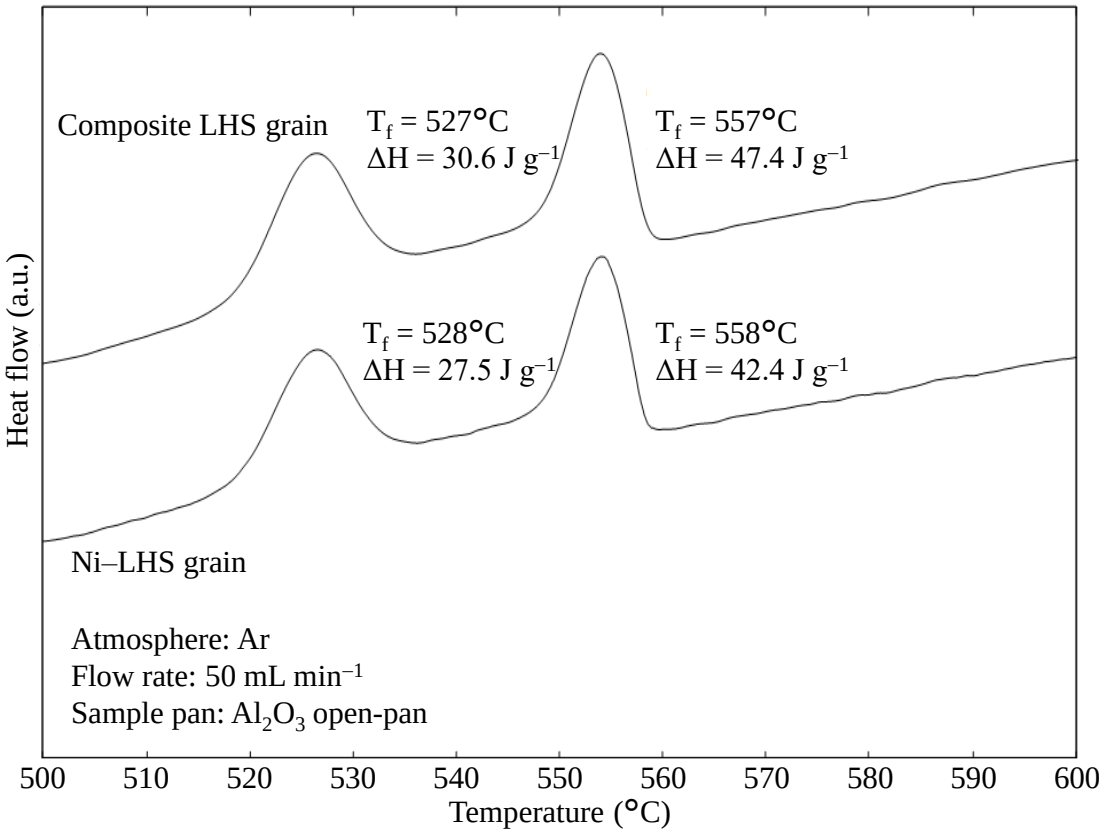

Figure 3-6 DSC curves of composite LHS grain before and after impregnation treatment during heat release under cooling from 600 to 500°C (T_f: freezing point; ΔH: latent heat of fusion).

3.3.2 Steam reforming of ethanol

Figure 3-7 shows the changes in the (a-1) outlet gas concentration, and (a-2) hydrogen yield and packed-bed temperature during the catalyst test using Ni–LHS grains and (b-1) outlet gas concentration, and (b-2) hydrogen yield and packed-bed temperature during the catalyst tests with Ni–Al_2O_3 grains. No C_2H_5OH was detected in the outlet gas, but H_2, CO_2, CO, CH_4, and H_2O were detected. At the beginning of the test, the H_2 concentration was ~62%, CO_2 concentration was ~9%, CO concentration was ~8%, CH_4 concentration was ~3%, and H_2O concentration was ~18%. After 30 min,

the H_2 concentration was ~38%, CO_2 concentration was ~10%, CO concentration was ~0%, CH_4 concentration was ~12%, and H_2O concentration was ~40%.

As shown in Fig. 3-7 (a-2), the H_2 yield also decreased with decreasing temperature. The H_2 yield was 52% and 26% at a catalyst bed temperature of 650°C and 450°C, respectively. During the catalyst test, the temperature dropped steadily, but there was a decrease in the rate of the temperature change at about 550°C. This was due to the release of latent heat from the solidification of the MEPCM. During the catalyst test, the H_2 yield decreased with a similar trend to that of the temperature, but the rate of decrease of the yield reduced around 550°C where the rate of temperature change also decreased slightly. This suggests that the heat released from the MEPCM decreased the temperature change of the catalyst packed bed, which in turn decreased the H_2 yield change rate.

The outlet gas concentration during the catalyst tests with Ni–Al_2O_3 grains showed a similar trend to that of the Ni–LHS grains, as shown in Fig. 3-7 (b-1). The H_2 concentration was slightly lower than that of the case with Ni–LHS grains. As shown in Fig. 3-7 (b-2), both the H_2 yield and the packed-bed temperature continued to decrease steadily during the test with Ni–Al_2O_3 grains. In addition, there was no reduction in the rate of decrease of either temperature or H_2 yield, unlike the case when Ni–LHS grains were used. Therefore, the latter was attributed to the release of latent heat by the MEPCM. In conclusion, the results verified that it is viable to control the heat of a catalytic reaction using an MEPCM as an LHS.

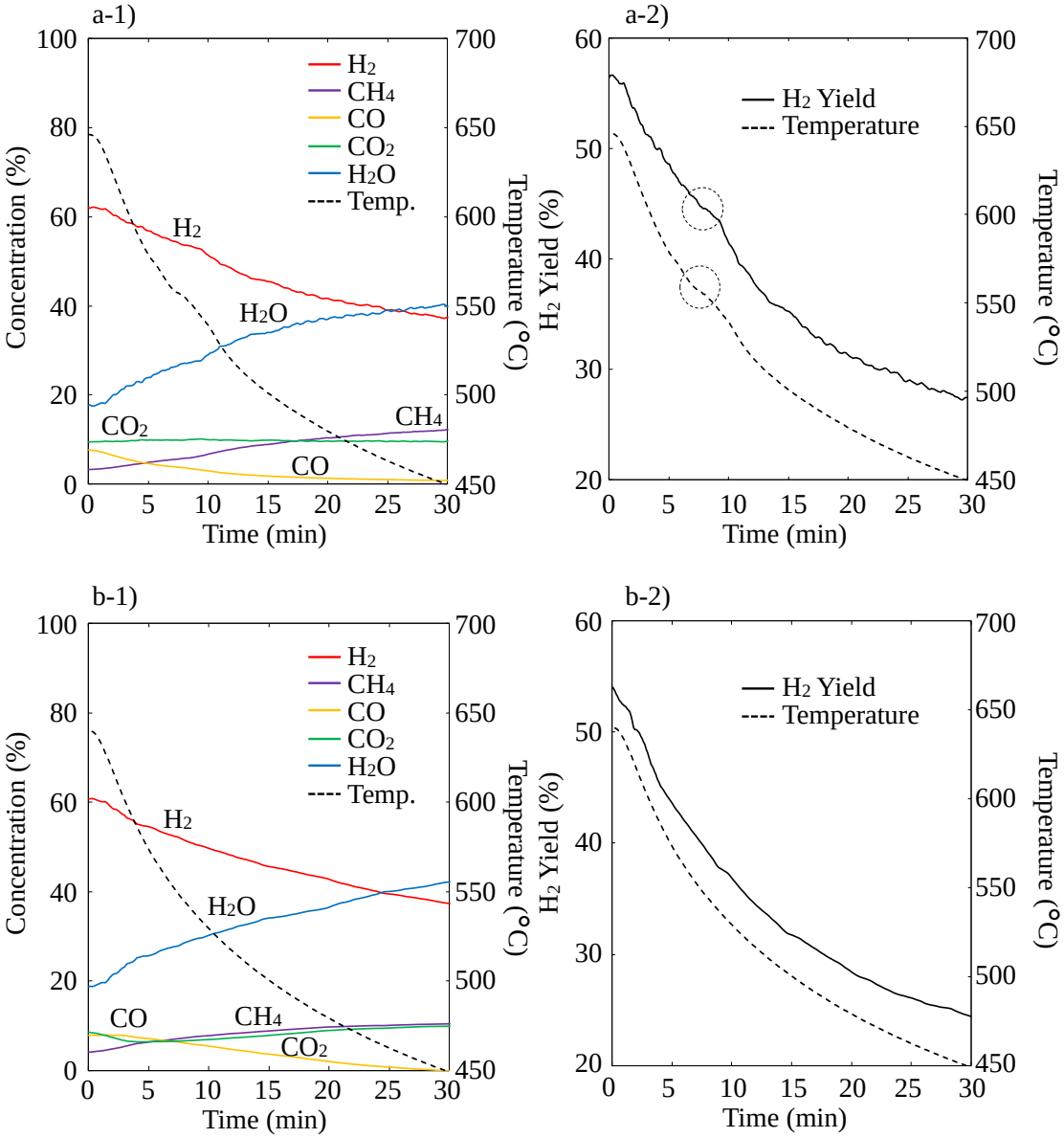

Figure 3-7 a-1), b-1) Concentration of outlet gas, and a-2), b-2) H_2 yield and temperature over time using a catalyst packed bed with a) Ni–LHS or b) Ni-Al_2O_3 during heat release. (Inlet flow: 17 mol% ethanol solution 0.1 ml min^{-1}; carrier gas: Ar 200 ml min^{-1}).

3.3.3 Characterization of the Ni–LHS grains after catalytic tests

Figure 3-8 shows a photograph of the Ni–LHS grains after the catalytic tests. There was no change in the shape and size of the grains after testing (the grain size remained ~1–3 mm). Two particle surface colors were observed: black and gray. Figure

3-9 shows the corresponding SEM images and EDS maps of the Ni–LHS grains after these tests. The surface of the black Ni–LHS grains was covered with fibrous precipitates, which were identified as carbon by EDS mapping. However, no carbon precipitation was observed on the surface of the gray grains. It is possible that all Ni–LHS grains will be covered with carbon after some time, and the catalyst will be deactivated by prolonged use.

Figure 3-10 shows XRD patterns of Ni–LHS grains a) just after hydrogen reduction, and b) after hydrogen reduction and catalytic tests. In both samples, the Al and Si peaks indicating the MEPCM and those of the sintered material were observed, which were also detected for the as-prepared Ni–LHS grains. Therefore, the core Al–Si alloy was protected and chemically unchanged during catalysis. NiO was observed before testing, but after the reduction treatment and catalytic test, it was not observed, and a new peak related to Ni was observed. This was due to the reduction of NiO to Ni in the presence of hydrogen before the catalytic tests.

Figure 3-11 shows the DSC curves of Ni–LHS grains after the catalytic tests. Endothermic peaks due to the solidification of PCM were observed. The L was 70.2 J g^{-1} and the freezing point was 557°C. These values are consistent with those of the Ni–LHS grains before testing. Therefore, the use of Ni–LHS grains in the catalytic test did not degrade their performance as a heat-storage material (at least over the time period observed here).

Figure 3-8 Appearance of Ni–LHS grain after a catalytic test.

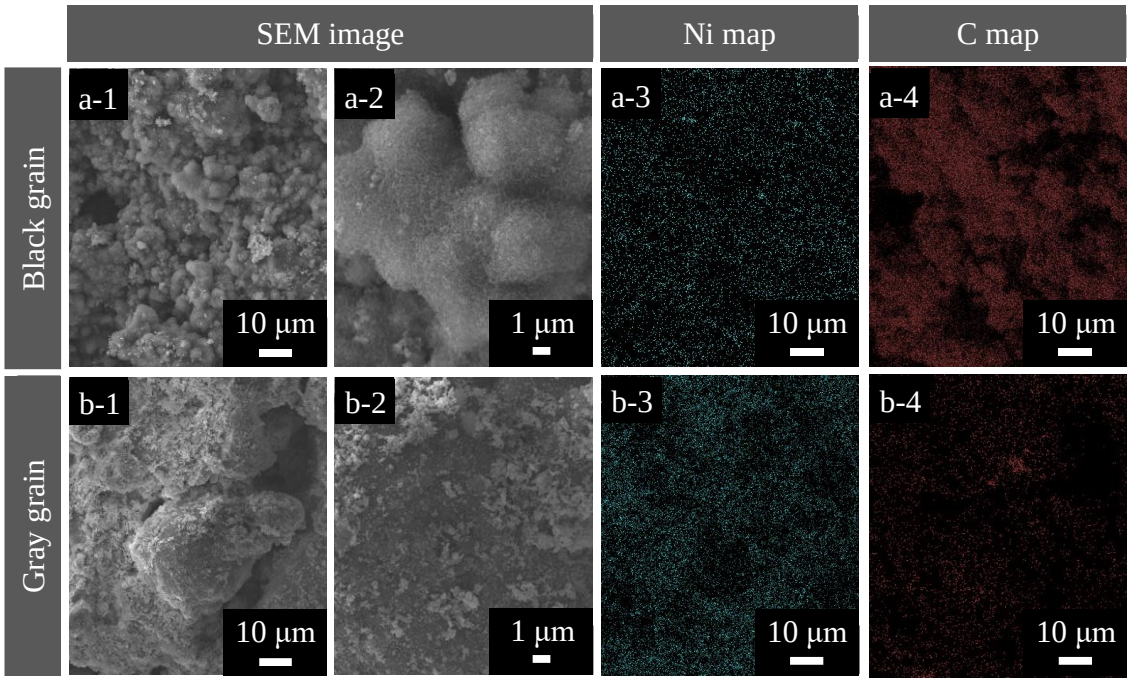

Figure 3-9 SEM images and Ni and C EDS maps of Ni–LHS grains after catalytic testing: a) black grain and b) gray grain (as shown in Fig. 3-8).

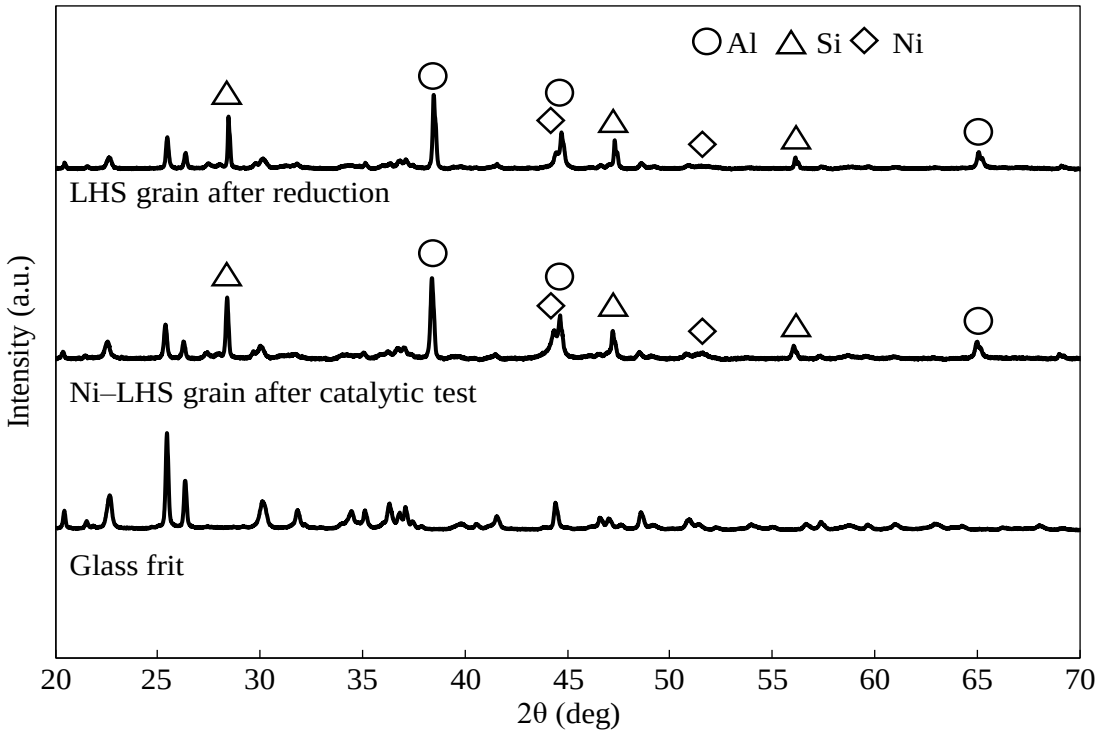

Figure 3-10 XRD patterns of Ni–LHS grains after reduction or catalytic testing, and the glass frit.

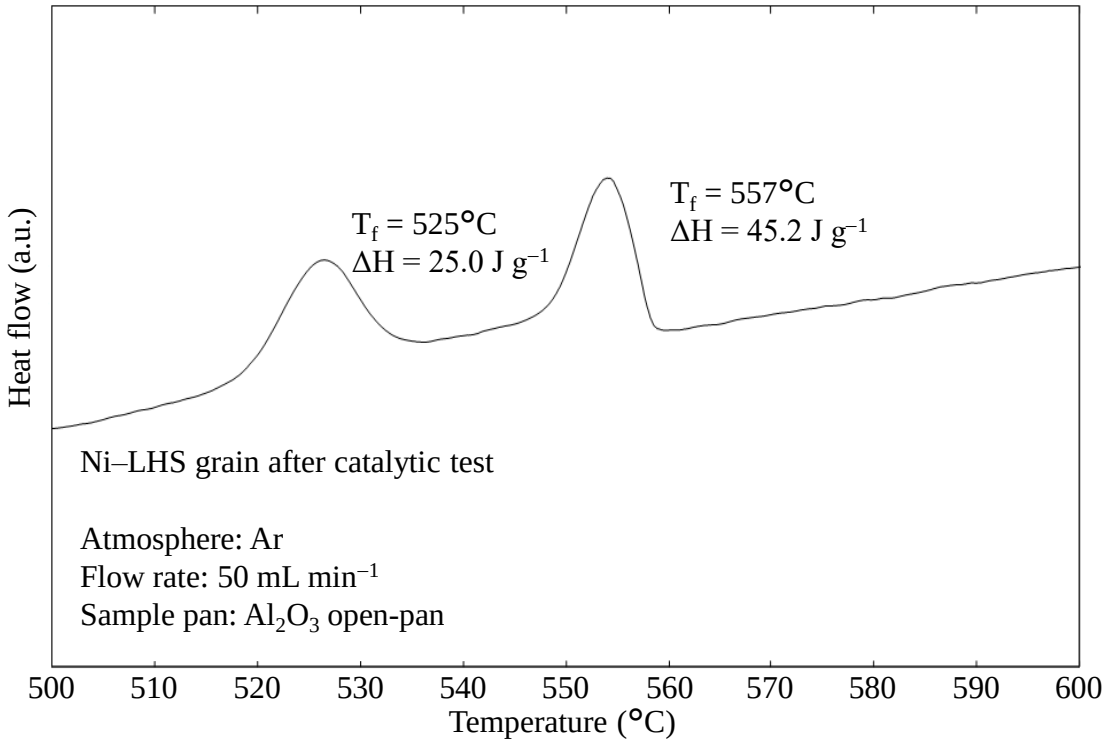

Figure 3-11 DSC curves of Ni–LHS grains after catalytic testing during heat release. (T_f: freezing point; ΔH: latent heat of fusion)

3.4 Discussion

The DSC results showed that the solidification temperatures were 557°C and 558°C for the LHS and Ni–LHS grains, respectively. These values are lower than the melting point of Al–25mass%Si alloy, the raw MEPCM material (577°C). It has been reported that undercooling occurs during the solidification of Al–25mass%Si/α-Al_2O_3 core/shell-structured MEPCM [5]. In addition, Al–Si-alloy-based MEPCM showed two heat-release peaks [6], which is consistent with those observed for each type of heat-storage particle analyzed here (Fig. 3-6).

In the catalytic performance tests, the outlet gas consisted of H_2, CO_2, CO, CH_4, and H_2O. Steam reforming of ethanol is known to have many more side reactions than steam reforming of methane and methanol, because ethanol contains two carbon atoms [7]. The following are some of the major side reactions in ethanol steam reforming, where ΔH_{298K} is the enthalpy change at 298 K.

$C_2H_5OH + H_2O \rightarrow 4H_2 + 2CO$ $\Delta H_{298K} = 256$ kJ mol^{-1} (3)

$C_2H_5OH + 2H_2 \rightarrow 2CH_4 + H_2O$ $\Delta H_{298K} = -157$ kJ mol^{-1} (4)

$C_2H_5OH \rightarrow CO + CH_4 + H_2$ $\Delta H_{298K} = 49$ kJ mol^{-1} (5)

$CO + H_2O \rightarrow CO_2 + H_2$ $\Delta H_{298K} = -41$ kJ mol^{-1} (6)

Because CO and CH_4 were detected in the outlet gas, it is considered that the above side reactions proceeded in addition to the target reaction.

3.5 Conclusion

LHS grains (particle size: 2 mm) were prepared by mixing MEPCM and glass frit as a sintering material, in a mass ratio of 1:1 and forming them by tumbling granulation. Ni was impregnated into the LHS grains to prepare Ni–LHS grains. Steam reforming of ethanol was performed using the Ni–LHS grains as catalyst while lowering the reaction temperature. As a result, 52% H_2 yield was obtained when the temperature

of the catalyst packed bed was 650°C, but this yield decreased to 26% at 450°C. During the catalytic test, there was a reduction in the rate of temperature change due to the heat release of solidification of the MEPCM at ~550°C. This was accompanied by a corresponding reduction in the rate of change of the H_2 yield. This phenomenon was not observed when Ni–Al_2O_3 grains were used as the catalyst. Therefore, the MEPCM as an LHS material is capable of supplying heat to the endothermic reaction system.

References

[1] Maruoka N, Sato K, Yagi J, Akiyama T. Development of PCM for Recovering High Temperature Waste Heat and Utilization for Producing Hydrogen by Reforming Reaction of Methane. ISIJ Int. 2002;42:215-9.

[2] Maruoka N, Akiyama T. Development of PCM reactor for methane steam reforming. ISIJ Int. 2010;50:1305-10.

[3] Maruoka N, Akiyama T. Exergy recovery from steelmaking off-gas by latent heat storage for methanol production. Energy. 2006;31:1632-42.

[4] Sheng N, Zhu C, Saito G, Hiraki T, Haka M, Hasegawa Y, et al. Development of a microencapsulated Al–Si phase change material with high-temperature thermal stability and durability over 3000 cycles. J of Mater Chem A. 2018;6:18143-53.

[5] Nomura T, Yoolerd J, Sheng N, Sakai H, Hasegawa Y, Haga M, et al. Microencapsulation of eutectic and hyper-eutectic Al-Si alloy as phase change materials for high-temperature thermal energy storage. Sol Energy Mater Sol Cells. 2018;187:255-62.

[6] Nomura T, Sheng N, Zhu C, Saito G, Hanzaki D, Hiraki T, et al. Microencapsulated phase change materials with high heat capacity and high cyclic durability for high-temperature thermal energy storage and transportation. Appl Energy. 2017;188:9-18.

[7] Vaidya PD, Rodrigues AE. Insight into steam reforming of ethanol to produce hydrogen for fuel cells. Chem Eng J. 2006;117:39-49.

Chapter 4

Investigation of the unique solidification of alloy phase-change materials as microcapsules

4.1 Introduction

Supercooling is one of the most important material properties of PCMs, especially for heat release, because their heat utilization is achieved by extracting the stored heat. Supercooling phenomena associated with microencapsulation have often been reported for MEPCMs. For example, it has been shown that there is a relationship between a certain particle size and the degree of supercooling in organic PCMs [1-3]. Supercooling is also related to the solidification structure. Depending on the composition of Si, the Al–Si alloys studied in this paper can have eutectic, eutectic, or hyper-eutectic microstructures. In the first half of Chapter 4, the effect of the microstructural evolution on supercooling was investigated, specifically the effect of grain size and Si composition.

One of the interesting phenomena affecting the nucleation of alloyed materials is superheating. Metastable microheterogeneity exists in some liquid alloys [4, 5]. It is considered that the metastable component can act as a nucleation embryo. This metastable state can dissolve at temperatures above the liquidus temperature of the material. Thus, superheating affects solidification, because a temperature increase above the melting temperature can affect supercooling. In the latter half this Chapter, the effect of superheating on solidification phenomena is discussed, because the effect of superheating should be considered in PCM operation.

4.2 Materials and methods

4.2.1 Materials

Spinning-disk-atomized microparticles of Al–Si alloys (Hikari Material Industry Co. Ld., purity: 99.0%, T_m: 577 °C) were used as raw materials. Various Si contents were used to achieve hypoeutectic (Al–5mass%Si), eutectic (Al–12mass%Si), and hypereutectic (Al–25mass%Si) compositions. These particles were classified by nylon sieves with 20, 37, 53, 75, or 106 μm mesh.

4.2.2 Preparation of MEPCMs

MEPCMs were prepared following the method reported in a previous study [6, 7]. First, the Al–Si particles were classified and then a boehmite treatment was conducted in boiling distilled water to form a precursor shell on the surface. After filtration and drying, the MEPCM precursor were obtained, which was then heat treated in an oxygen gas flow (purity: 99.5%) to form a stable Al_2O_3 shell. The Al–5mass%Si and Al–12mass%Si MEPCM precursors were heated from room temperature to 1200°C, while the Al–25mass%Si MEPCM precursor was heated to 1150°C. The heating rate was 10°C min^{-1} and the target temperature was maintained for 3 h to finally obtain the MEPCMs.

4.2.3 Characterization

SEM (JEOL, JSM-7001FA) and EDS were used to characterize the surface structure. The phase composition was determined using powder XRD with a 1D silicon-strip detector (Rigaku Miniflex600, D/teX Ultra2, Cu Kα). Their latent heat of fusion, melting temperature, and freezing temperature were obtained using TG-DSC (Mettler Toledo TGA-DSC-3); the samples were heated to 800°C and cooled at a rate of 5 °C min^{-1} in an Ar atmosphere. The effect of superheating on the freezing of the PCMs, their latent heat of fusion, and the melting and freezing temperatures was also

investigated; the MEPCMs with a 20–37 μm diameter were heated to 650, 800, or 1000°C, kept for 5 min and then cooled at rate of 5 °C min^{-1} in an Ar atmosphere. For comparison, bulk Al–Si alloy was also prepared. Raw Al–Si particles with the same composition were heated to 1000°C and kept for 10 min under an Ar flow in a high-frequency induction furnace to obtain bulk Al–Si alloy. The same measurements were performed to characterize the bulk Al–Si alloys. SEM was used to characterize the cross-sections of the MEPCMs after DSC measurements.

4.3 Results

4.3.1 Effect of Si content and MEPCM diameter on supercooling

4.3.1.1 As-prepared MEPCMs

Figure 4-1 shows SEM images and elemental maps of Al–5mass%Si, Al–12mass%Si, and Al–25mass%Si MEPCMs with various diameters. In the elemental maps, the purple area indicates that Al (red) and O (blue) were both detected. An Al-oxide film was formed on all MEPCMs, regardless of their composition and grain diameter.

Figure 4-2 shows XRD patterns of Al–5mass%Si, Al–12mass%Si, and Al–25mass%Si MEPCMs with various diameters. For all MEPCMs, the major phases were Al, Si, and α-Al_2O_3. The results confirmed that Al–Si alloys were present in the Al_2O_3 layer of the MEPCM capsule.

Figure 4-3 shows the weight change of samples during heat treatment to prepare the MEPCMs. The weight loss of Al hydroxide and mass increase due to Al oxidation were observed. For all compositions, the weight change (ΔW) calculated from the difference between the minimum and maximum weight-change values tended to be greater for smaller particle sizes.

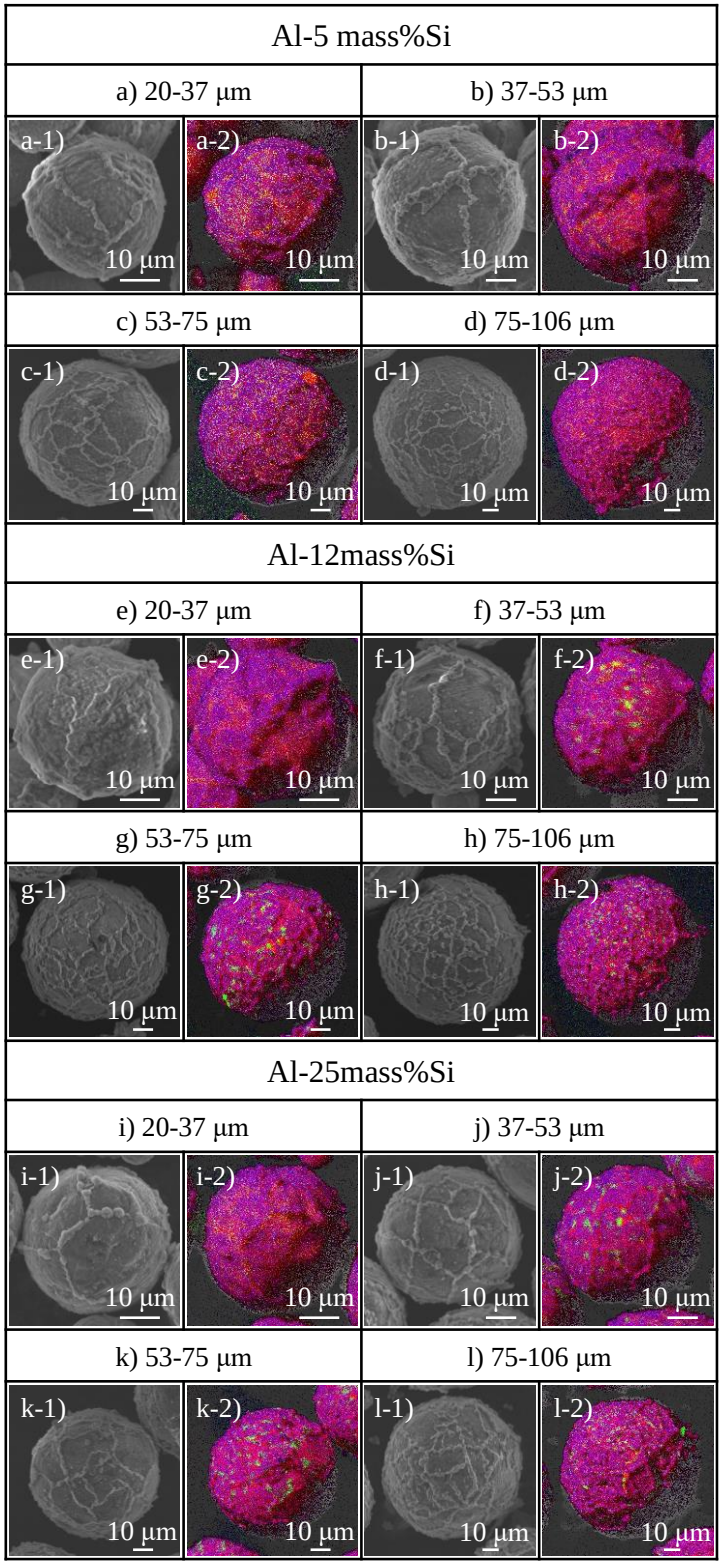

Figure 4-1 1) SEM images and 2) elemental maps of Al-Si MEPCMs with diameter of a, e, i) 20–37, b, f, j) 37–53, c, g, k) 53–75, and d, h, l) 75–106 μm. In the elemental maps, Al, Si, and O are indicated in red, green, and blue, respectively.

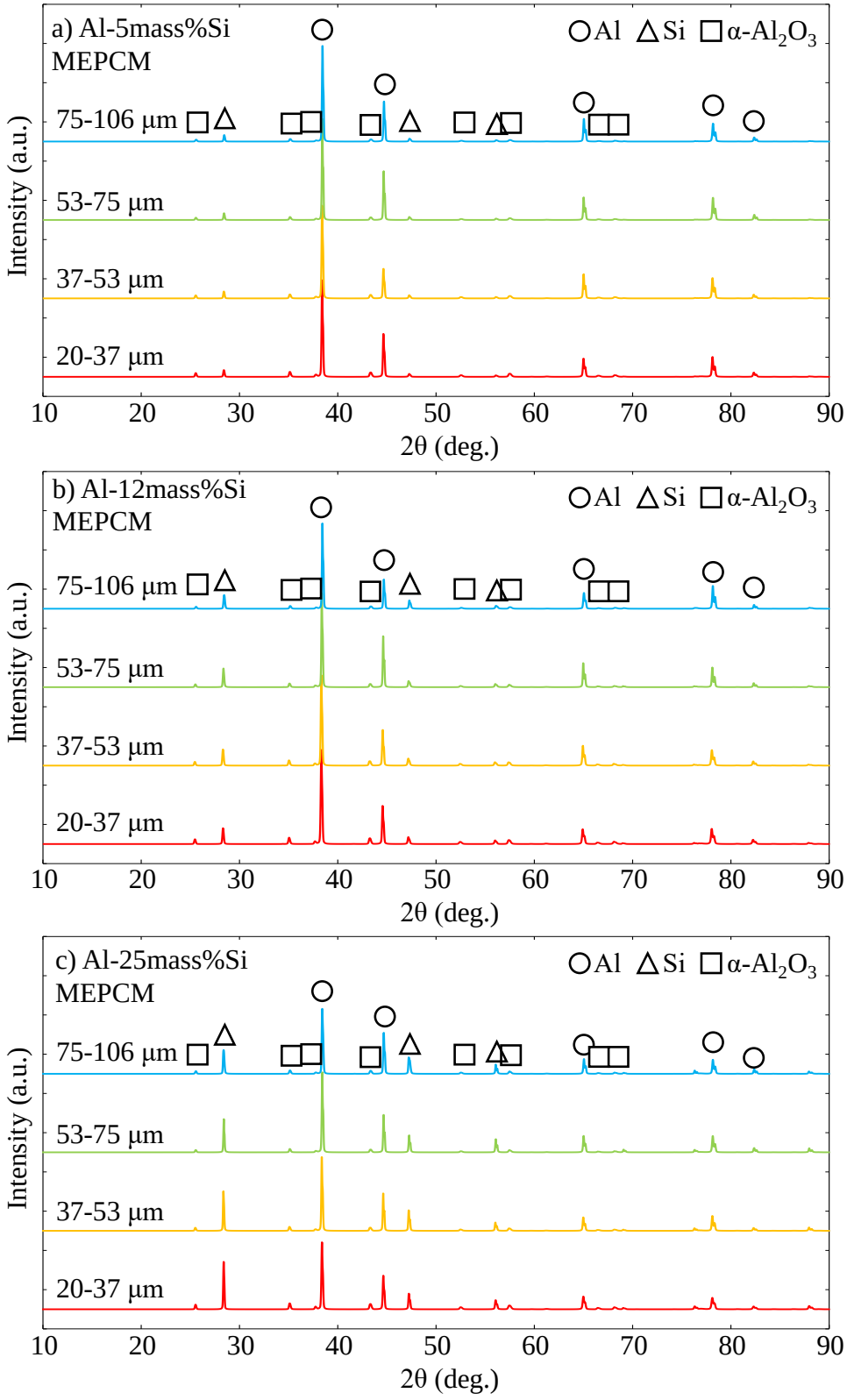

Figure 4-2 XRD patterns of a) Al-5mass%Si , b) Al-12mass%Si, and c) Al-25mass5Si MEPCMs.

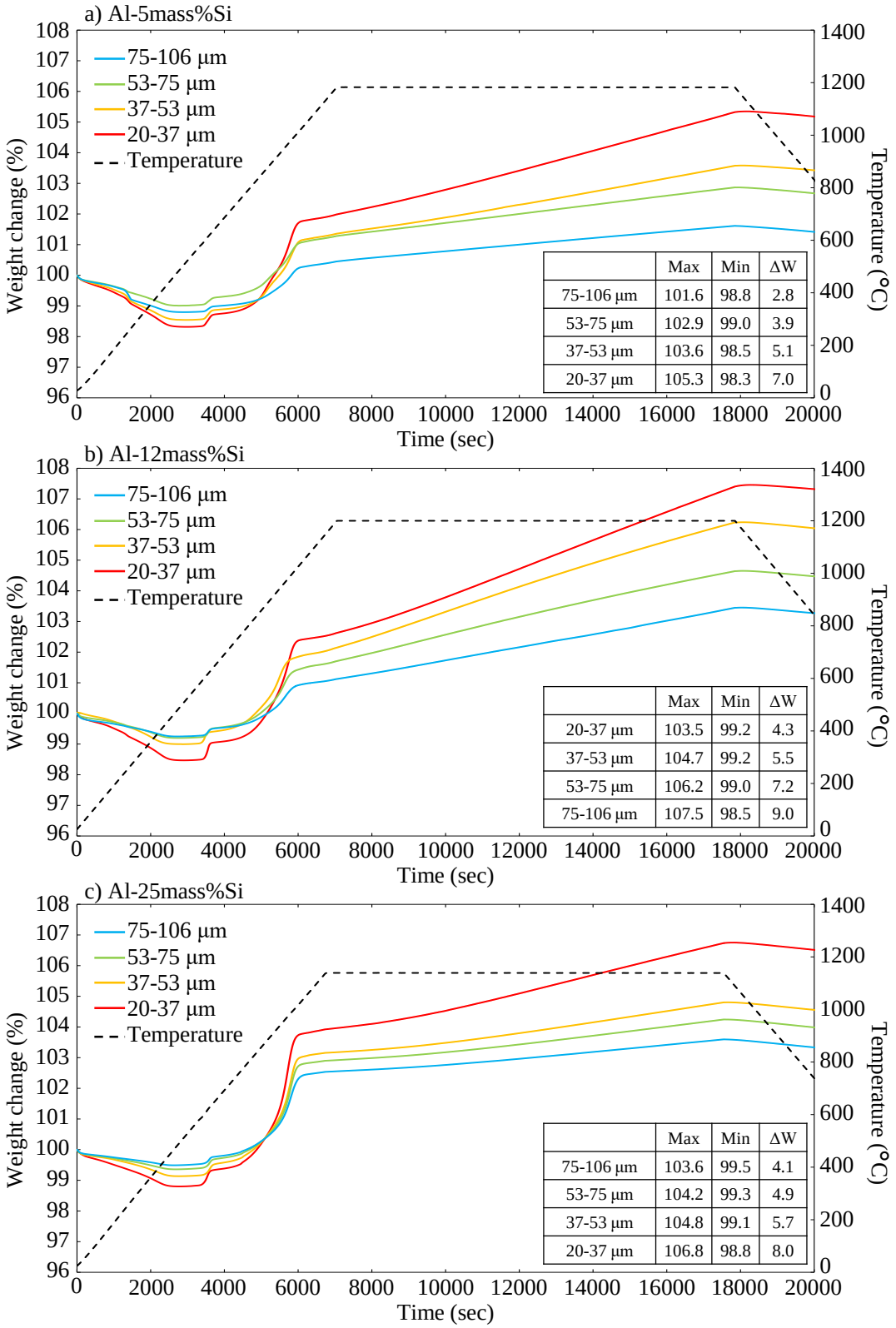

Figure 4-3 Weight change of a) Al-5mass%Si, b) Al-12mass%Si, and c) Al-25mass%Si MEPCMs during heat treatment under O_2 flow at a rate of 200 mL min^{-1}.

4.3.1.2 Thermal properties of MEPCMs

In the subsequent analysis, the MEPCMs described in the previous section were used. Figure 4-4, 4-5, and 4-6 show DSC curves of the prepared MEPCMs. In each figure, convex curves trending downward and upward indicate endothermic and exothermic processes, respectively, i.e., phase change during melting and freezing of the PCM, respectively. Table 4-1 shows the melting and freezing temperatures and latent heat of fusion evaluated from Fig. 4-4, 4-5, and 4-6. The supercooling was calculated as the difference between the temperature of the eutectic (melting) and eutectic (freezing) temperatures.

In Fig. 4-4, two peaks during both heating and cooling were observed. For Al–5mass%Si (hypoeutectic composition), the low-temperature peaks indicate eutectic reactions of Al–Si and the high-temperature peaks indicate the melting and solidification of primary Al. In Table 4-1, “Al (melting)” and “Al (freezing)” refer to primary Al, where only the hypoeutectic composition has primary Al.

Fig. 4-5 shows the DSC results for the Al–25mass%Si MEPCM. The eutectic solidification temperature tended to decrease with decreasing grain size. The supercooling degree increased with decreasing grain size from 75–106 μm to 20–37 μm, from 25.9°C to 34.1°C, respectively.

The same curve as Fig. 4-5 was obtained for Fig. 4-6, which is the measurement result of the hypereutectic MEPCM composition. The eutectic solidification temperature also tended to decrease with decreasing grain size. The supercooling degree increased with decreasing grain diameter from 75–106 μm to 20–37 μm, i.e., from 33.6°C to 36.9°C, respectively.

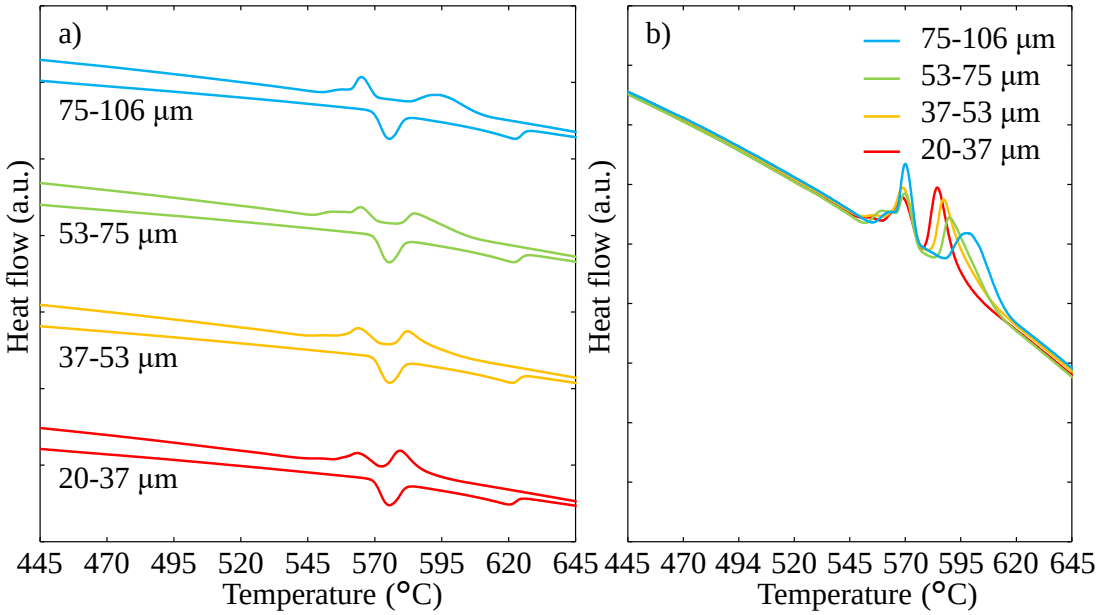

Figure 4-4 DSC curves of Al-5mass% MEPCMs with different grain sizes. a) Curves during heating and cooling. b) Overlapping curves during cooling.

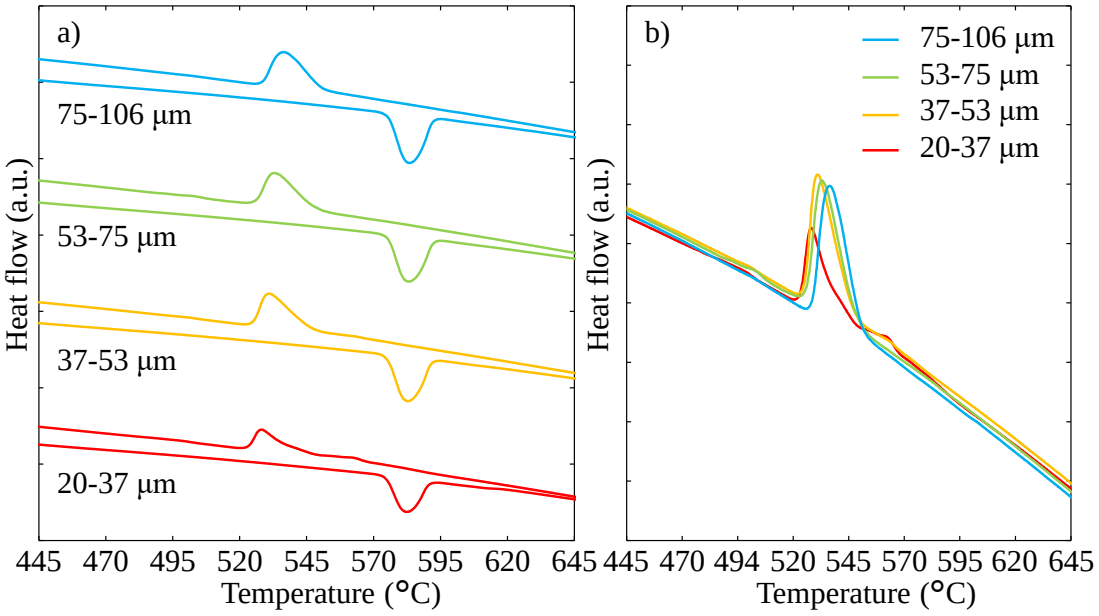

Figure 4-5 DSC curves of Al-12mass% MEPCMs with different grain sizes. a) Curves during heating and cooling. b) Overlapping curves during cooling.

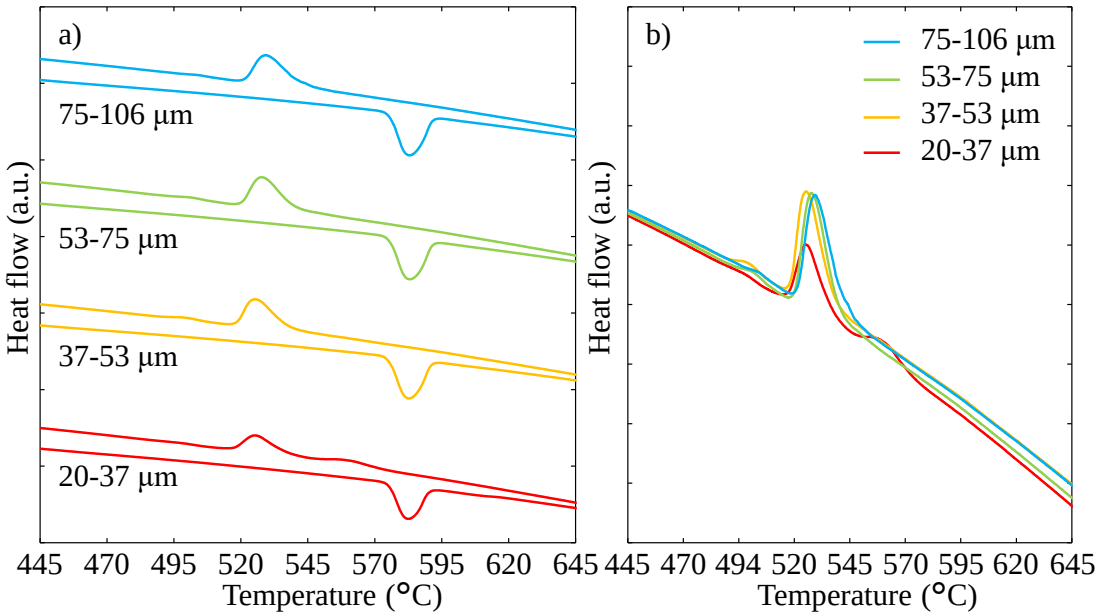

Figure 4-6 DSC curves of Al-25mass% MEPCMs with different grain sizes. a) Curves during heating and cooling. b) Overlapping curves during cooling.

Table 4-1 Melting and freezing temperatures, latent heat of fusion (ΔH), and supercooling evaluated from the DSC curves of the MEPCMs.

Si content		Eutectic (melting)		Al (melting)		Eutectic (freezing)		Al (freezing)		Supercooling
	Diameter [µm]	Temperature [°C]	ΔH [J g^{-1}]	Temperature [°C]	ΔH [J g^{-1}]	Temperature [°C]	ΔH [J g^{-1}]	Temperature [°C]	ΔH [J g^{-1}]	Temperature [°C]
5	raw	574.1	170.7	595.5	175.1	574.4	144.4	623.9	184.7	**-0.3**
5	75-106	574.6	154.5	602.4	162.4	575.5	143.6	613.5	188.3	**-0.8**
5	53-75	574.8	153.4	599.8	155.2	577.0	155.5	597.2	157.7	**-2.2**
5	37-53	574.7	150.9	601.7	143.7	576.3	125.2	597.2	157.7	**-1.6**
5	20-37	574.7	151.3	594.9	137.7	576.6	110.6	596.9	150.5	**-1.9**
12	raw	575.4	506.8	-	-	566.0	489.0	-	-	**9.4**
12	75-106	575.8	407.7	-	-	549.9	378.4	-	-	**25.9**
12	53-75	575.6	390.7	-	-	547.7	370.4	-	-	**27.9**
12	37-53	575.2	376.1	-	-	547.0	348.2	-	-	**28.2**
12	20-37	574.6	278.8	-	-	540.5	201.3	-	-	**34.1**
25	raw	576.2	416.3	-	-	571.4	409.3	-	-	**4.8**
25	75-106	575.5	338.5	-	-	541.9	312.6	-	-	**33.6**
25	53-75	575.5	339.8	-	-	540.5	294.8	-	-	**35.0**
25	37-53	575.3	323.9	-	-	538.7	277.8	-	-	**36.6**
25	20-37	575.4	256.3	-	-	538.5	244.3	-	-	**36.9**

4.3.2 Effect of superheating on supercooling

Figure 4-7, 4-8, and 4-9 show DSC curves of the MEPCMs and bulk alloys with three compositions cooled from 650°C, 800°C, or 1000°C. Table 4-2 shows the melting and freezing temperatures and latent heat of fusion evaluated from the DSC curves of the samples. In Fig. 4-9, only one exothermic peak was observed; however, a second exothermic peak was observed at low temperature during cooling. In Table 4-2, "Eutectic 1 (freezing)" and "Eutectic 2 (freezing)" refer to the peak at high temperature and the peak at low temperature, respectively. For the MEPCMs, the measurement results obtained when the temperature was increased to 800°C represent the temperature and latent heat of fusion while melting. The result for Al–5mass%Si MEPCM is shown in Fig. 4-7 a). By changing the cooling start temperature from 650°C to 800°C, the temperature of primary Al precipitation was lower. It is worth noting that only one exothermic peak was observed when cooling from 1000°C. Fig. 4-7 b) shows the result of bulk samples of the same compositions cooled under the same conditions as those used for the MEPCMs; regardless of the cooling start temperature, the same results were obtained. The same curves observed for the MEPCMs were not obtained.

Fig. 4-8 a) shows DSC curves of Al–12mass%Si MEPCM cooled from 650°C, 800°C, or 1000°C. The supercooling degree increased with increasing cooling start temperature. In particular, cooling from 1000°C significantly increased supercooling, from 22.7°C to 75.3°C. Fig. 4-8 b) also shows the results for bulk Al–12mass%Si, which showed a different curve to that of the corresponding MEPCM.

Fig. 4-9 a) shows the DSC results for the Al–25mass%Si MEPCM. When cooling from 650°C, there was a single exothermic peak, but as the cooling start temperature increased, the peak gradually split. Fig. 4-9 b) shows the DSC curves of bulk Al–25mass%Si. Regardless of the cooling start temperature, a single exothermic

peak was obtained. Compared to the MEPCM, the supercooling was very small.

To observe the microstructure of the MEPCMs after the DSC measurements, SEM observations of the sample cross-sections were performed. Figure 4-10 shows the SEM images, where the outer white region is the alumina shell of the MEPCM, the light gray internal region is Al, and the dark gray part is Si. Eutectic Si crystals were dispersed in granular form. In the case of Al–5mass%Si MEPCM cooled from 650°C or 800°C, primary Al was observed in the center of the grain and Al–Si eutectic precipitated at the edge. The microstructure changed with cooling from 1000°C. The primary Al structure was not observed, while the eutectic structure was observed over the entire area. For eutectic and hypereutectic MEPCM compositions, no differences in the microstructure were observed by changing the cooling temperature. The eutectic structure was observed in the eutectic composition, and eutectic and primary Si were observed in the hypereutectic composition.

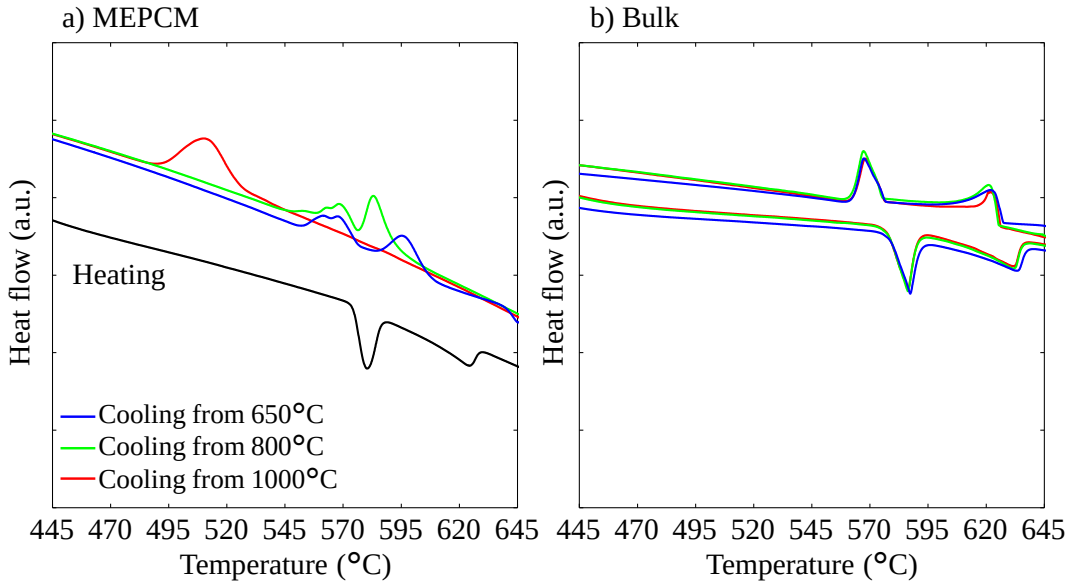

Figure 4-7 DSC curves of Al-5mass%. a) MEPCM and b) bulk material heated to 650 °C, 800 °C, or 1000 °C and cooled at a rate 5 °C min^{-1}.

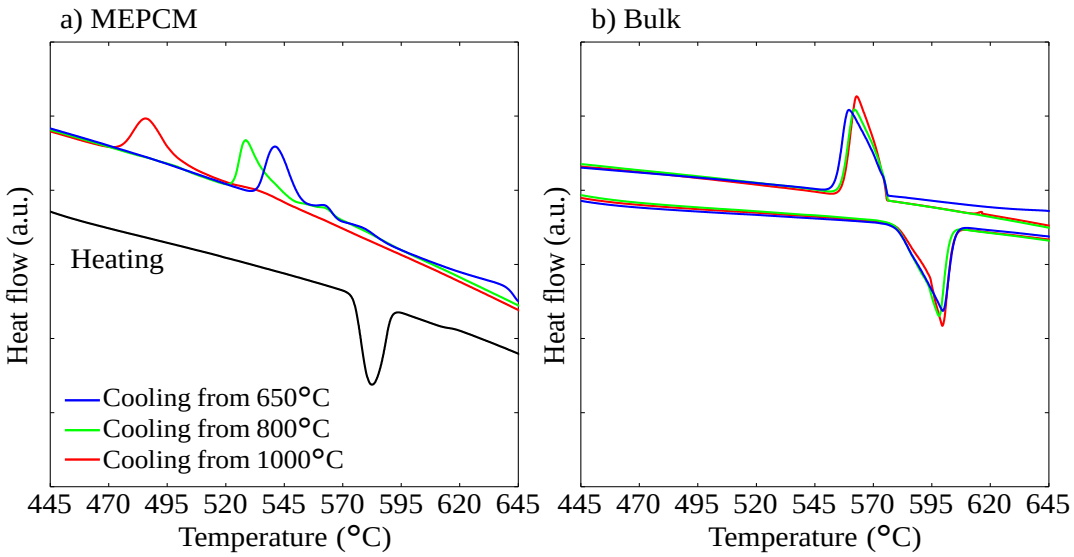

Figure 4-8 DSC curves of Al-12mass%. a) MEPCM and b) bulk material heated to 650 °C, 800 °C, or 1000 °C and cooled at a rate 5 °C min^{-1}.

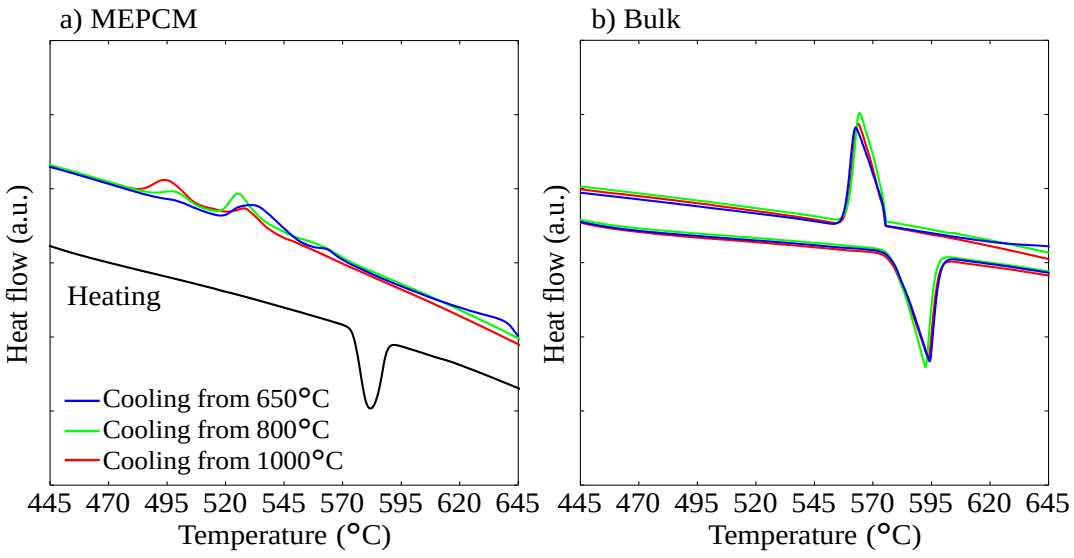

Figure 4-9 DSC curves of Al-25mass%. a) MEPCM and b) bulk material heated to 650 °C, 800 °C, or 1000 °C and cooled at a rate 5 °C min^{-1}.

Table 4-2 Melting and freezing temperatures, latent heat of fusion, and supercooling temperature evaluated from DSC curves of the MEPCMs and bulk PCMs.

Si content	Maximum Temperature [°C]	Style	Eutectic (melting)		Al (melting)		Eutectic1 (freezing)		Eutectic 2 (freezing)		Al		Supercooling
			Temperature [°C]	ΔH [J g^{-1}]	Temperature [°C]	ΔH [J g^{-1}]	Temperature [°C]	ΔH [J g^{-1}]	Temperature [°C]	ΔH [J g^{-1}]	Temperature [°C]	ΔH [J g^{-1}]	Temperature [°C]
5	650	MEPCM					577.2	128.0	-	-	607.1	151.6	-2.8
5	800	MEPCM	574.4	144.7	598.6	132.0	575.5	112.7	-	-	591.8	139.7	-1.1
5	1000	MEPCM					525.7	289.8	-	-	-	-	48.7
5	650	Bulk	579.3	145.1	602.8	183.4	577.4	129.0	-	-	627.3	209.3	1.6
5	800	Bulk	576.0	154.9	603.7	178.4	563.3	128.4	-	-	625.3	268.1	12.7
5	1000	Bulk	576.8	154.9	608.2	172.5	576.6	120.0	-	-	640.6	211.9	0.2
12	650	MEPCM			-	-	552.3	236.1	-	-	-	-	22.7
12	800	MEPCM	575.0	274.0	-	-	538.2	232.2	-	-	-	-	36.8
12	1000	MEPCM			-	-	499.7	195.6	-	-	-	-	75.3
12	650	Bulk	581.4	374.8	-	-	576.1	368.3	-	-	-	-	5.3
12	800	Bulk	587.0	340.6	-	-	576.2	354.4	-	-	-	-	10.8
12	1000	Bulk	590.8	342.9	-	-	575.8	380.5	-	-	-	-	15.0
25	650	MEPCM			-	-	547.7	180.6	-	-	-	-	26.7
25	800	MEPCM	574.4	255.9	-	-	534.8	99.4	508.4	32.5	-	-	39.6
25	1000	MEPCM			-	-	539.2	88.1	506.6	92.9	-	-	35.2
25	650	Bulk	578.6	383.3	-	-	576.0	352.1	-	-	-	-	2.6
25	800	Bulk	578.5	378.5	-	-	576.1	358.0	-	-	-	-	2.4
25	1000	Bulk	579.0	359.9	-	-	575.6	333.7	-	-	-	-	3.4

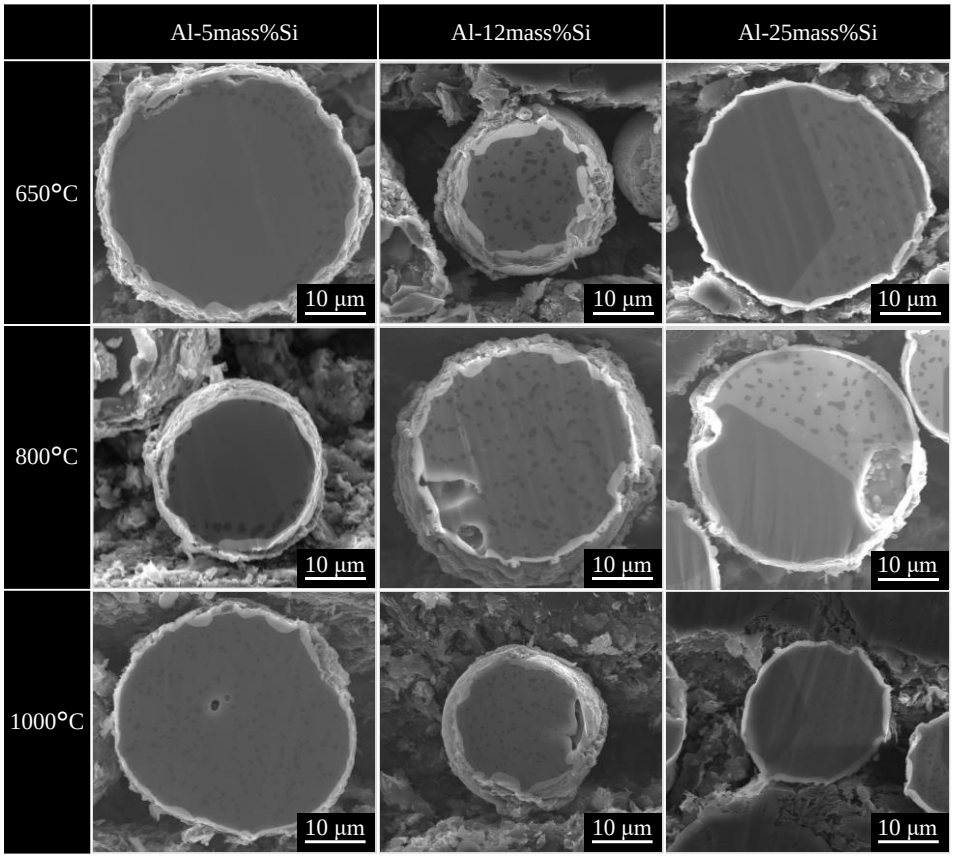

Figure 4-10 SEM images of the cross-sections of three types of MEPCMs: Al-5mass%Si, Al-12mass%Si, and Al-25mass%Si cooled from 650°C, 800°C, or 1000°C.

4.4. Discussion

4.4.1 Effect of Si content and MEPCM diameter on supercooling

In the Al–5mass%Si hypoeutectic MEPCM, the solidification temperature of the Al primary crystal tended to decrease with decreasing grain size. However, eutectic melting and freezing occurred at the same temperature regardless of the grain diameter. This indicates that no supercooling occurred via the eutectic reaction in the Al–5mass%Si MEPCM. According to Nafisi et al., primary Al crystals are nucleation sites for the Al–Si eutectic reaction in the hypoeutectic composition [8]. It is clear from the DSC results of Al–5mass%Si MEPCM that primary Al precipitated in the MEPCM, regardless of its diameter. This is why the undercooling in Al–5mass%Si was significantly suppressed.

Eutectic and hypereutectic MEPCM compositions have a large supercooling effect. The eutectic composition has no primary crystal. In the hypereutectic composition, primary Si exists. Generally, Si crystals are composed of covalent bonds and grow into faceted crystals. Therefore, the primary Si crystal is unlikely to be a nucleation site for new Si crystals. Therefore, the primary Si does not act as a nucleation site, unlike primary Al. Thus, the eutectic and hypereutectic MEPCM compositions showed supercooling. The samples with larger particle size had larger differences in the degree of supercooling in eutectic and hypereutectic MEPCMs, while for smaller particle sizes, there was no significant composition dependence of the supercooling. In particular, the supercooling was similar for grain sizes of 20–37 μm.

The results indicate that the Al primary crystal acts as an effective nucleation site for the eutectic reaction in the MEPCM. The hypoeutectic composition is preferable from the viewpoint of reducing undercooling. A larger amount of latent heat is available for compositions closer to the eutectic composition. To design microcapsules with high

latent-heat energy and minimal supercooling, a hypoeutectic composition close to the eutectic composition is preferable. It is important to note that in the hypoeutectic MEPCM composition, undercooling of primary Al occurs. As the composition approaches that of the eutectic, the amount of Al primary in the capsule decreases and the liquidus temperature also decreases. Accordingly, primary Al may not precipitate before the eutectic reaction temperature due to the undercooling of the primary Al. In this case, it is difficult to induce the eutectic reaction using the Al primary crystals as nucleation sites. The balance between the amount of latent heat and the composition where Al primary crystals can precipitate is important.

4.4.2 Effect of superheating on supercooling

In all compositions, the degree of supercooling increased with increasing cooling start temperature. When the start temperature was changed from 650°C to 800°C, the lowering of the freezing temperature was small: 15.3°C for Al–5mass%Si MEPCM (Al primary, 607.1→591.8°C), 14.1°C for Al–12mass%Si MEPCM (Al-Si eutectic, 552.3→538.2°C), and 12.9°C for Al–25mass%Si MEPCM (Al-Si eutectic, 547.7→534.8°C). In contrast, a significant change was observed for a cooling start temperature of 1000°C. In addition, primary Al was not observed in MEPCM cooled from 1000°C. These results suggest that Al primary crystallization did not occur in the Al–5masss%Si MEPCM cooled from 1000°C, and only the eutectic reaction occurred with a large degree of supercooling. This structure is considered to be a pseudo-eutectic structure.

Studies of the existence of heterogeneous components in Al–Si alloy heated above the melting point may facilitate the understanding of the temperature-dependent supercooling. Investigations of heterogeneous components in Al–Si binary liquid were carried out by high temperature XRD [9] and small-angle neutron scattering [10-12]. It

is thought that there are Si clusters, as heterogeneous components, of a few tens to hundreds of nanometers in the solution. The prevalence of these clusters decreases around 1000°C. Most of the Si clusters can act as nucleation sites. The effect of overheating has also been studied to investigate the relationship between the overheating and supercooling of Al in Al–Al_2O_3 nanocapsules [13]. Even in pure Al, heating to 1000°C significantly accelerated supercooling. Thus, it is expected that the nucleation sites for the solidification reaction for both Al and Si disappear by heating to 1000°C. A high supercooling temperature was observed in the MEPCMs analyzed here that were cooled from 1000°C. In contrast, no supercooling was observed under the same thermal analysis for the bulk material. Therefore, the MEPCM structure is expected to greatly accelerate the effects of overheating.

Generally, dendrites of Al primary crystal or coarse Si primary crystals are precipitated in hypoeutectic or hypereutectic compositions. In Fig. 4-10, such structures were not observed because the inside of the microcapsule is too small to have such a structure. The eutectic microstructure was similar in both compositions. The microstructure changed only when the Al–5mass%Si MEPCM was cooled from 1000°C. Generally, such microstructural changes are achieved by cooling at a high rate (several hundred °C s^{-1} or more) to intentionally increase the degree of supercooling. In this study, despite the low cooling rate of 5 °C min^{-1}, strong overheating and microencapsulation caused large supercooling and microstructural changes. For Al–Si alloys, the microstructure can become eutectic at the composition where primary crystals should be found. This is known as a coupled zone. Because the composition of Al–5mass%Si is outside the coupled zone composition [14], such a pseudo-eutectic microstructure is not expected. This can be characterized as a truly unique form of solidification in MEPCMs.

4.5 Conclusion

In this chapter, the effect of grain size and composition on supercooling, and the effect of superheating on supercooling were investigated for the Al–Si binary alloy system as an MEPCM. The main conclusions are as follows.

1. The supercooling of the Al primary crystal in the hypoeutectic composition and that of the eutectic reaction in the eutectic and hypereutectic compositions increased with decreasing grain size.

2. Supercooling of the eutectic reaction was almost absent in the hypoeutectic composition of the MEPCM, because the Al primary crystals can act as nucleation sites for the Al–Si eutectic reaction.

3. For the eutectic composition, supercooling of about 25–35°C was observed. For the hypereutectic composition, supercooling of more than 30°C was observed.

4. Superheating promoted the degree of supercooling in all compositions.

5. In particular, in the hypoeutectic composition, the precipitation of the Al primary crystal was not observed after cooling from 1000°C, and there was only one exothermic peak.

In the development of MEPCM applications, it is very important to investigate the heat-release characteristics of the material. In this study, the heat-release characteristics of Al–Si-based MEPCMs were investigated for three compositions, with different microstructures within the size range that can be used as microcapsules. To reduce the degree of supercooling, the composition with Al primary crystal precipitation is advantageous. However, the undercooling increases significantly with heating to ~1000°C. In the case of the hypoeutectic composition, the Al primary crystal does not precipitate and significant undercooling occurs.

These results show the influence of composition, grain size, and degree of

heating (i.e., operating temperature of the MEPCM) on the degree of supercooling. It is hoped that these results will serve as an indicator for the selection of raw materials in the development of applications of MEPCM.

References

[1] Al-Shannaq R, Kurdi J, Al-Muhtaseb S, Dickinson M, Farid M. Supercooling elimination of phase change materials (PCMs) microcapsules. Energy. 2015;87:654-62.

[2] Wu Q, Zhao D, Jiao X, Zhang Y, Shea KJ, Lu X, et al. Preparation, properties, and supercooling prevention of phase change material n-octadecane microcapsules with peppermint fragrance scent. Ind Eng Chem Res. 2015;54:8130-6.

[3] Yuan H, Bai H, Lu X, Zhang X, Zhang J, Zhang Z, et al. Size controlled lauric acid/silicon dioxide nanocapsules for thermal energy storage. Sol Energy Mater Sol Cells. 2019;191:243-57.

[4] Popel P, Calvo-Dahlborg M, Dahlborg U. Metastable microheterogeneity of melts in eutectic and monotectic systems and its influence on the properties of the solidified alloy. J Non-Cryst Solids. 2007;353:3243-53.

[5] Popel P, Dahlborg U, Calvo-Dahlborg M. On the existence of metastable microheterogeneities in metallic melts. IOP Conf Ser: Mater Sci Eng: IOP Publishing; 2017. p. 012012.

[6] Nomura T, Zhu C, Sheng N, Saito G, Akiyama T. Microencapsulation of metal-based phase change material for high-temperature thermal energy storage. Sci Rep. 2015;5:9117.

[7] Nomura T, Sheng N, Zhu C, Saito G, Hanzaki D, Hiraki T, et al. Microencapsulated phase change materials with high heat capacity and high cyclic durability for high-temperature thermal energy storage and transportation. Appl Energy. 2017;188:9-18.

[8] Nafisi S, Ghomashchi R, Vali H. Eutectic nucleation in hypoeutectic Al-Si alloys. Mater Charact. 2008;59:1466-73.

[9] Bian X, Wang W. Thermal-rate treatment and structure transformation of Al–13 wt.% Si alloy melt. Mater Lett. 2000;44:54-8.

[10] Calvo-Dahlborg M, Popel P, Kramer M, Besser M, Morris J, Dahlborg U. Superheat-dependent microstructure of molten Al–Si alloys of different compositions studied by small angle neutron scattering. J Alloys Compd. 2013;550:9-22.

[11] Dahlborg U, Kramer MJ, Besser M, Morris JR, Calvo-Dahlborg M. Structure of molten Al and eutectic Al–Si alloy studied by neutron diffraction. J Non-Cryst Solids. 2013;361:63-9.

[12] Dong X, Li P, Amirkhanlou S, Ji S, Popel PS, Dahlborg U, et al. Evidence of disruption of Si-rich microstructure in engineering-lightweight Al–12.2 at.% Si alloy melt above liquidus temperature. Sci Rep. 2020;10:1-11.

[13] Mei Q, Li J. Dependence of liquid supercooling on liquid overheating levels of Al small particles. Materials. 2016;9:7.

[14] Trivedi R, Jin F, Anderson I. Dynamical evolution of microstructure in finely atomized droplets of Al-Si alloys. Acta Mater. 2003;51:289-300.

Chapter 5

Suppression of supercooling of alloy-type MEPCM by doping

5.1 Introduction

Supercooling is observed in alloy-type MEPCMs. In chapter 4, unique supercooling of Al–Si alloy MEPCMs was reported. Considering an application involving constant temperature control by a PCM, supercooling is a fatal problem that excludes the possibility of developing an MEPCM. Indeed, supercooling of the PCM is a major problem for both alloys and other materials. Thus, several studies have addressed supercooling. For example, Safari et al. reviewed supercooling of paraffin, fatty acid, and salt-type PCMs [1]. Zahir et al. also reviewed supercooling of PCM and its mitigation techniques and they suggested studying alloy-type PCMs [2]. The addition of a nucleation agent can effectively suppress supercooling. For paraffin or n-octadecane MEPCMs, the modification of the shell has been reported [3-5]. In this study, Al–Si alloy PCM is the focus, but supercooling of Al–Si microcapsules have rarely been reported. In the field of alloy casting, it was reported that Al intermetallic compounds such as $TiAl_3$, $ZrAl_3$, VAl_{10}, $NiAl_3$, $CrAl_7$, and B_2Al are good nucleation agents for Al [6]. These compounds are candidates for suppressing the supercooling of Al. To produce MEPCMs, it is important to evaluate how nucleation agents can be introduced.

In this chapter, the use of high-speed impact blending (HIB) is described as a proposed method for introducing a nucleation agent into MEPCM. HIB is a dry surface-modification method for particles using a hybridizer. By feeding a powder mixture

containing two types of particles, large ones and small ones, into the high-speed airflow generated in the hybridizer, the powders are subjected to repeated mechanical impacts. This results in the small particles adhering to the surface of the large ones. Fixation of MgSi to silica gel [7], fabrication of TiB_2–Al_2O_3 core–shell particles [8], and surface modification of polyimide by silica [9] were evaluated using this method. Various organic, inorganic, metallic, and ceramic materials are suitable for HIB because it is a simple dry mechanical treatment. Moreover, several minutes of operation time is sufficient and productivity is high.

In this chapter, TiO_2 was used as a nucleation agent (Ti source) for Al–25mass%Si PCM and was introduced using HIB. Then, the suppression of supercooling of the MEPCM by this nucleation agent was investigated.

5.2 Experimental procedures

5.2.1 Materials

Microparticles of spinning-disk atomized Al-25mass%Si (Hikari Material Industry Co. Ld., purity: 99.0%, T_m: 577 °C) were used as raw materials. These particles were classified by nylon sieves with 20 and 37 μm mesh. Sub-micron particles of TiO_2 with a diameter of 0.5 μm (Kojundo Chemical Laboratory Co., Ltd, Purity: 99.99%) were used as the nucleation agent.

5.2.2 High-speed impact blending

Figure 5-1 shows a schematic diagram of the experimental HIB procedure and the hybridizer used for high-speed impact blending. The main parts of the hybridizer are the rotor, blade, and loop circuit for circulation. The powder mixture fed to the hybridizer is dispersed and subjected to a mechanical force under the gas flow by the high-speed rotor and blade. The processed powder passes through a loop circuit and back to the high-

speed gas flow, resulting in the powder being repeatedly impacted to achieve high-speed impact blending.

In this study, 20 g of a mixture of Al–25mass%Si and TiO_2 particles were prepared with TiO_2 contents of 1, 3 or 5 mass%. This mixture was fed to an HIB system (Nara Machinery Co. Ltd., Model NHS-0). TiO_2 was fixed on the Al–Si particles at a circumferential speed of 80 ms^{-1} for 3 min in the hybridizer under Ar flow.

5.2.3 Preparation of MEPCM

MEPCM was prepared using the TiO_2-loaded Al–Si particles with a method reported in a previous study [10, 11]. First, a boehmite (AlOOH) treatment of the Al–Si particles was conducted in boiling distilled water to form a precursor shell on the surface. After filtration and drying, the MEPCM precursor was obtained, and then heat-treated in an oxygen gas flow (purity: 99.5%) to form a stable Al_2O_3 shell. Then, the precursor was heated from room temperature to 1000°C with a heating rate of 10°C min^{-1} and maintained at 1000°C for 3 h to form the final MEPCM.

5.2.4 Characterization

SEM (JEOL, JSM-7001FA) and EDS were used to characterize the surface structure of the MEPCM. The phase composition was determined using powder XRD with a 1D Si-strip detector (Rigaku Miniflex600, D/teX Ultra2, Cu Kα). Their latent heat of fusion melting and freezing temperatures were measured using TG-DSC (Mettler Toledo TGA-DSC-3); the samples were heated to 800°C and cooled at rate of 5 °C min^{-1} in an Ar atmosphere.

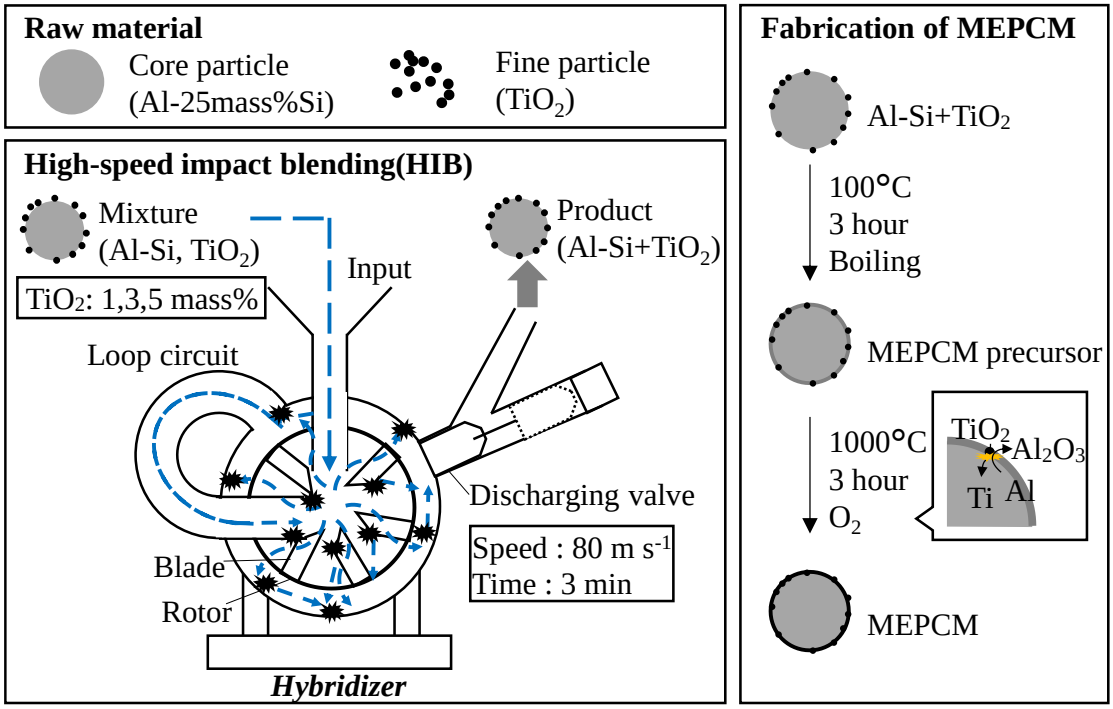

Figure 5-1 Experimental procedure. Schematic image of hybridizer for high-speed impact blending (HIB) is at left side.

5.3 Results

Figure 5-2 shows SEM images of the samples with 1, 3, and 5 mass% of TiO_2 before treatment, and after HIB, chemical reaction with AlOOH, and heat treatment. The upper images show one microsphere and the lower images are magnified views of the surface of the microsphere. Fixed TiO_2 particles were observed on the surfaces under all conditions after HIB. After chemical treatment, the microsphere surfaces were covered with flower-like structures. Then, the surface structure became rough after heat treatment. After TiO_2 introduction by HIB, the microsphere maintained its spherical shape.

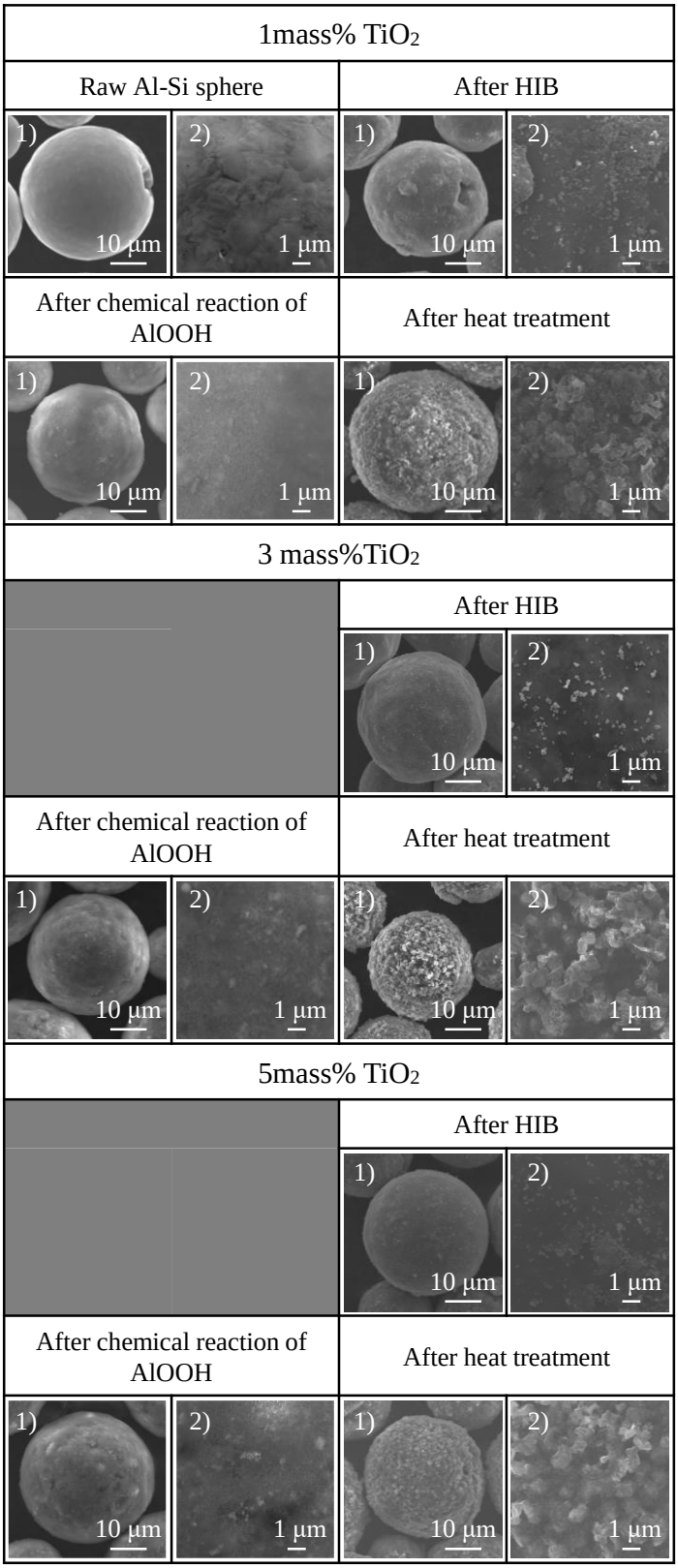

Figure 5-2 1) Overall and 2) magnified SEM images of samples with 1, 3, and 5 mass% TiO_2 before and after HIB, chemical, and heat treatments.

Figure 5-3, 5-4, and 5-5 show SEM images and EDS maps of sample cross-sections of the 1, 3 and 5mass% TiO_2 samples, respectively, after heat treatment. In the SEM images, the white area is the surface oxide layer and the gray area is the internal alloy region. This oxide layer acts as the shell of the microcapsules. Ti was detected inside the oxide layer. The area over which Ti was detected was clearly larger than that over which the raw TiO_2 sub-micron powder was deposited, and Si was also detected in the same area. Figure 5-8 shows SEM–EDS images and the results of EDS line analysis of another MEPCM made from a mixture including 5 mass% TiO_2. Ti was detected in the outer oxides layer of the MEPCM in Fig. 5-6.

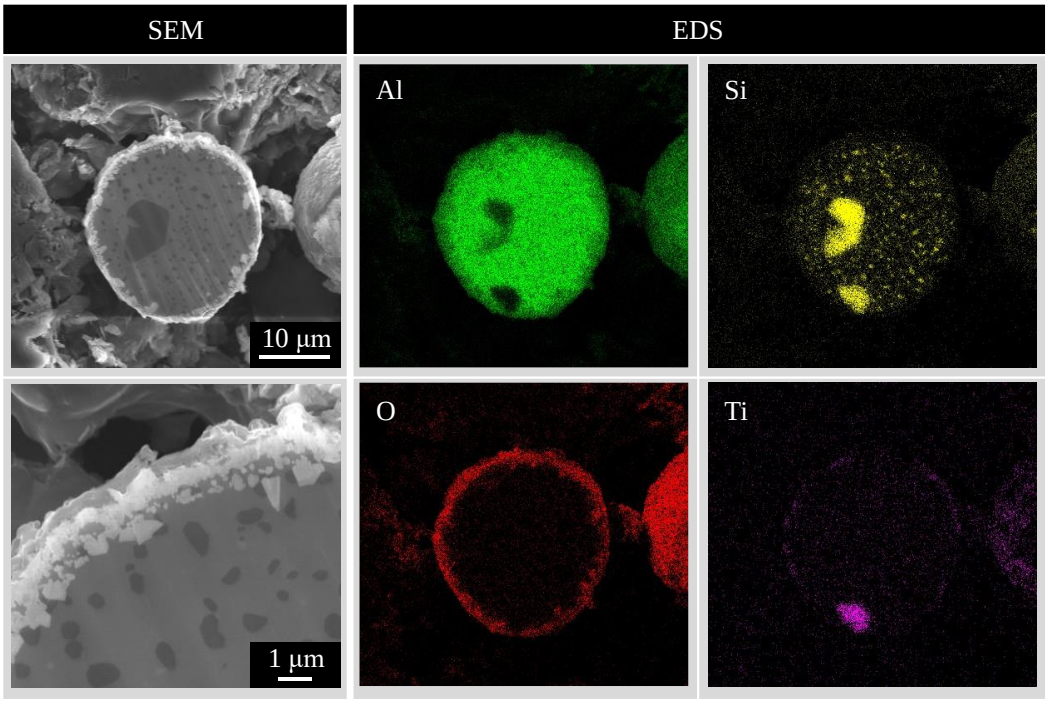

Figure 5-3 Cross-sectional SEM images and EDS maps of MEPCM with 1 mass% TiO_2. Green, yellow, red, and purple regions represent Al, Si, O, and Ti, respectively.

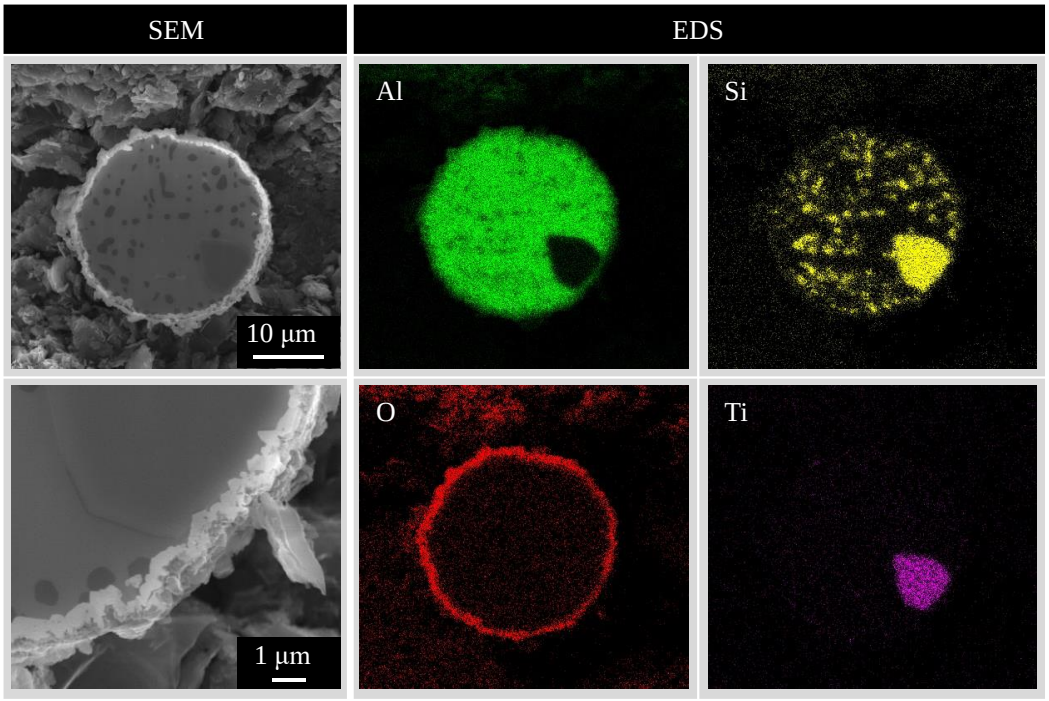

Figure 5-4 Cross-sectional SEM images and EDS maps of MEPCM with 3 mass% TiO_2. Green, yellow, red, and purple regions represent Al, Si, O, and Ti, respectively.

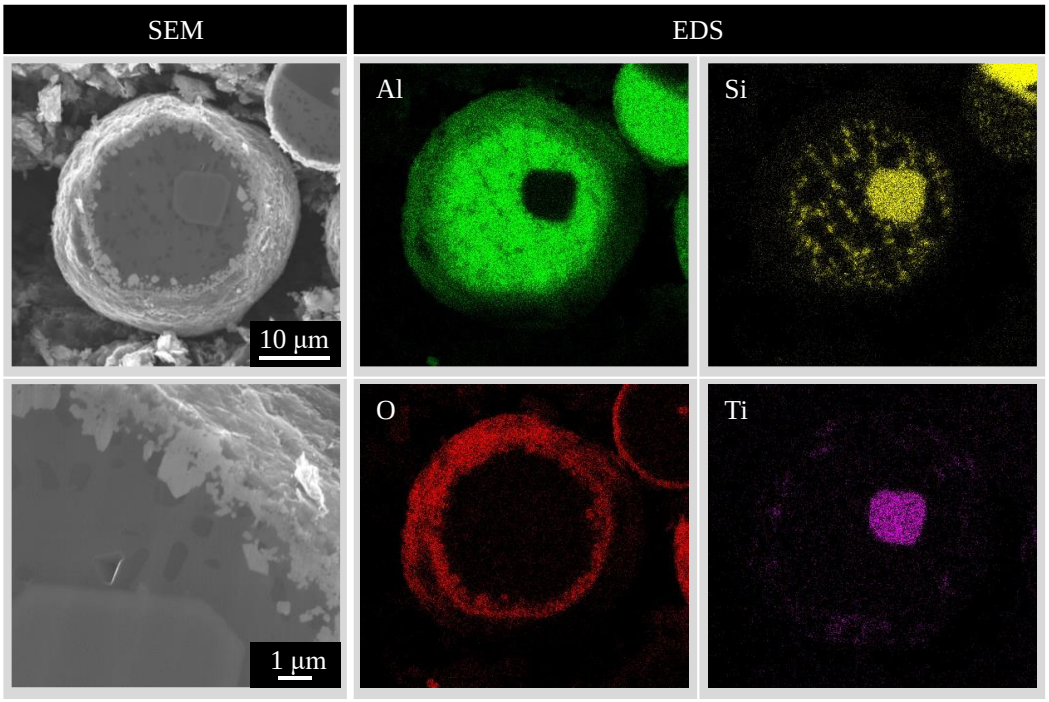

Figure 5-5 Cross-sectional SEM images and EDS maps of MEPCM with 5 mass% TiO_2. Green, yellow, red, and purple region represent Al, Si, O, and Ti, respectively.

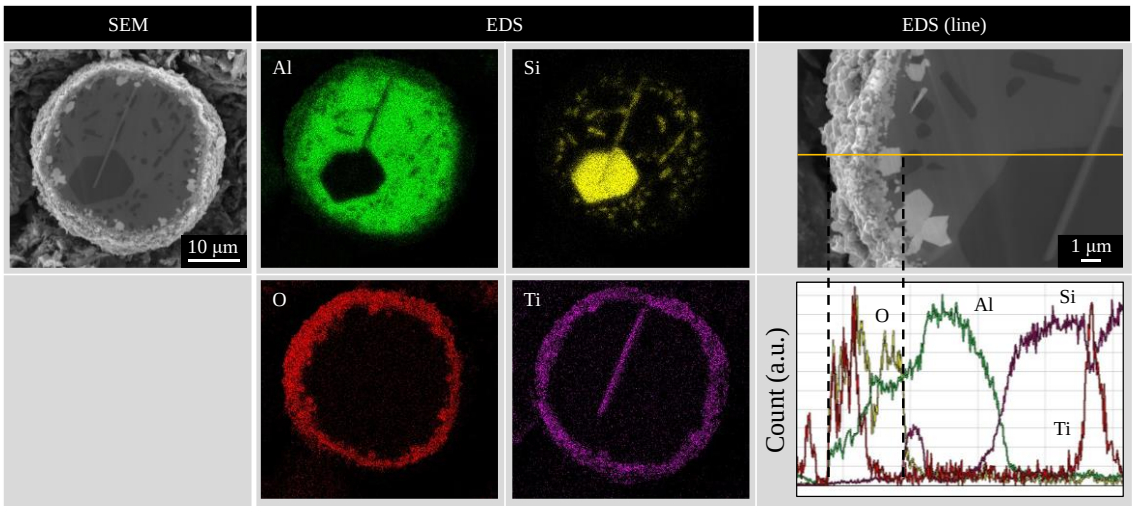

Figure 5-6 Cross-sectional SEM images, and EDS maps and line analysis of MEPCM with 5 mass% TiO_2. Green, yellow, red, and purple regions represent Al, Si, O, and Ti respectively.

Figure 5-7 shows XRD patterns of samples with 1 mass% TiO_2 (as a representative sample) before treatment, and after HIB, chemical reaction with AlOOH, and heat treatment. The major composition of the sample did not change after chemical treatment, and the resulting MEPCM contained Al, Si, and α-Al_2O_3. Figure 5-8 compares the XRD patterns of the MEPCMs with the different TiO_2 contents, and the smaller peaks were analyzed. Tiny peaks of $TiSi_2$ were detected. In addition, TiO_2 peaks were detected for the MEPCMs prepared with the higher TiO_2 contents (3 or 5 mass%).

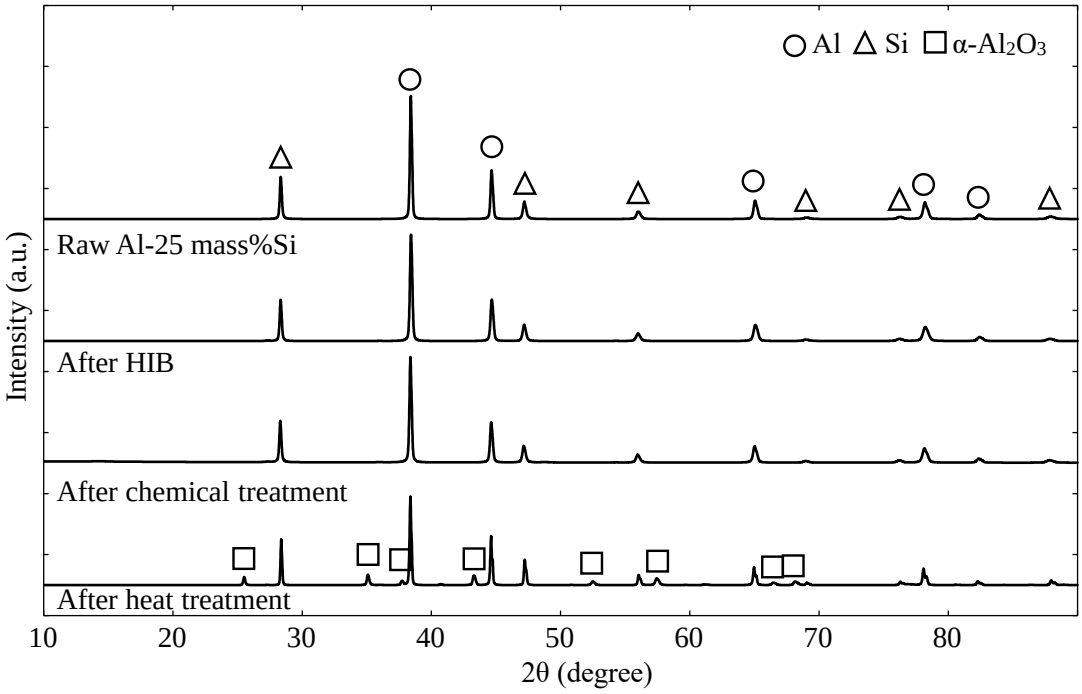

Figure 5-7 XRD patterns of samples with 1 mass% TiO_2 before and after HIB, chemical, and heat treatments.

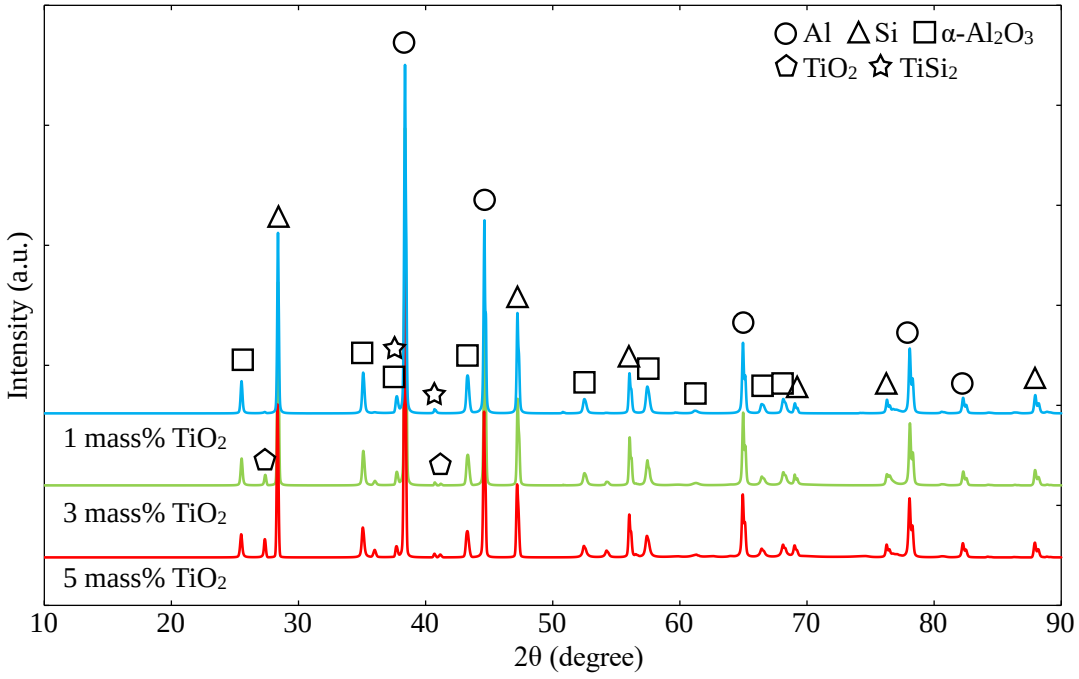

Figure 5-8 XRD patterns of MEPCMs with 1, 3 and 5 mass% TiO_2. The pattern is magnified compared to Fig. 5-7 to clearly show the tiny peaks.

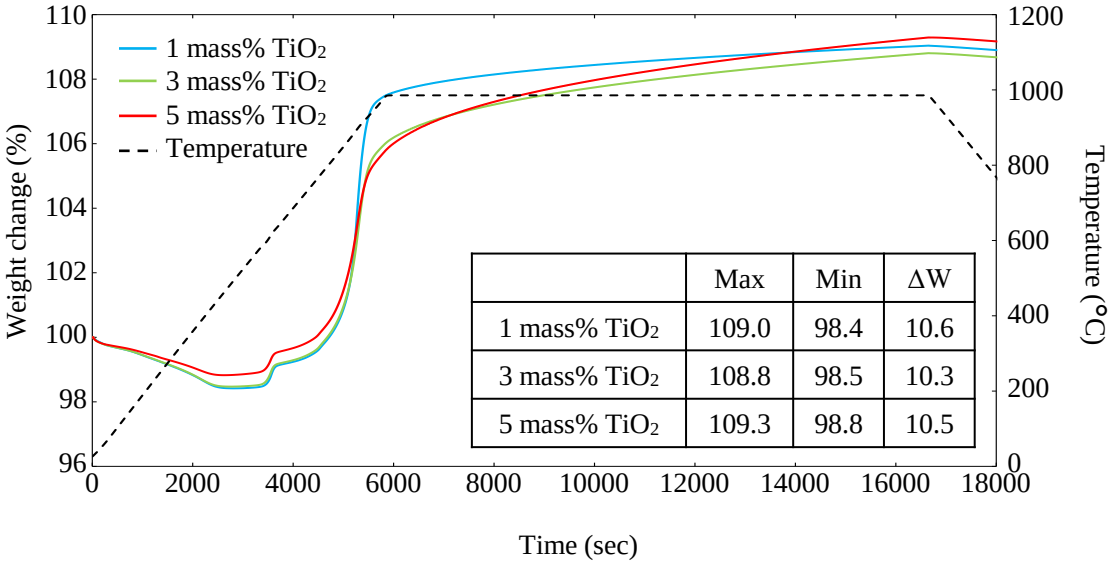

	Max	Min	ΔW
1 mass% TiO_2	109.0	98.4	10.6
3 mass% TiO_2	108.8	98.5	10.3
5 mass% TiO_2	109.3	98.8	10.5

Figure 5-9 shows the weight change of the three different samples during heat treatment. A mass loss was observed around 400 °C, and a mass gain started at around 600 °C. The mass decrease of the samples with 5 mass% TiO_2 was lower than the others.

Figure 5-9 Weight change of samples with 1, 3 and 5 mass% TiO_2 during heat treatment under an O_2 flow at a rate of 200 mL min^{-1}.

Figure 5-10 shows DSC curves of the MEPCM without and with 1, 3, or 5 mass% TiO_2. Table 5-1 shows the phase-change temperature and latent heat of fusion (ΔH; J g^{-1}) evaluated from Fig. 5-10. After TiO_2 addition, the T_m values of the samples were almost the same as that of the initial MEPCM with no TiO_2. In addition, the ΔH decreased by approximately 50 J g^{-1} by TiO_2 addition. Regardless of the TiO_2 content, two exothermic peaks were observed in the DSC curves. Compared to MEPCM without TiO_2, the first endothermic peak of the MEPCMs with TiO_2 was broader and started at higher temperature. The freezing temperature of the MEPCMs with 0, 1, 3, and 5 mass% TiO_2 were 536.0, 569.9, 571.1, and 563.1°C, respectively. The supercooling of the MEPCMs with 1, 3 and 5 mass% of TiO_2 calculated from T_m and the first freezing temperature were 5.9, 4.9, and 12.5°C, respectively.

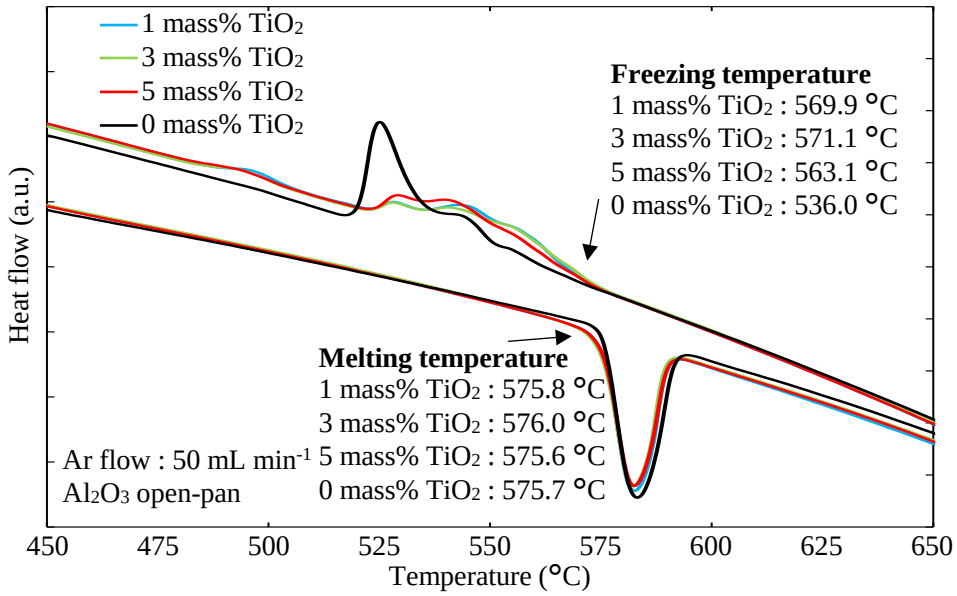

Figure 5-10 DSC curves of MEPCMs without and with 1, 3 and 5 mass% TiO_2

Table 5-1 Melting and freezing temperature and latent heat of fusion evaluated from the DSC curves in Fig. 5-10

TiO_2 content	1st freezing		2nd freezing		Melting		Supercooling
	Temperature (°C)	ΔH (J g^{-1})	Temperature (°C)	ΔH (J g^{-1})	Temperature (°C)	ΔH (J g^{-1})	Temperature (°C)
1 mass%	569.9	231.4	504.8	16.1	575.8	256.8	5.9
3 mass%	571.1	217.0	503.3	15.9	576.0	233.6	4.9
5 mass%	563.1	220.1	502.8	11.3	575.6	248.9	12.5
0 mass%	536.0	267.7	—	—	575.7	304.5	39.7

5.4 Discussion

Ti accumulation was observed inside the MEPCMs (see Fig. 5-3, 5-4, and 5-5). Considering the XRD results, Ti exists as a metallic compound with Si. During heat treatment, the Gibbs' free energy of TiO_2 is always higher than that of Al_2O_3. Based on data from thermodynamic databases, the Gibbs' free energy of the reaction between Al_2O_3 and TiO_2 at 1000°C is as follows.

$$1.5TiO_2+2Al=Al_2O_3+1.5Ti: \Delta G^0_{1000°C} = -199.172\ kJ \quad (1)$$

Thus, Al could reduce TiO_2 under the experimental conditions, allowing the Ti to dissolve into the Al–Si alloy. Moreover, the Gibbs' free energy of the reaction between Al_2O_3 and TiO, which has a low free energy among the Ti oxides, at 1000°C is given by equation (2).

$$3TiO+2Al=Al_2O_3+3Ti \quad \Delta G^0_{1000°C} = -7.146\ kJ \quad (2)$$

At 1000°C, Ti oxides are reduced to the metallic phase by Al (i.e., Al is oxidized by TiO_2), where the Al-oxide particles observed over the shell were probably generated by this redox reaction. In fact, several examples of such reduction have been reported in studies of Al–Ti alloy production [12-16].

Considering the composition of the alloy phase, when 1 mass% TiO_2 was added to Al–25mass%Si, the composition is Al–24.75mass%Si–0.60mass%Ti–0.40mass%O. Here, it is assumed that only Al is consumed from the alloy phase in the oxidation reaction, and that the ratio of Si to Ti remains unchanged. Figure 5-11 shows the a) Al-rich corner of the Al–Ti–Si ternary phase diagram at 1000°C and b) pseudobinary phase diagram of 24.75Si –0.60Ti–Al calculated with thermochemical software, FactSage 8.1, for a range of Al contents. The phase inside the MEPCM during heat treatment (1000°C) was estimated from Fig. 5-11 b). Even for an Al content of ~70 mass%, the interior of the MEPCM is liquid at 1000°C. At room temperature, the alloy phase is expected to contain

Al, Si, and $TiSi_2$, which is consistent with the XRD results shown in Fig. 5-8. In particular, the Ti-containing region was clearly larger than that of the Ti source (i.e., TiO_2 sub-micron particles fixed on the surface during HIB). At the heat treatment temperature (1000°C), the Al–Si alloy inside the MEPCM is in a liquid state, which would allow Ti to precipitate into large crystals. The results indicated that the introduction of Ti by combining the HIB and MEPCM preparation methods was successful. Since the melting of $TiSi_2$ does not terminate until around 900°C, $TiSi_2$ is expected to exist in a solid state at temperatures near the eutectic temperature of Al–Si in the Ti–doped MEPCM. Furthermore, the disregistry is considered, which is the degree of lattice mismatch expressed as $\delta = \Delta a_0/a_0$. The lattice parameters of the orthorhombic $TiSi_2$ are $a_0 = 4.4280$, $b_0 = 4.7790$, and $c_0 = 9.0780$ (Å) [17], and the parameters for Al and Si are $a_0 = 4.0560$ [18] and $a_0 = 5.4317$ (Å) [19], respectively. Thus, the minimum δ between Al and $TiSi_2$ is 9.17% and that between Si and $TiSi_2$ is 11.7%. A smaller disregistry corresponds to a more favorable condition for nucleation. Thus, $TiSi_2$ is the more favorable nucleation site for Al.

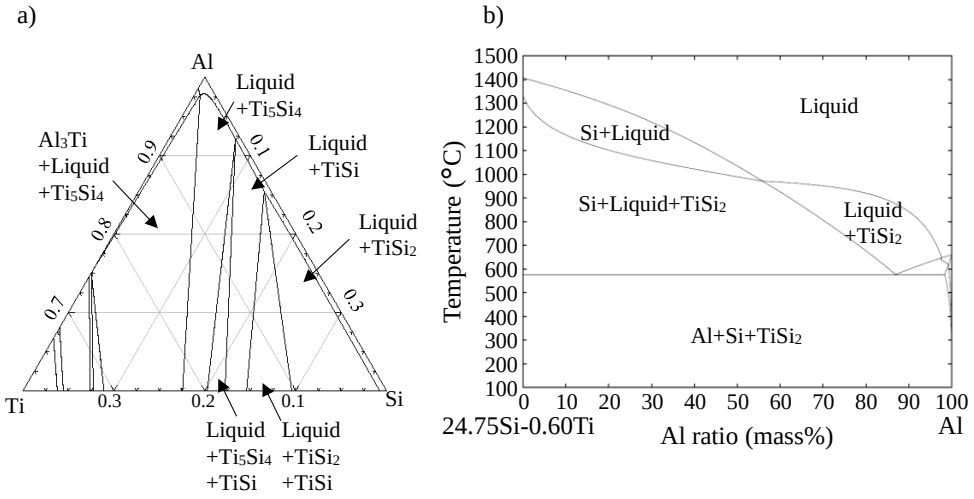

Figure 5-11 a) Al-rich corner of the Al–Ti–Si ternary phase diagram at 1000°C and b) pseudobinary phase diagram of 24.75Si–0.60Ti–Al. The phase diagrams were calculated with thermochemical software, FactSage 8.1.

Excess TiO_2 addition by HIB is ineffective because TiO_2 remained after sample preparation (see Fig. 5-8) and it was observed that supercooling was not suppressed well at high TiO_2 contents. In Fig. 5 and 6 some remaining TiO_2 was observed in the outer layer after heat treatment. Therefore, there is likely a maximum amount of TiO_2 on the surface of the Al–Si that is able to introduce Ti into the MEPCM via the methods described here.

In DSC results of the TiO_2-loaded MEPCMs, broadening of the exothermic curve was observed. Unlike stable sample types, the DSC curves of MEPCMs reflect the statistical distribution of the phase change in each microcapsule. In particular, the shape of the exothermic peak indicating solidification depends on the distribution of the freezing temperature of each microcapsule, because solidification of the liquid alloy in the MEPCM cannot propagate among the microcapsules. Thus, peak broadening indicates a distribution of freezing temperatures in the MEPCM. A small exothermic peak was also observed in the Ti-doped MEPCM at the same temperature as that of the MEPCM without Ti addition. This suggests that a group of particles where undercooling was moderated by the addition of Ti coexisted with a group where undercooling was not moderated, resulting in the DSC curve shown in the Fig. 5-10. Here, TiO_2 addition suppressed supercooling by about 5°C, which was the best effect observed among the samples. While the undercooling was mitigated by the introduction of Ti, it resulted in a broadening of the range of phase-change temperatures. This indicates a variation in the effect of Ti addition, and a more uniform treatment is desirable to obtain sharp peaks.

5.5 Conclusion

The conclusions related to the introduction of Ti into MEPCM to suppress its supercooling are as follows.

1. The chemical and heat treatment by HIB successfully introduced Ti into the Al–Si MEPCM.

2. TiO_2 fixed on the surface of the Al–Si microspheres was reduced by Al during heat treatment, resulting in metallic Ti with Si and $TiSi_2$ on the MEPCM.

3. The DSC curves of the Ti-doped MEPCM showed that the exothermic peak broadened and shifted to higher temperature compared to that without Ti. Focusing on the freezing start temperature, the supercooling degree decreased; the minimum supercooling degree was 4.9 °C.

4. The broad exothermic peaks indicated variations in the effect of Ti addition. More homogenous treatments are required to obtain sharp exothermic peaks.

The results presented in this chapter indicate that it is possible to introduce impurities into the MEPCM using the HIB method. Unfortunately, not all of the particles appeared to suppress supercooling, but it may be possible to achieve supercooling by introducing other nucleation-site candidates or by applying a more homogeneous treatment. It is also possible to introduce impurities in other MEPCM compositions using the same method. Thus, the development of this process is considered to be meaningful for the development of MEPCM with suppressed supercooling.

References

[1] Safari A, Saidur R, Sulaiman F, Xu Y, Dong J. A review on supercooling of Phase Change Materials in thermal energy storage systems. Renew Sust Energ Rev. 2017;70:905-19.

[2] Zahir MH, Mohamed SA, Saidur R, Al-Sulaiman FA. Supercooling of phase-change materials and the techniques used to mitigate the phenomenon. Appl Energy. 2019;240:793-817.

[3] Li M, Liu J, Shi J. Synthesis and properties of phase change microcapsule with SiO_2-TiO_2 hybrid shell. Sol Energy. 2018;167:158-64.

[4] Zhu Y, Qin Y, Liang S, Chen K, Tian C, Wang J, et al. Graphene/SiO_2/n-octadecane nanoencapsulated phase change material with flower like morphology, high thermal conductivity, and suppressed supercooling. Appl Energy. 2019;250:98-108.

[5] Zou D, Liu X, He R, Huang L. High thermal response rate and super low supercooling degree microencapsulated phase change materials (MEPCM) developed by optimizing shell with various nanoparticles. Int J Heat Mass Transfer. 2019;140:956-64.

[6] Marcantonio JA, Mondolfo LF. The Nucleation of Aluminum by Several Intermetallic Compounds. J Inst Met. 1970;96:23-7.

[7] Yamina O, Alain C, Laurence G, Michel B, Gérard T, Philippe G, et al. Effect of Mechanical dry Coating on the Flowability and the Wettability of Silica Gel Powder. HAL 2010;hal-00457782.

[8] Tang W, Fu Z, Zhang J, Wang W, Wang H, Wang Y, et al. Fabrication and characteristics of TiB_2/Al_2O_3 core/shell particles by hybridization. Powder Technol. 2006;167:117-23.

[9] Nishida Y, Iso M, Matsuoka M, Partch R. Study of polyimide particle surface modification by the high-speed impact method. Adv Powder Technol. 2004;15:247-61.

[10] Nomura T, Zhu C, Sheng N, Saito G, Akiyama T. Microencapsulation of metal-based phase change material for high-temperature thermal energy storage. Sci Rep. 2015;5:9117.

[11] Nomura T, Sheng N, Zhu C, Saito G, Hanzaki D, Hiraki T, et al. Microencapsulated phase change materials with high heat capacity and high cyclic durability for high-temperature thermal energy storage and transportation. Appl Energy. 2017;188:9-18.

[12] Gheorghe I, Rack H. Reactive infiltration of 25 vol pct TiO_2/Al composites. Metall Mat Trans A. 2002;33:2155-62.

[13] Kleiner S, Bertocco F, Khalid F, Beffort O. Decomposition of process control agent during mechanical milling and its influence on displacement reactions in the Al–TiO_2 system. Mater Chem Phys. 2005;89:362-6.

[14] Hosseinpouri M, Mirmonsef S, Soltanieh M. Production of Al-Ti master alloy by aluminothermic reduction technique. Can Metall Q. 2007;46:139-43.

[15] Khaghani-Dehaghani M, Ebrahimi-Kahrizsangi R, Setoudeh N, Nasiri-Tabrizi B. Mechanochemical synthesis of Al_2O_3–TiB_2 nanocomposite powder from Al–TiO_2–H_3BO_3 mixture. Int J Refract Met Hard Mater. 2011;29:244-9.

[16] Feng C, Froyen L. Formation of Al_3Ti and Al_2O_3 from an Al–TiO_2 system for preparing in-situ

aluminium matrix composites. Composites Part A: Applied Science and Manufacturing. 2000;31:385-90.
[17] Smith PL, Ortega R, Brennan B. Pseudo-C11b phase formation of titanium disilicide during the C49 to C54 transition. MRS Online Proceedings Library (OPL). 1997;481.
[18] Tougait O, Noël H. Stoichiometry of UAl_4. Intermetallics. 2004;12:219-23.
[19] Kuestner H, Remy H. Z Kristallogr, Kristallgeom, Kristallphys, Kristallchem. 1924;60:379.

Chapter 6

General conclusions

Thermal energy storage technology is important for effective energy use in the field of renewable energy and industry. There is the need for achieving high heat-storage capacities at high temperature. Latent heat storage using a PCM is very attractive due to its advantages; high heat capacity, constant charge/discharge temperature, and no chemical changes. In particular, metallic PCMs have high melting temperature, high thermal conductivity and high heat-storage density. Metallic PCMs have attracted attention as next-generation heat-storage materials. However, the high corrosivity of molten metal is a challenge for practical use. Alloy-type microencapsulated PCMs have been developed as a candidate material to overcome this problem and have attracted much attention in recent years due to their easy handling and high heat-storage density. MEPCMs can be used as a powder material and the development of heat-storage structures with various shapes of MEPCM have been proposed. It is easy to fabricate an LHS structure following these requirements. Chemical-reaction heat control by combining an MEPCM and a catalyst is also proposed as an application of MEPCMs. Alloy-based MEPCMs show supercooling behavior. This phenomenon can be a disadvantage for MEPCM use, which needs to be solved in order to develop further applications. In this thesis, various limitations in the development of a promising thermal energy storage material, Al–Si alloy based MEPCM, were addressed.

In chapter 1, a general introduction was given. The purpose and content of this thesis were described.

In chapter 2, thermal energy storage composites with MEPCM and sintering aids (glass frit) or ceramic (sinterable alumina) were fabricated to prove the concept of the development of an LHS structure using MEPCM. Pellet-type MEPCM–glass-frit composites were obtained, which stored heat around the melting temperature of MEPCM and had approximately double the heat capacity of that of a sensible heat storage material (ΔT = 50 K). The composite with MEPCM and sinterable alumina had LHS ability after sintering. The obtained LHS composites are expected to have good heat resistance. The results shown in chapter 2 indicated that a TES structure can be fabricated via bottom-up approach. Only the production of pellet-type heat-storage materials was presented here, as they are easy to produce. However, in the future, production of heat-storage materials with a more suitable shape for heat exchange, such as honeycomb structures, could be achieved.

In chapter 3, the combination of an MEPCM and Ni catalyst to control chemical reaction heat was proposed. Ni–LHS grains containing an MEPCM were fabricated. The catalytic performance for steam reforming of ethanol was evaluated for the LHS-supported catalyst. During the catalytic tests, there was a reduction in the rate of temperature change due to the heat release of solidification of the PCM at ~550°C. The results demonstrated the possibility of thermal control of chemical reactions by MEPCM. In this thesis, the catalyst bed temperature was not maintained for a long time, and there is still room for improvement in terms of heat-storage density, device arrangement, and catalyst content. A foundation for a novel temperature-control technology that can control of heat from inside the catalyst bed using an MEPCM was provided.

In chapter 4, supercooling phenomena in Al–Si-based MEPCM were

investigated. The MEPCMs were prepared with hypoeutectic, eutectic, and hypereutectic compositions, and various particle diameters. The effect of superheating on supercooling was also described. For all compositions, supercooling increased with decreasing particle diameter. For hypoeutectic MEPCM, supercooling at the eutectic temperature was not observed due to primary Al acting as a nucleation site. For eutectic and hypereutectic MEPCM, supercooling of 25–37°C was observed. In addition, when the MEPCMs were heated to 1000°C and then cooled, the supercooling degree increased significantly. In the hypoeutectic composition, even the precipitation of the Al primary crystal did not occur under these conditions. In this chapter, the dependence of supercooling on the composition, particle diameter, and superheating in Al–Si alloy-based MEPCM was clarified.

In chapter 5, the fabrication of MEPCMs with nucleation aids by high-speed impact blending was evaluated. TiO_2 was fixed on Al–Si alloy microspheres as the raw MEPCM. Ti dissolved in the alloy core of the MEPCM, and supercooling was somewhat suppressed in a part of the MEPCM. It is noteworthy that impurities were incorporated into the alloy-based MEPCM by dry processing. More effective impurity addition can also be expected for not only Al–Si, but also other alloy MEPCMs. This new method is expected to provide a solution for overcoming the supercooling of MEPCMs.

In summary, to develop new applications of MEPCMs, various studies were performed: fabrication of MEPCM composites; combination of MEPCMs and a catalyst; and investigation of unique supercooling and suppression of supercooling by the addition of nucleation aids. It is hoped that the information provided in the thesis will assist the development of technology for effective heat utilization.

Appendix

Publications

1. **Hiroki Sakai**, Nan Sheng, Ade Kurniawan, Tomohiro Akiyama, Takahiro Nomura

"Fabrication of heat storage pellets composed of microencapsulated phase change material for high-temperature applications"

Applied Energy, Vol.265, (2020), pp114673

The former part of Chapter 2 is the contents reported in this paper.

2. **Hiroki Sakai**, Ade Kurniawan, Tomohiro Akiyama, Takahiro Nomura

"Fabrication of Heat Storage Pellets Consisting of a Metallic Latent Heat Storage Microcapsule and an Al_2O_3 Matrix"

ISIJ International, Vol.60 (2020), No.10, pp.2152-2156

The latter part of Chapter 2 is the contents reported in this paper.

3. **Hiroki Sakai**, Yuta Hasegawa, Ade Kurniawan, Takahiro Nomura,

Tomohiro Akiyama

"Reaction Heat Control for Steam Reforming of Ethanol with Ni-supported Latent Heat Storage Grain"

Tetsu-to-Hagane (in Japanese), Vol.106, (2020), No.8, pp.534-541.

Chapter 3 is the contents reported in this paper.

4. Nan Sheng, Chunyu Zhu, **Hiroki Sakai**, Yuta Hasegawa, Tomohiro Akiyama, Takahiro Nomura

"Modified preparation of Al_2O_3@Al-Si microencapsulated phase change material for high-temperature thermal storage with high durability over3000 cycles"
Solar Energy Materials and Solar Cells, Vol.200, (2019), pp109925

5. Kohei Kashiyama, Takahiro Kawaguchi, Kaixin Dong, **Hiroki Sakai**, Nan Sheng, Ade Kurniawan, Takahiro Nomura
"Ga-Based Microencapsulated Phase Change Material for Low-Temperature Thermal Management Applications"
Energy Storage, Vol.2, (2020), e177

6. Takahiro Kawaguchi, **Hiroki Sakai**, Nan Sheng, Ade Kurniawan, Takahiro Nomura
"Microencapsulation of Zn-Al alloy as a new phase change material for middle-high-temperature thermal energy storage applications"
Applied Energy, Vol. 276, (2020), pp115487

7. Hiroaki Koide, Tatsuya Takahashi, **Hiroki Sakai**, Ade Kurniawan, Justin Ning-Wei Chiu, Takahiro Nomura
"Development of Novel Microencapsulated Hybrid Latent/Chemical Heat Storage Material"
ACS Sustainable Chemistry & Engineering, Vol. 8, No.39 (2020), pp14700-14710

8. Tatsuya Takahashi, Hiroaki Koide, **Hiroki Sakai**, Daisuke Ajito, Ade Kurniawan, Yuji Kunisada, Takahiro Nomura
"Catalyst-loaded micro-encapsulated phase change material for thermal control of exothermic reaction"

Scientific Reports, Vol. 11, (2021), pp7539.

9. Hiroaki Koide, Ade Kurniawan, Tatsuya Takahashi, Takahiro Kawaguchi, **Hiroki Sakai**, Yusuke Sato, Justin NW. Chiu, Takahiro Nomura
"Performance analysis of packed bed latent heat storage system for high-temperature thermal energy storage using pellets composed of micro-encapsulated phase change material"
Energy, Vol. 238, (2022), pp121746

10. Takahiro Kawaguchi, Julalak Yoolerd, **Hiroki Sakai**, Yuto Shimizu, Ade Kurniawan, Takahiro Nomura
"Modified preparation of Al_2O_3@Al microencapsulated phase change material with high durability for high-temperature thermal energy storage over 650 ° C"
Solar Energy Materials and Solar Cells, Vol.237, (2022) pp.111540

Presentations (International)

1. **Hiroki Sakai,** Nan Sheng, Tomohiro Akiyama, Takahiro Nomura
"Fabrication of pellet-type latent heat storage composite for high-temperature applications"
The Fifth International Symposium on Innovative Materials and Processes in Energy Systems, IMPRES2019 (Poster Session), Japan, Kanazawa, 2019.10.21-23

Presentations (Domestic)

1. **Hiroki Sakai**, Gaixin Dong, Takahiro Kawaguchi, Ade Kurniawan, Takahiro Nomura

Suppression of supercooling on Al-Si alloy based micro-encapsulated phase change material

SCEJ 52nd Autumn Meeting, (Oral presentation), Okayama (Online), 2021.9.21-24

2. Hiroki Sakai, Gaixin Dong, Takahiro Kawaguchi, Ade Kurniawan, Takahiro Nomura

"Suppression of supercooling of alloy type latent heat storage microcapsule"

-Addition of Ti to Al-Si alloy latent heat storage microcapsule to suppress supercooling-

10th Latent heat engineering symposium, (Oral presentation), Kobe (Online), 2021.11.29-30

Acknowledgments

This study was conducted under the supervision of Associate Prof. Nomura at the Center for Advanced Research of Energy and Materials. I would like to express deep gratitude to Associate Prof. Nomura. Without their advice and support I would not have been able to finish this study.

I also would like to express my gratitude to the committee comprised of Prof. Shigenari Hayashi, Prof. Munekazu Ohno, and Prof. Seiichi Watanabe, who reviewed this dissertation, for their valuable comments and helpful advice.

I would like to express my sincere gratitude to Prof. Akiyama for welcoming me warmly to the laboratory. I am grateful to my co-researchers: Dr. Ade Kurniawan, Mr. Gaixin Dong, Mr. Takahiro Kawaguchi, Mr. Daisuke Ajito, Mr. Ryosuke Ishida, and Mr. Yuto Shimizu. Their kind help and insightful comments always help me. I take this privilege to thank all members of the Laboratory of Energy Media for their kind help and encouragement.

I would also like to express my gratitude to my family for their support and warm encouragement.

This research was partly supported by JSPS KAKENHI Grant Number JP21J11916.